APPLIED COMPUTATIONAL ELECTROMAGNETICS SOCIETY JOURNAL

April 2017
Vol. 32 No. 4
ISSN 1054-4887

The ACES Journal is abstracted in INSPEC, in Engineering Index, DTIC, Science Citation Index Expanded, the Research Alert, and to Current Contents/Engineering, Computing & Technology.

The illustrations on the front cover have been obtained from the research groups at the Department of Electrical Engineering, The University of Mississippi.

EMERITUS EDITORIAL ASSISTANTS

APRIL 2017 REVIEWERS

THE APPLIED COMPUTATIONAL ELECTROMAGNETICS SOCIETY

JOURNAL

Vol. 32 No. 4 April 2017

TABLE OF CONTENTS

FDTD Acceleration using MATLAB Parallel Computing Toolbox and GPU

Joseph E. Diener and Atef Z. Elsherbeni

Electrical Engineering and Computer Science Department
Colorado School of Mines, Golden, CO 80401, USA
jdiener@mines.edu, aelsherb@mines.edu

Abstract ─ We present a MATLAB based finite difference time domain (FDTD) method accelerated using the GPU functions in MATLAB's parallel computing toolbox (PCT). Procedures to achieve significant speedups over a CPU implementation of the same code are outlined. The use of specialized code with NVIDIA's compute unified device architecture (CUDA) programming results in impressive computational speedups. However, this requires specialized programming knowledge to efficiently implement. The MATLAB PCT can be applied directly to pre-existing MATLAB FDTD code and obtain reasonable speedups over equivalent CPU code. We demonstrate several modifications to increase the efficiency on several different NVIDIA graphics cards. Benchmarks are presented on problems of practical size (millions of cells) with a CPML terminated domain.

Index Terms ─ FDTD, GPU, MATLAB.

I. INTRODUCTION

For problems of practical size using FDTD method, domains on the order of tens of millions of cells with large number of time stepping need to be solved. This leads to correspondingly long computation times. Significant speedups in the computation time of FDTD solvers are possible by shifting the computation from the CPU to a GPU. While the most efficient solvers employ code specifically written to run on a GPU, often using CUDA kernels [1, 3-4, 6], this requires specialized programming and is non-trivial to implement. MATLAB is an easy to use high-level programming language available at many universities, currently available for many students and practicing engineers. Efficient implementations of FDTD code on MATLAB can also be an effective educational tool for electromagnetic simulations. This paper shows both the efficiency increases that the PCT allows over regular MATLAB based code, as well as some techniques that can be used to further optimize performance. Performance is benchmarked using the solver speed in millions of cells per second (MCPS), as suggested in [3]. This allows for easy comparison across different platforms and problem sizes. It is worth noting that the codes used for this paper are highly general, and no assumptions are made about uniform discretization to simplify the formulation. Thus, each updating coefficient array is unique and valid for the general FDTD formulation. Speeds of up to ~300MCPS on problems with only near-field excitations, and ~267MCPS with a total-field scattered field (TF/SF) plane-wave source are obtained. These results are slower than those presented using CUDA written codes [1], [8], which presented peak speeds of ~1600MCPS using an NVIDIA Titan-Z card. Our results are significant improvements on regular vectorized-CPU MATLAB code (~11->12 MCPS), and does not require any CUDA programming.

II. IMPLEMENTATION IN MATLAB

The second-order FDTD MATLAB implementation as given in [2] is used as a starting point for code modifications. MATLAB is most efficient with vectorized code, so the updating equations are written in vectorized form as much as possible. As a result, the base FDTD code represents an efficient and straightforward implementation on the MATLAB engine. Since GPU benchmarks are commonly done using single precision because of the superior computing ability on GPUs for single precision problems, single precision is used for the CPU as well. By default, MATLAB operates in double precision, but can be cast into single precision through the single() function. Two benchmark cases are presented, where the solver runs for sufficient time-steps to ensure an accurate representation of the throughput. The first benchmarking problem is the excitation of a dielectric sphere of relative permittivity of 4 and radius of 1mm using the field radiated by a dipole antenna, and the second problem is the excitation of the same sphere using a plane wave. The reason for the two different configurations is to show the performance using a total field FDTD formulation versus a scattered field formulation performance. The CPU MATLAB code in this paper is written in an efficient vectorized style, which will perform matrix operations using multiple processor cores for simple functions (such as *, +, -) which constitute a large portion of the FDTD work load. To examine the efficiency of the code modifications over

Submitted On: July 15, 2016
Accepted On: March 18, 2017

larger domain sizes, the problem space is discretized using increasingly smaller cubic cells. The computational domain boundary is terminated using an air buffer of 8 cells on each side from the sphere, and 6 CPML cells in each direction. The speed of the code in MCPS is presented over domains measured in millions of cells (MC). The problem execution time is measured using the tic/toc functions in MATLAB over the time marching loop, thus the one-time array initializations are not included. Additionally, all benchmarking is performed in MATLAB 2016b. Initial benchmarking is done using an NVIDIA Tesla K40C card, with the CPU code running on an Intel i7-4770 @3.4GHz (8 cores).

III. GPU IMPLEMENTATION

By moving the updating equations onto the GPU, substantially improved performance is obtained compared with the CPU implementation. The most direct implementation on the GPU is simply to call each array as its GPU equivalent, such as Ex = gpuArray(Ex). This requires no further modifications to the code than the above for each field variable and updating coefficients. Figure 1 shows the throughput obtained when directly porting each array into the GPU. For the dipole source, maximum speedups of ~10x are seen, with performance peaking around 115MCPS. The throughput of the GPU code increases with increasingly large domains, so that it never achieves a steady level of constant performance. In contrast, the CPU code has an essentially flat performance of 11 to 12MCPS for domains larger than ~2MC, and only slightly slower speeds for smaller problem sizes.

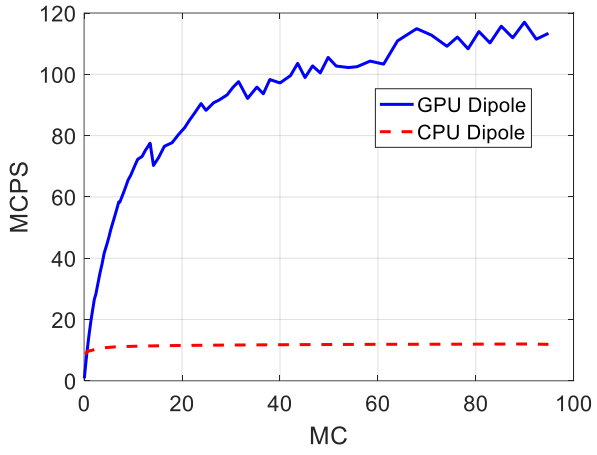

Fig. 1. NVIDIA Tesla K40C direct FDTD port compared against the CPU implementation of the code.

A. Optimize CPML with arrayfun

The updating of the fields in the CPML region on either the GPU or CPU is a significant portion of total computation time in comparison with the E and H field updating in the computational domain. In part this is due to the CPML being unable to be easily vectorized on the CPU. A variety of problems can be vectorized and show dramatic improvement in performance when using arrayfun() on the GPU [4-5, 7]. Here, we demonstrate the application of arrayfun() to the FDTD CPML absorbing boundary condition. The arrays must be of appropriate dimension to perform the scalar expansion employed in arrayfun(), which can necessitate reshaping the array in a preprocessing step. A snippet of the code listing for the arrayfun application to the updating of the Ez-field in the CPML region is shown in listing 1. Similar modifications are required for the other components in the CPML code to allow for arrayfun to be used for each field component. This modification is very efficient and results in much higher computational speeds as shown in Fig. 2. This yields peak speeds of ~157MCPS for the dipole source, a speedup of ~13x compared with respect to the CPU. Peak performance is for a problem size of ~24MC, with nearly steady performance for larger problem sizes.

```
cpml_b_ez_zn=reshape(cpml_b_ez_zn,1,1, ncpml_zn);
Psi_exz_zn=arrayfun(@times,cpml_b_ez_zn,
Psi_exz_zn)+arrayfun(@times,cpml_a_ez_zn,
Hy(:,:,1+cpmlznvec) - Hy(:,:,cpmlznvec) );

Psi_eyz_zn=arrayfun(@times,cpml_b_ez_zn,
Psi_eyz_zn)+arrayfun(@times,cpml_a_ez_zn,
Hx(:,:,1+cpmlznvec) - Hx(:,:,cpmlznvec) );

Ex(:,:,cpmlznvec+1)=Ex(:,:,cpmlznvec+1)+
CPsi_exz_zn.*Psi_exz_zn;
Ey(:,:,cpmlznvec+1)=Ey(:,:,cpmlznvec+1)+
CPsi_eyz_zn.*Psi_eyz_zn;
```

Listing 1. Modification of Ez CPML component from [2] using arrayfun on the GPU.

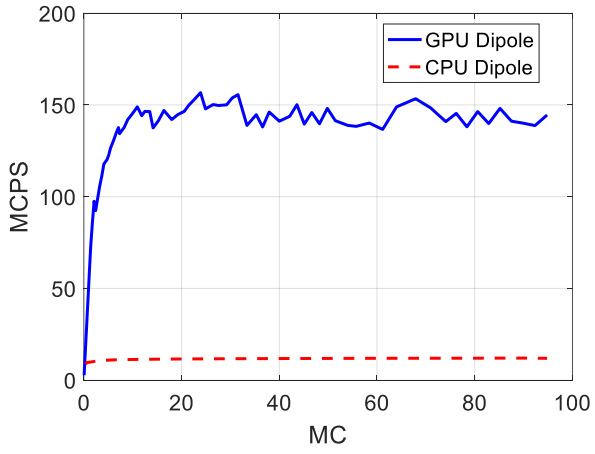

Fig. 2. Tesla K40C performance in comparison with the dipole benchmark on CPU using CPML modification.

B. Optimized E-field updating process

MATLAB tends to be fastest when using vectorized code, and is capable of performing element-wise computation very efficiently. Performance decreases when blocks of a matrix must be multiplied instead of the entire matrix. The staggered grid in FDTD creates differently sized field components, and this leads to explicit indexing in the updating equations for either the electric or magnetic field components, depending on which field terminates the computational domain. In our analysis, the electric field is used to terminate the computational domain. The electric field components are updated with the staggered magnetic field component differences, as shown in listing 2.

```
Ex(1:nx,2:ny,2:nz)=Cexe(1:nx,2:ny,2:nz).*
Ex(1:nx,2:ny,2:nz)+Cexhz(1:nx,2:ny,2:nz).*...
(Hz(1:nx,2:ny,2:nz)-Hz(1:nx,1:ny-1,2:nz)) ...
+ Cexhy(1:nx,2:ny,2:nz).*...
 (Hy(1:nx,2:ny,2:nz)-Hy(1:nx,2:ny,1:nz-1));
```

Listing 2. Ex updating equation for FDTD in MATLAB as presented in [2].

This means that portions of the electric field components and updating coefficients arrays are multiplied with portions of the magnetic field components. Quicker computation can be achieved by multiplying and writing to the entire electric field component arrays, without explicit indexing. By concatenating an array of zeros along the appropriate dimensions, the Hz array for updating Ex can be used without indexing, and becomes a simple vector operation. Listing 3 shows the equivalence of the two operations.

$$A = [Hz\ 0],$$
$$B = [0\ Hz].$$

Listing 3. Example of zero-padding arrays to accomplish indexless updating in electric field components.

Consider two new matrices, A and B. A is the 'right' zero padded matrix, and B is the 'left' zero padded matrix, where the zero padding is of appropriate size such that the resulting matrices have equal size to Ex. This removes any need to index A or B, and reproduces the staggered difference in Hz with the vector operation $A - B$. The first and last row in y will write incorrect values to Ex, but this can be handled by zeroing the updating coefficient array, $Cexhz(:,1,:) = 0$, $Cexhz(:,j+1,:) = 0$. Defining similar matrices $C = [Hy\ 0]$, $D = [0\ Hy]$, and zeroing the coefficient array $Cexhy(:,:,1) = 0$, and $Cexhy(:,:,end) = 0$, we can write the updating equation as: $Ex = Cexe * Ex + Cexhz * (A - B) + Cexhy * (C - D)$. This results in a speedup in MATLAB by removing the explicit subscripting that is ordinarily required. The example code listing below shows how the zero padding is performed within MATLAB:

$$A = \mathrm{cat}(2, \mathrm{Hz}, \mathrm{zeros}(\mathrm{nx}, 1, \mathrm{nz}+1)),$$
$$B = \mathrm{cat}(2, \mathrm{zeros}(\mathrm{nx}, 1, \mathrm{nz}+1), \mathrm{Hz}),$$

the updating modifications to the other electric field components are similar. The integer in the 'cat' command represents the dimension along which the zero array is appended. '1' corresponds to the x-axis, '2' corresponds to the y-axis, and '3' to the z-axis. The effect of these changes are seen in Fig. 3, where a large speedup is obtained over solely modifying the CPML. This concatenation approach yields peak speeds of ~220MCPS – an increase of ~70MCPS over just the CPML modification. This performance can be increased further by putting the various FDTD updating arrays into a single function call, with each component of the electric or magnetic field using an arrayfun() call on a sub-function that will update the field component. This is detailed in the listings given in the appendix. The CPML boundaries are similarly put into a single function that internally updates each boundary using the arrayfun() approach. The results of this optimal updating are shown in Fig. 4. This shows a maximum increase of ~90MCPS, yielding maximum performance of 310MCPS. With the optimal updating established, the analysis for the plane-wave benchmark is shown in Fig. 5. The peak performance in the plane wave is ~270MCPS, a full 40MCPS less than the dipole case. The overall shape of the two curves are very similar, with a performance loss incurred by the extra updating required in the TF/SF formulation.

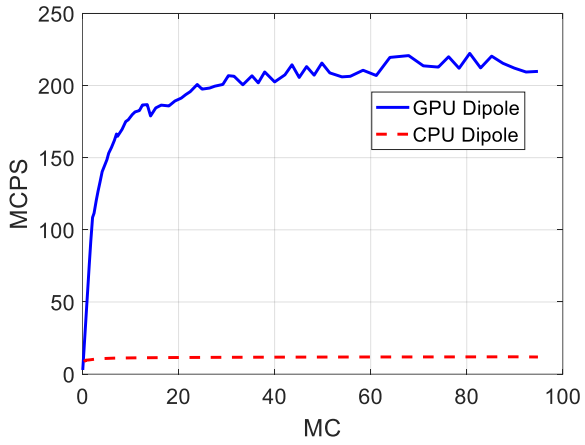

Fig. 3. NVIDIA Tesla K40C performance with concatenated E-field modification.

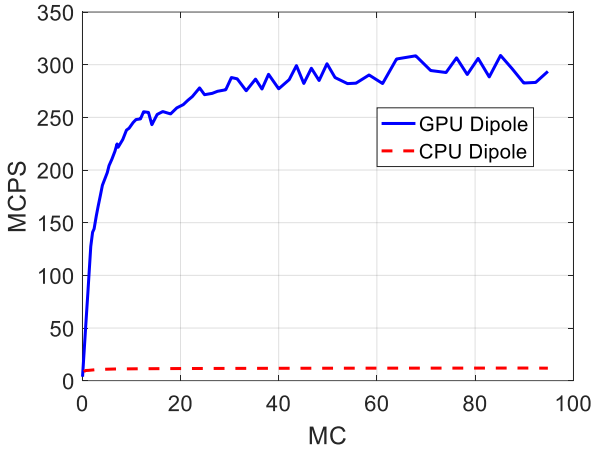

Fig. 4. NVIDIA Tesla K40C performance with optimal updating.

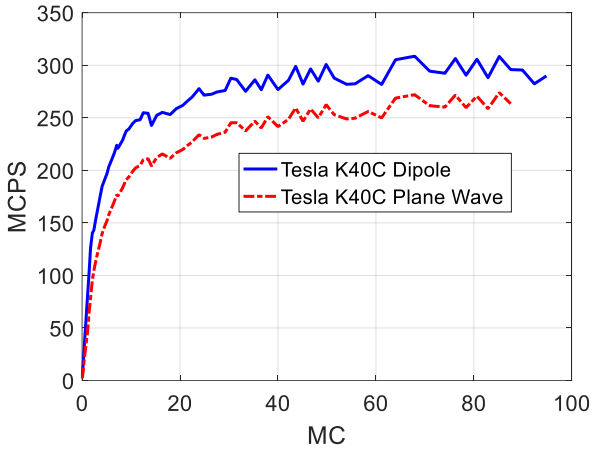

Fig. 5. Comparison of planewave benchmark and dipole benchmark on K40C.

IV. BENCHMARKING SEVERAL GPUs

With the completion of the optimization of the code, the same benchmarking analysis is performed on different NVIDIA graphics cards with each method, for both the plane wave and dipole cases. The analysis is restricted to the dipole case, as the plane wave results show essentially the same performance curves, with reduced maximum speeds. An NVIDIA GTX-780 (3GB) and NVIDIA Titan-Z (12GB) are chosen to compare the results of the developed code. While the Titan-Z nominally has 12GB of memory, it is spread across two 6GB processors on the same physical card, which are addressed separately within MATLAB. Thus, only 6GB of memory is addressable at a time in the current implementation. In Fig. 6, the comparison between the Tesla K40C, GTX-780, and Titan-Z is shown for the dipole case. Similar max speeds are obtained for each of the cards. The K40C has a maximum speed of 310MCPS, the GTX a maximum speed of 303MCPS, and the Titan-Z a maximum speed of 367MCPS. However, both the GTX and Titan-Z demonstrate a marked reduction in speed after hitting their peak performance – thus, an 'optimal' problem size is smaller than one using the K40C card. Since different versions of MATLAB can sometimes improve or even reduce the performance of different code [9], this behavior may change with different versions of MATLAB and the PCT.

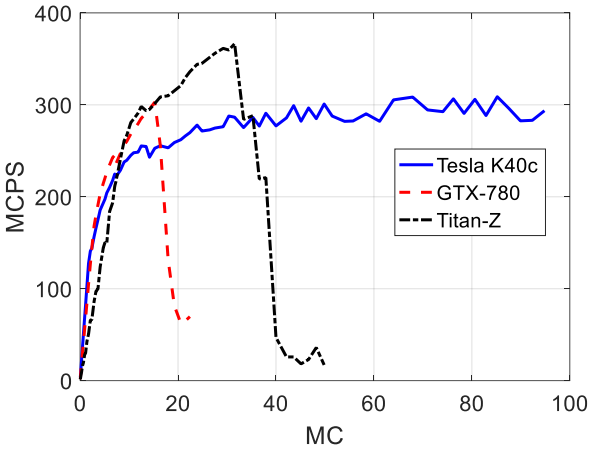

Fig 6. Comparison of optimal updating for three NVIDIA cards for dipole problem.

V. CONCLUSION

In this paper, the implementation of a FDTD solver in MATLAB using the parallel computing toolbox and its GPU computing capabilities is examined. The appendix lists in some detail functions from the best code developed in this paper. We avoid the use of specialized CUDA based programming in order to present an easy to implement code that can achieve substantial speedups in MATLAB. Code is benchmarked across several GPUs and problem types. Sizeable computational speeds on problems of practical sizes with CPML absorbing boundaries are achieved. A method of removing explicit indexing for one set of field-updating in the FDTD loop is presented that shows strong improvements on throughput that might be similarly useful in other vectorized programming languages.

APPENDIX

A more complete listing of the optimized updating code for a generic FDTD problem is given in this listing. First, the form of the electric field updating step within the main FDTD loop is shown in listing 4. The function outputs the updated electric field components, and takes as inputs the field components, updating matrices, and computational domain size.

```
[Ex, Ey, Ez] = updateEfields( Ex, Cexe, Cexhz, Cexhy,
     Ey, Ceye, Ceyhx, Ceyhz,  Ez, Ceze, Cezhx, Cezhy,
```

```
    Hx, Hy, Hz, nx, ny, nz);
```

Listing 4. Form of the electric field updating step in the time marching loop.

The function "updateEfields" contains the concatenated field updating as a separate step for each field component. Listing 5 shows this for the y-component of the field, with the equations and matrices A1 and B1 having a similar form for the other components.

```
A1 = zeros(nx+1, ny, 1, 'gpuArray');
B1 = zeros(1, ny, nz+1, 'gpuArray');

Ey = arrayfun(@updateEcomponent, Ey, Ceye, Ceyhx,
   cat(3, Hx, A1), cat(3, A1, Hx), ...
   Ceyhz, cat(1, Hz, B1), cat(1, B1, Hz));
```

Listing 5. Ey updating step within "updateEfields" function.

Finally, this calls the subfunction "updateEcomponent", which takes as input the appropriate field component, coefficient matrices, and auxiliary matrices. This is shown in listing 6. The function updates the input field with purely element wise operations.

```
function [A] = updateEcomponent(A, B, C, D, E, F, G,
H)

 A = A.*B + C.*(D - E) + F.*(G - H);
```

Listing 6. Function updateEcomponent.

A nearly identical set of functions are defined for the magnetic field components updating step. Similarly, the CPML updating step for the electric and magnetic fields are called as one function, which contains bsxfun() function calls for efficient updating. This is shown in listings 7 and 8.

```
[Hx, Hy, Hz, Psi_hyx_xn, Psi_hzx_xn, Psi_hzy_yn,
Psi_hxy_yn, Psi_hxz_zn, Psi_hyz_zn,  Psi_hyx_xp,
Psi_hzx_xp,  Psi_hzy_yp, Psi_hxy_yp,Psi_hxz_zp,
Psi_hyz_zp]  = update_magnetic_field_CPML_ABC
(Hx, Hy, Hz, Ex, Ey, Ez, cpml_b_mx_xn,
cpml_a_mx_xn, Psi_hyx_xn, Psi_hzx_xn,
CPsi_hyx_xn, CPsi_hzx_xn,  cpml_b_my_yn,
cpml_a_my_yn, Psi_hzy_yn, Psi_hxy_yn,
CPsi_hzy_yn, CPsi_hxy_yn,  cpml_b_mz_zn,
cpml_a_mz_zn, Psi_hxz_zn, Psi_hyz_zn, CPsi_hxz_zn,
CPsi_hyz_zn,  n_cpml_xn, n_cpml_yn, n_cpml_zn, ...
cpml_b_mx_xp, cpml_a_mx_xp, Psi_hyx_xp,
Psi_hzx_xp, CPsi_hyx_xp, CPsi_hzx_xp, ...
cpml_b_my_yp, cpml_a_my_yp, Psi_hzy_yp,
Psi_hxy_yp, CPsi_hzy_yp, CPsi_hxy_yp, ...
cpml_b_mz_zp, cpml_a_mz_zp, Psi_hxz_zp,
Psi_hyz_zp, CPsi_hxz_zp, CPsi_hyz_zp, ...
n_stmx, n_stmy, n_stmz, nx, ny, nz);
```

Listing 7. The function call for updating all the CPML boundaries within the domain for the magnetic field.

```
Psi_hyx_xn = bsxfun(@times, cpml_b_mx_xn,
Psi_hyx_xn)  + bsxfun(@times, cpml_a_mx_xn,
diff(Ez(1:n_cpml_xn+1, :,:) , 1, 1) );

Psi_hzx_xn =bsxfun(@times,  cpml_b_mx_xn,
Psi_hzx_xn)  + bsxfun(@times, cpml_a_mx_xn,
diff(Ey(1:n_cpml_xn+1, :,:) , 1, 1) );

Hy(1:n_cpml_xn, :,:) = Hy(1:n_cpml_xn, :,:)  +
CPsi_hyx_xn.* Psi_hyx_xn;
Hz(1:n_cpml_xn, :,:) = Hz(1:n_cpml_xn, :,:)  +
CPsi_hzx_xn.* Psi_hzx_xn;
```

Listing 8. The 'xn' boundary of CPML updating within the function call.

The bsxfun() call is used for updating the CPML matrices efficiently. A boolean check can be implemented for domains with mixed boundaries with little impact on the performance.

REFERENCES

[1] V. Demir and A. Z. Elsherbeni, "Compute unified device architecture (CUDA) based finite-difference time-domain (FDTD) implementation," *ACES Journal*, vol. 25, no. 4, pp. 303-314, April 2010.

[2] A. Z. Elsherbeni and V. Demir, *The Finite-Difference Time-Domain Method for Electromagnetics with MATLAB Simulations*. second edition, ACES Series on Computational Electromagnetics and Engineering, SciTech Publishing, an Imprint of IET, Edison, NJ, 2016.

[3] V. Demir, "A stacking scheme to improve the efficiency of finite-difference time-domain solutions on graphics processing units," *ACES Journal*, vol. 25, no. 4, pp. 323-330, April 2010.

[4] Illustrating three approaches to GPU Computing: the Mandelbrot Set, http://www.mathworks.com/help/distcomp/examples/illustrating-three-approaches-to-gpu-computing-the-mandelbrot-set.html, May, 2016.

[5] Improve Performance of Element-wise MATLAB Functions on the GPU using ARRAYFUN, http://www.mathworks.com/help/distcomp/examples/improve-performance-of-element-wise-matlab-functions-on-the-gpu-using-arrayfun.html, May, 2016.

[6] M. J. Inman, A. Z. Elsherbeni, and C. J. Reddy, "CUDA based LU decomposition solvers for CEM

applications," *ACES Journal*, vol. 25, no. 4, pp. 339-347, April 2010.

[7] Joss Knight, High-Performance MATLAB with GPU Acceleration, https://devblogs.nvidia.com/parallelforall/high-performance-matlab-gpu-acceleration, January 2017.

[8] V. Demir, A. Z. Elsherbeni, CEMS Software Package, based on [2], 2014.

[9] MATLAB Answers Forum Question, http://www.mathworks.com/matlabcentral/answers/239817-matlab-s-r2015b-new-jit-experiences-a-severe-degradation-in-speed-in-the-following-example-but-the, February 2017.

Joseph E. Diener obtained his bachelor's degree in Physics from the University of Puget Sound in 2013. Currently he is a Master's Student at the Colorado School of Mines studying Electrical Engineering. His research interests include finite difference time domain methods, antennas, microwave measurements, and phased arrays.

Atef Z. Elsherbeni received his Ph.D. degree in Electrical Engineering from Manitoba University, Winnipeg, Manitoba, Canada, in 1987. Elsherbeni was with the University of Mississippi from 1987 to 2013. He was a Finland Distinguished Professor from 2009 to 2011. In August 2013 he joined the Electrical Engineering and Computer Science Department at Colorado School of Mines where he is now the Dobelman Distinguished Chair Professor and the Head of the Electrical Engineering Department. His research interest includes the scattering and diffraction of EM waves, finite-difference time-domain analysis of antennas and microwave devices, field visualization and software development for EM education, interactions of electromagnetic waves with the human body, RFID and sensor integrated FRID systems, reflector and printed antennas and antenna arrays, and measurement of antenna characteristics and material properties. Elsherbeni is a Fellow Member of IEEE and ACES. He is the Editor-in-Chief for ACES Journal. He was the General Chair for the 2014 APS-URSI Symposium and was the President of ACES Society from 2013 to 2015.

A Novel Method to Solve 2nd Order Neumann Type Boundary Value Problems in Electrostatics

Goker Sener

Department of Electrical Electronics Engineering
Cankaya University, Ankara, 06790, Turkey
sener@cankaya.edu.tr

Abstract ─ In this paper, the numerical method of non-polynomial spline approximation is used to solve 2nd order Neumann type boundary value problems (bvp's) in electrostatics. This new approach provides more accurate results than the polynomial approximations and the spectral methods. The literature contains very little on the solution of Neumann type bvp's because of the fact that a unique solution does not exist for all problems. In electrostatics, Neumann type bvp's are encountered for finding the electrostatic potential inside closed surfaces where the normal derivative of the electric potential is specified everywhere on the surface. Two examples are presented to prove the accuracy of the proposed method. In these examples, the governing differential equation is solved to find the electrostatic potential inside a region bounded by conductors that are maintained at constant voltages. The results are compared with the analytic solutions.

Index Terms ─ Boundary value problems, electrostatics, Neumann boundary conditions, numerical methods.

I. INTRODUCTION

Many problems in engineering require the solution of differential equations. If the initial conditions for the solution of the equation are given at the boundaries, these problems are called the "boundary value problems" or shortly the "bvp's". In electrostatics, there are two types of bvp's that govern the majority of problems. They are known as the "Poisson's equation" and the "Laplace equation". Both are 2nd order linear differential equations having the electric potential as the unknown variable that is a function of space coordinates. If the derivatives of the electric potential at the boundaries are specified, then these problems are named as "Neumann type bvp's" [1].

Numerical methods are used to solve bvp's, especially when analytical solutions in closed form are difficult to obtain. The finite difference method (FDM) and the finite element method (FEM) are the most frequently used numerical methods to solve electrostatic problems containing partial or ordinary differential equations [2,3]. These methods are based on discretization of the solution domain and transforming the differential equation into a system of linear equations. They are applicable to problems with non-homogenous media easily. However, one of their disadvantages is that for Neumann type bvp's, the computation matrix of the linear system of equations, also called the "stiffness matrix", is singular, and therefore a solution does not exist [4,5].

In this paper, a new numerical method, called the "Non-polynomial Spline Approximation" is introduced to solve 2nd order electrostatic bvp''s having Neumann type boundary conditions. In this method, the solution domain is sampled by n points, and for each sample, the unknown function is approximated by a non-polynomial (trigonometric) function. The approximated solution is replaced into the differential equation, and the resulting linear equation system is solved for the unknown function of the problem. The proposed method has the advantage of producing an approximate solution for Neumann type bvp's. In literature, there are many applications of FDM and FEM in electromagnetics specifically for Dirichlet or mixed type bvp's. For example, in [6], several FEM based numerical techniques are compared to existing methods in terms of their accuracy for solving boundary value problems in electromagnetics. In [7], the boundary element method (BEM) is used for solving the electromagnetic problems. In [8], the FEM is used for the solution of electromagnetic problems involving anisotropic media. In [9], FDM is analyzed as the numerical technique for non-stationary electromagnetic problems. Up to the authors' knowledge, the work in this paper is novel in the sense that the method of non-polynomial spline approximation has not been applied to electrostatic problems having Neumann type bvp's before.

Two examples are presented to prove the applicability and the accuracy of the proposed method. In the first example, the Poisson's equation is solved for the unknown electrostatic potential distribution inside a charged homogeneous dielectric medium. In the second example, the Laplace equation is solved for the

Submitted On: February 11, 2016
Accepted On: March 13, 2017

electrostatic potential in a 2-D region enclosed by conducting boundaries.

II. NON-POLYNOMIAL SPLINE APPROXIMATION

A. Formulations

The solution of the following linear 2nd order boundary value problem is considered [4]:

$$y^2 + f(x)y = g(x), \quad x \in [a,b], \tag{1}$$

subjected to the Neumann boundary conditions:

$$y^{(1)}(a) - A_1 = y^{(1)}(b) - A_2 = 0, \tag{2}$$

where A_1 and A_2 are the real constants. The functions $f(x)$ and $g(x)$ in (1) are assumed to be continuous in $[a,b]$.

The solution domain $x \in [a,b]$ is sampled by equally spaced n points as:

$$x_i = a + ih, \quad i = 0,1,\dots,n, \tag{3}$$

where $x_0 = a$, $x_n = b$, and $h = (b-a)/n$.

Now, the notation $y(x)$ is used as the exact solution of (1), and S_i as the approximate solution to $y_i = y(x_i)$ acquired by the spline function $Q_i(x)$ that fits in the points (x_i, S_i) and (x_{i+1}, S_{i+1}).

A non-polynomial spline $Q_i(x)$ is defined in the following form:

$$Q_i(x) = a_i \cos \mathrm{k}(x - x_i) + b_i \sin \mathrm{k}(x - x_i) + c_i, \quad i = 0,1,\dots,n-1, \tag{4}$$

where a_i, b_i and c_i are constant coefficients, and k is the frequency of the trigonometric functions. Thus, the non-polynomial spline function $S(x)$ that approximates to the exact solution can be written as:

$$S(x) = Q_i(x), \quad x \in [x_i, x_{i+1}], \quad i = 0,1,\dots,n-1. \tag{5}$$

The spline function $Q_i(x)$ and its derivatives are defined as:

$$Q_i(x_{i+1/2}) = S_i(x_{i+1/2}), \quad Q_i^{(1)}(x_i) = D_i, \quad Q_i^{(2)}(x_{i+1/2}) = F_{i+1/2}, \tag{6}$$

where the notation $x_{i+1/2}$ denotes the midpoint of the interval $[x_i, x_{i+1}]$. By using (4) and (6), one can obtain the following relations for the constant coefficients:

$$a_i = \frac{-1}{k^2} F_{i+1/2} \sec(\theta/2) - \frac{1}{k} D_i \tan(\theta/2), \quad b_i = \frac{1}{k} D_i, \quad c_i = S_{i+1/2} - \frac{1}{k^2} F_{i+1/2}, \tag{7}$$

where $\theta = kh$ and $i = 0,1,\dots,n-1$.

By using the continuity of the spline function $Q_i(x)$ at the joining nodes:

$$Q_{i-1}^{(m)}(x) = Q_i^{(m)}(x), \quad m = 0,1, \tag{8}$$

together with (4) and (7), we obtain the following relation:

$$\left(S_{i+1/2} - 2S_{i-1/2} + S_{i-3/2}\right) = h^2(\alpha F_{i+1/2} + \omega F_{i-1/2} + \alpha F_{i-3/2}), \quad i = 2,3,\dots,n-1, \tag{9}$$

where

$$\alpha = \frac{\sec(\theta/2) - 1}{\theta^2}, \tag{10}$$

and

$$\omega = \frac{4\sec(\theta/2)\sin^2(\theta/2) + 2(1 - \sec(\theta/2))}{\theta^2}. \tag{11}$$

(9) gives $n-2$ linear equations with n unknowns $S_{i+1/2}$, $i = 0,1,\dots,n-1$. Two more equations come from the boundary nodes as:

$$\left(-hS_0^{(1)} - S_{1/2} + S_{3/2}\right) = \frac{h^2}{24}(23F_{1/2} + F_{3/2}), \quad at\ i = 1, \tag{12}$$

and

$$\left(S_{n-3/2} - S_{n-1/2} + hS_n^{(1)}\right) = \frac{h^2}{24} 23F_{n-3/2} + 23F_{n-1/2}, \quad at\ i = n. \tag{13}$$

As a result, the linear equation solution of (9) gives the approximate solution S_i to $y_i = y(x_i)$, $i = 0,1,\dots,n-1$.

For $\boldsymbol{\alpha = 1/12}$ and $\boldsymbol{\omega = 10/12}$, the algorithm produces the most accurate numerical results [4], thus all of the computations in this paper are carried out using these values.

B. Error analysis

The local truncation error t_i for $i = 1,2,\dots,n$ corresponding to (9)-(13) is given as [4]:

$$t_i = \frac{-h^4}{24} y_0^{(4)} + O(h^5), \quad i = 1,$$

$$t_i = h^2(1 - 2\alpha - \omega)y_i^{(2)} + h^3\left(\alpha + \frac{\omega}{2} - \frac{1}{2}\right)y_i^{(3)} + h^4\left(\frac{5}{24} - \frac{5}{4}\alpha - \frac{\omega}{8}\right)y_i^{(4)} - h^5\left(\frac{1}{16} - \frac{26}{48}\alpha - \frac{\omega}{48}\right)y_i^{(5)} + O(h^6), \quad i = 2,3,\dots,n-1$$

$$t_i = \frac{-h^4}{24} y_n^{(4)} + O(h^5), \ i = n. \tag{14}$$

Thus, for the boundary nodes and interior nodes, the error is of the order of 5 and 6 respectively.

The truncation error associated with the algorithm can be defined as:

$$e_{i+1/2} = y_{i+1/2} - S_{i+1/2}, \tag{15}$$

where $y_{i+1/2} = y\left(x_{i+1/2}\right)$ and $S_{i+1/2}$, $i = 0,1,\dots,n-1$, are the exact, and the approximated solutions respectively at the $(i+1/2)^{th}$ nodes. The total truncation error is given by [4]:

$$\|E\|_\infty \le O(h^2), \tag{16}$$

where $\|E\|_\infty$ is the maximum norm of the global error vector:

$$e_{i+1/2} = y_{i+1/2} - S_{i+\frac{1}{2}}, \quad i = 0,1,2,..,n. \tag{17}$$

Thus, the error is bounded by $\boldsymbol{O(h^2)}$ which implies that the method is quadratically convergent. Also, all round-off errors in this analysis are neglected assuming high digit computations by Matlab.

III. EXAMPLES

A. Solution of 1D electrostatic potential

Finding the electrostatic potential inside a parallel

plate capacitor is considered. The governing equation for this problem is the "Poisson's equation". To ensure that the equation satisfies the Neumann boundary conditions, we specify the normal derivatives of the potential at the boundaries. All numeric computations are carried out with the software program Matlab.

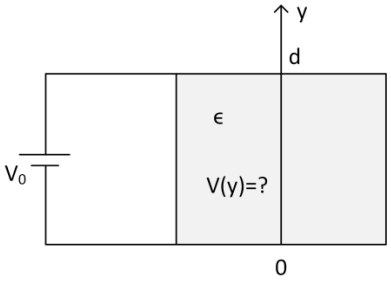

Fig. 1. Cross sectional figure of the capacitor problem.

Figure 1 shows the physical description of the problem. The parallel plate capacitor is assumed to be filled by a charged medium with the uniform charge density ρ and the electric permittivity ϵ. The capacitor has a plate separation length d, and maintained at potential V_0 volts across its plates. The fringe fields at the plate edges are assumed to be negligible, thus the voltage inside the capacitor varies only along the y direction. The Poisson's equation for this problem can be written as [10]:

$$\frac{d^2V(y)}{dy^2} = \frac{-\rho}{\epsilon}, \tag{18}$$

whose solution can be obtained by taking the integral of both sides with respect to y twice. This gives the following result:

$$V(y) = \frac{-\rho}{2\epsilon}y^2 + C_1 y + C_2, \tag{19}$$

where C_1 and C_2 are the constants to be determine by the boundary conditions. Given the following Neumann boundary conditions:

$$\frac{dV(0)}{dy} = \frac{\rho d}{2\epsilon} + \frac{V_0}{d}, \tag{20}$$

and

$$\frac{dV(d)}{dy} = \frac{-\rho d}{2\epsilon} + \frac{V_0}{d}, \tag{21}$$

the solution of the problem exists up to a constant.

The constant C_1 can be obtained by imposing (20) to the derivative of the solution in (19) as:

$$C_1 = \frac{\rho d}{2\epsilon} + \frac{V_0}{d}. \tag{22}$$

Thus, the solution becomes:

$$V(y) = \frac{-\rho}{2\epsilon}y^2 + \left(\frac{\rho d}{2\epsilon} + \frac{V_0}{d}\right)y + C_2. \tag{23}$$

Now, we consider the numeric solution of the problem using the proposed approximation. Figure 2 shows the results for the following simulation parameters: $d = 1(m)$, $V_0 = 1(V)$, $\rho = 10^{-9}(C/m^3)$, $\epsilon_r = 1$, $C_2 = 0$. The results show good accuracy especially for greater number of samples being used.

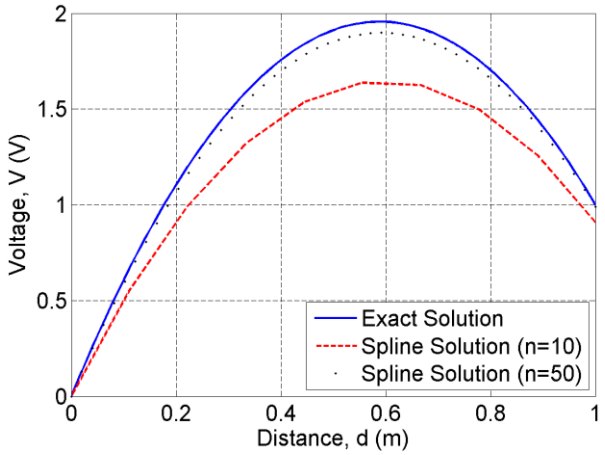

Fig. 2. Simulation results for the voltage distribution inside a parallel plate capacitor for sampling number n=10 and n=50.

The numerical stability of the proposed method is analyzed in terms of the condition number, k(A), of the solution matrix in (9). Figure 3 shows the results with respect to the number of sample points. The proportional relation between the condition number and the size of the matrix is expected [11]. In general, if the condition number $k(A) = 10^k$, then "k" digits of accuracy are lost (at most) during computation in addition to round off errors [12]. Thus, neglecting the round off errors, from Fig. 3 the method is bounded approximately by 5 digits of inaccuracy at about n=50 sampling points, and since the Matlab simulation uses 16 digits of precision, this does not disrupt convergence.

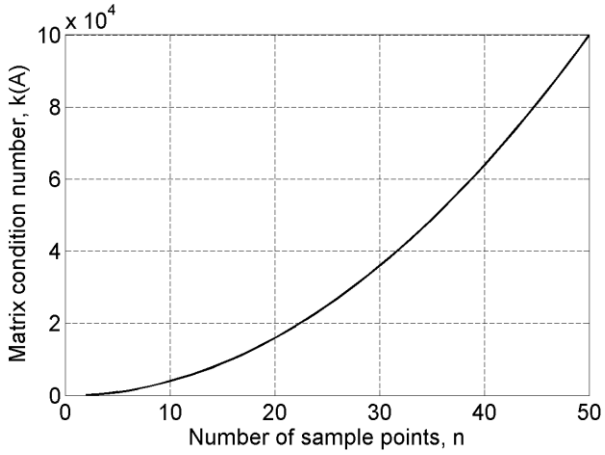

Fig. 3. Stability analysis of the proposed method.

B. Solution of 2D electrostatic potential

Finding the electrostatic potential inside a 2D charge free area is considered. The region is bounded by three conducting rods maintained at constant voltages. Figure

4 shows the physical arrangement of the problem.

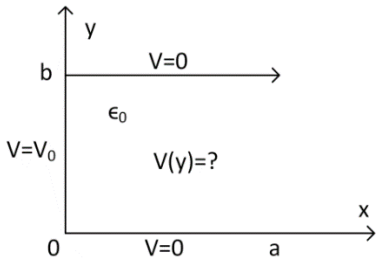

Fig. 4. Cross sectional figure of 2D electrostatic potential example.

The governing equation for this problem is the "Laplace equation", given in rectangular coordinates as:

$$\frac{\partial^2 V(x,y)}{\partial x^2} + \frac{\partial^2 V(x,y)}{\partial y^2} = 0. \quad (24)$$

The analytic solution of the problem is obtained by separating the solution into the product of functions that are only dependent on a single coordinate variable; this procedure is known as the "separation of variables". Thus, we write the solution as:

$$V(x,y) = X(x)Y(y), \quad (25)$$

where $X(x)$ and $Y(y)$ are the solutions of the following ordinary differential equations:

$$\frac{d^2X(x)}{dx^2} + k_x^2 X(x) = 0, \quad (26)$$

and

$$\frac{d^2Y(y)}{dy^2} + k_y^2 Y(y) = 0, \quad (27)$$

where k_x and k_y are so called the separation constants.

Let us assume that the following boundary conditions are given. In the y-direction:

$$\frac{\partial Y(0)}{\partial y} = \frac{\pi}{b}, \quad \frac{\partial Y(b)}{\partial y} = -\frac{\pi}{b}, \quad (28)$$

and in the x-direction:

$$\frac{\partial X(0)}{\partial x} = \frac{-j\pi}{b}, \quad \frac{\partial X(\infty)}{\partial x} = 0. \quad (29)$$

The analytic solutions of (26) and (27) subjected to Neumann boundary conditions (28) and (29) are given as [10]:

$$X(x) = D_2 e^{-k_x x}, \quad (30)$$

and

$$Y(y) = A_1 \sin(k_y y), \quad (31)$$

where $k_x = jk$, $k_y = k$, and $k = \frac{m\pi}{b}$ for $m = 1$.

The solution of the problem is given by:

$$V(x,y) = \frac{4V_0}{\pi} e^{-\frac{\pi x}{b}} \sin(\frac{\pi}{b} y),$$
$$x > 0, \quad 0 < y < b, \quad and\ m = 1, \quad (32)$$

where $A_1 D_2 = \frac{4V_0}{m\pi}$.

The general solution of the problem includes all the values for the constant m, and is given by:

$$V(x,y) = \sum_{m=1}^{\infty} C_m e^{-\frac{m\pi x}{b}} \sin\left(\frac{m\pi}{b} y\right),$$
$$m = 1, 3, 5, \ldots, \quad x > 0 \ and\ 0 < y < b, \quad (33)$$

where $C_m = A_1 D_2 = \frac{4V_0}{m\pi}$.

Figure 5 and Fig. 6 show the solutions of (26) and (27) subjected to (28) and (29) obtained by the proposed algorithm for the variables $X(x)$ and $Y(y)$ respectively. The following parameters are used in the simulation: $a = 2(m)$, $b = 1(m)$, $V_0 = \frac{\pi}{4}(V)$, and $m = 1$. The results are in good agreement with the exact solution especially for greater number of samples.

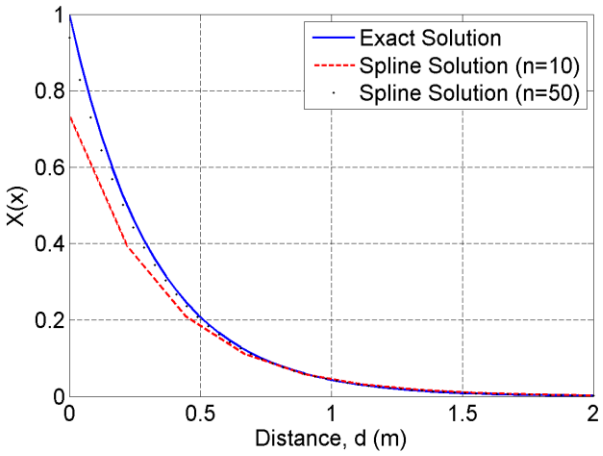

Fig. 5. Simulation results for the partial solution $X(x)$ of the voltage distribution inside a 2D area bounded by electrodes.

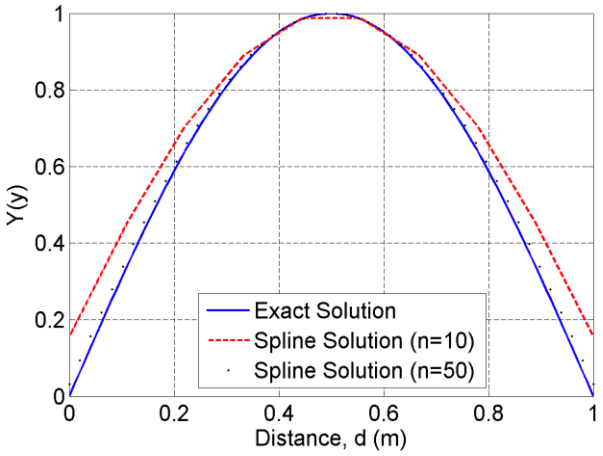

Fig. 6. Simulation results for the partial solution $Y(y)$ of the voltage distribution inside a 2D area bounded by electrodes.

Figure 7 shows the total numeric solution as in (33) obtained by the proposed algorithm for the truncated summation of the first 100 terms.

The stability analysis for the problem in (26) is given in Fig. 8. The results show that this problem can be considered to be well-posed especially for lower

number of samples.

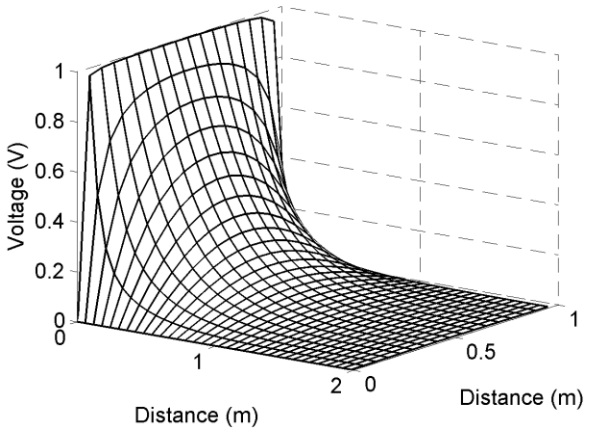

Fig. 7. Simulation results for the voltage distribution inside a 2D area bounded by electrodes.

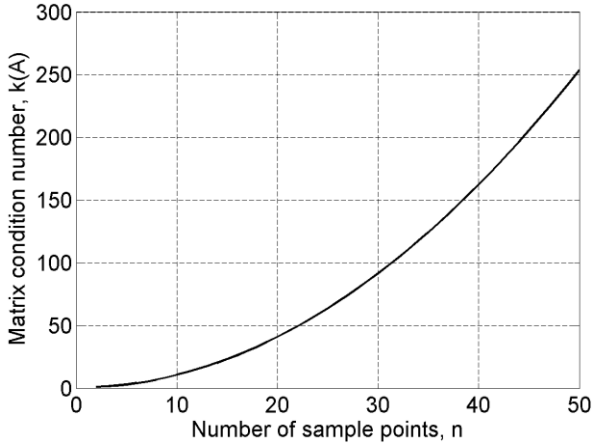

Fig. 8. Stability analysis of the proposed method.

IV. CONCLUSION

The non-polynomial spline approximation has been used to solve 2nd order Neumann type bvp's in electrostatic problems. The method is applicable to linear 2nd order bvp's given by (1), and has proven to give accurate results even for ill-conditioned problems such as the capacitor problem in Section III. The proposed method has been applied specifically to electrostatic problems, although it can also be used to solve any electromagnetic bvp's governed by 2nd order Neumann type differential equations.

REFERENCES

[1] R. Kress, *Numerical Analysis*. Springer-Verlag, New York, 1998.

[2] M. N. O. Sadiku, *Numerical Techniques in Electromagnetics*. CRC Press, New York, 2001.

[3] E. Suli, *Lecture notes on finite element methods for partial differential equations*, Mathematical Institute University of Oxford, 2012.

[4] M. A. Ramadan, I. F. Lashien, and W. K. Zahra, "Polynomial and non-polynomial spline approaches to the numerical solution of second order boundary value problems," *Applied Mathematics and Computation*, vol. 184, pp. 476484, 2007.

[5] H. Caglar, N. Caglar, and K. Elfaituri, "B-spline interpolation compared with finite difference, finite element and finite volume methods which applied to two-point boundary value problems," *Applied Mathematics and Computation*, vol. 175, pp. 72-79, 2006.

[6] K. Aniserowicz, "Comparison of different numerical methods for solving boundary-value problems in electromagnetics," *IEEE Transactions on Education*, vol. 47, pp. 241-246, 2004.

[7] T. C. O'Connell and P. T. Krein, "A time harmonic three-dimensional vector boundary element model for electromechanical devices," *IEEE Transactions on Energy Conversion*, vol. 25, pp. 606-618, 2010.

[8] J. Jin and W. C. Chew, "Variational formulation of electromagnetic boundary value problems involving anisotropic media," *IEEE Antennas and Propagation Society International Symposium*, Seattle, WA, USA, pp. 1752-1755, 1994.

[9] Y. Sirenko and N. Yashina, "Numerical technique of non-stationary electromagnetic theory," *Mathematical Methods in Electromagnetic Theory International Symposium*, Lviv, Ukraine, pp. 275-276, 1996.

[10] D. K. Cheng, *Field and Wave Electromagnetics*. Addison-Wesley Publishing Company, New York, 1989.

[11] A. Pyzara, B. Bylina, and J. Bylina, "The influence of a matrix condition number on iterative methods' convergence," *IEEE Proceedings of the Federated Conference on Computer Science and Information Systems*, Szczecin, Poland, pp. 459-464, 2011.

[12] E. W. Cheney and D. R. Kincaid, *Numerical Mathematics and Computing*. Brooks Cole, 2007.

Goker Sener was born in 1973. He completed his B.S. degree in Electrical Engineering in 1995 at the Wright State University, Dayton OH. He completed his M.S. and Ph.D. degrees in Electrical and Electronics Engineering in 2004 and 2011 at the Middle East Technical University, Ankara, Turkey.

He is currently an Assistant Professor in Cankaya

University Electrical and Electronics Engineering department, Ankara, Turkey. His fields of interest are electromagnetic theory, antennas and numerical techniques.

Correlation Analysis between Multi-Sources in Indoor Corridors and Tunnels

Hany M. El-Maghrabi [1], Samir F. Mahmoud [2], Ahmed M. Attiya [3], Mostafa El-Said [2], and Essam A. Hashish [2]

[1] Department of Electromechanical
Housing and National Research Center, Cairo, Egypt
helmaghrabi@hbrc.edu.eg

[2] Department of Electronics and Electrical Communication
Cairo University, Cairo, Egypt

[3] Department of Microwave Engineering
Electronic Research Institute, Cairo, Egypt
attiya@eri.sci.eg

Abstract ─ In this paper, a model is presented to simulate wave propagation in indoor corridors and tunnels with imperfectly conducting walls. The model is based on the waveguiding effect of corridors and tunnels. This approach is based on assuming that the boundaries of the waveguide section are constant impedance surface as the surface impedance of the wall is almost independent of the angle of the wave incidence onto the wall. An analytical approach for the calculation of the signal correlation between the transmitters and receivers elements in tunnels and indoor corridors is proposed. A new approach for determining the best locations of the indoor access points is introduced based on minimum correlation between sources with minimum cross talk. A scenario is considered in order to check the accuracy of this model. This scenario is verified by comparing experimental and numerical simulation results. Good agreement is achieved.

Index Terms ─ Indoor propagation, signal correlation.

I. INTRODUCTION

In recent years, a lot of attention has been drawn to modelling indoor wave propagation [1-2], in road and mine tunnels [3]. This is especially important in wireless applications because of the large dimensions compared with the operating wavelength and complex geometry of buildings. Predicting wave propagation in indoor environment is especially complicated problem due to the operating wavelength that is usually much smaller than the size of different objects in the normal building in addition to the complicated shapes and structures inside indoor environment. Different models have been developed to predict how indoor environment affects the wave propagation. These models are divided into empirical and theoretical models [4-10].

Recent advances on wireless communication have revived interest on correlation between sources in tunnels [11-18]. Results described in [16] have shown that angular spread of the rays are rather small and one can thus expect a strong correlation between antennas if arrays are used at both ends of the link. The correlation between the receiving array elements increases with distance, while a small correlation is obtained at small distances where the number of modes is large [17]. At large distance from the transmitter, the correlation increases since only few modes interfere; this correlation has a strong impact on the channel capacity [18]. Since small correlation between array elements is an important criterion for Multiple Input Multiple Output (MIMO) systems, in a tunnel, this can lead to arrays that may become prohibitively long [17].

In this paper, a model based on 3D waveguide model for simulating long corridor sections and tunnels is proposed. This approach is based on assuming that the boundaries of the waveguide section are constant impedance surface as the surface impedance of the wall is almost independent of the angle of the wave incidence onto the wall. An analytical approach for the calculation of the signal correlation between the transmitters and receivers elements is proposed. The effect of the transmitter and receiver locations on the signal correlation is presented. A new approach for determining the best locations of the indoor access points is introduced based on minimum correlation between sources and minimum cross talk. Full wave numerical analysis of the same problem based on FEKO [19] simulation is used to verify the obtained results. Experimental results are also conducted with a simple dipole antenna in a specific office corridor to verify the

Submitted On: July 25, 2016
Accepted On: March 27, 2017

obtained theory.

II. MODAL ANALYSIS OF INDOOR PROPAGATION BASED ON CONSTANT WALL IMPEDANCE BOUNDARY CONDITIONS

Corridors in indoor environment and tunnels can be represented as a combination of multi-mode rectangular waveguide sections as shown in Fig. 1. The excitation source is assumed to be a dipole located at the waveguide section. The proposed model is introduced by Mahmoud [20-21]. The model is based on assuming that the boundaries of the waveguide section are constant impedance surface as the surface impedance of the wall is almost independent of the longitudinal phase constant k_z.

Following [20-21], consider a rectangular guide of width w and height h and the outer medium of complex relative permittivity $\varepsilon_c = \varepsilon_r - i\sigma/\omega\varepsilon_0$ as shown in Fig. 1 (b). When the operating frequency is sufficiently high such that the tunnel dimensions are much greater than the free space wavelength λ_0, the low order modes in the tunnel are characterized by $k_x \ll k_0$ and $k_y \ll k_0$, where k_0 is the free space wavenumber, k_x and k_y are the wavenumbers in the x and y directions. Under these conditions, the tunnel walls are accurately modelled by normalized constant surface impedance Z_s and admittance Y_s relating the transverse and longitudinal field components. The Z_s and Y_s are defined by [20]:

$$Z_s = 1/\sqrt{\varepsilon_r - 1 - i\sigma/\omega\varepsilon_0}, \quad (1)$$

$$Y_s = (\varepsilon_r - i\sigma/\omega\varepsilon_0)/\sqrt{\varepsilon_r - 1 - i\sigma/\omega\varepsilon_0}, \quad (2)$$

where ε_r is the corridor walls relative permittivity and σ is the corridor walls conductivity. The total fields(E, H) are expressed as a sum over the natural modes in the corridor/tunnel. For a TM_y, or a vertically polarized mode, $E_x = 0$ and E_y may given, for an even mode by:

$$\mathbf{E}_y^{TM}(x, y, z) = \sum\sum A_{mn} e_{mn}(x, y)\, exp(-jk_z z), \quad (3)$$

where A is the excitation coefficients and $e_{mn}(x, y)$ are the transverse eigenfunctions, given by:

$$e_{mn}(x, y) = \cos(k_{xm}x)\cos(k_{yn}y), \quad (4)$$

where k_x and k_y are the transverse wave numbers in the walls given as below [20]:

$$k_{yn}h = n\pi[1 + j2Y_s/k_0 h], \quad (5)$$

$$k_{xm}h = m\pi[1 + j2Z_s/k_0 w], \quad (6)$$

where m and n =1,3, … are odd integers for the even modes considered. In the above: $k_y^2 + k_x^2 = k_0^2 - {k_z}^2$ because the guide is oversized relative to the wavelength, both k_x and k_y are $\ll k_0$ and k_z for the low order modes. The E_z component is obtained from the divergence equation $\nabla \cdot \bar{E} = 0$, hence,

$$jk_z E_z = \partial E_y/\partial y, \quad (7)$$

which shows that E_z is of the first order smallness relative to E_y. The magnetic field components are obtained as:

$$\eta_0 H_x = -k_z E_y/k_0\,, \eta_0 H_y \approx 0, \text{ and}$$

$$\eta_0 H_z = j\partial E_y/k_0 \partial x, \quad (8)$$

where terms of the second order smallness have been neglected (such as $k_x k_y/k_0^2$). Same analysis can be followed to obtain the TE, horizontally polarized case.

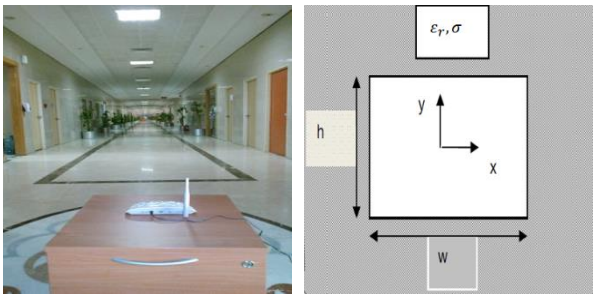

(a) (b)

Fig. 1. (a) Schematic drawing of an example for an indoor corridor environment, and (b) equivalent waveguide representation [20].

Full wave numerical analysis based on FEKO Ray Launching Geometrical Optics (RL-GO) [19] simulator is used to verify this technique for long corridor section. FEKO's RL-GO [19] method is a ray-based technique that models objects based on optical propagation, reflection and refraction theory [23-24]. GO (ray launching) is formulated for use in instances where electrically very large (>20λ) metallic or dielectric structures are modelled. Ray-interactions with metallic and dielectric structures are modelled using Huygens sources, placed at each ray, contact point on material boundaries. The ray-launching process is easily controlled, based on the angular spacing (for localized sources) or transverse spacing (for plane wave sources) of the rays and the number of multiple interactions allowed.

Figure 2 shows the electric field distribution for a corridor section with imperfectly conducting walls. The operating frequency is assumed to be 0.90 GHz corresponding to the lower GSM band. The length, width and height of the corridor are assumed to be 100 m, 5 m and 3 m respectively. The permittivity of the walls is 3 and conductivity is σ=0.01 s/m [22]. The section is excited by a unit y-directed dipole which is located at the point (2.5 m, 1.5 m, 0.5 m).

Figure 2 (a) shows the magnitude of the normalized electric field in the plane parallel to the ground at a height 2.25 m. On the other hand, Figure 2 (b) shows the corresponding normalized electric field distribution for the equivalent constant impedance walls rectangular waveguide section. The percentage of the difference between Fig. 2 (a) and Fig. 2 (b) is calculated by using Mathematica. By comparing the simulation and model

results, it is found that the error is about 8.57%. The model is developed in Matlab which runs on a laptop with an Intel 2.4 GHz processor, 8 GB of RAM and Windows 8.1 64-bit; the total program runtime for the above example is only 2 minutes. On the other hand, the same example is simulated using simulation package FEKO version 7.0 with the same computer resources. It is found that the simulation takes about 23 minutes using FEKO RL-GO solver. It can be noted that the proposed model is faster than the simulation package and the difference will be increased by increasing the dimensions or operating frequency.

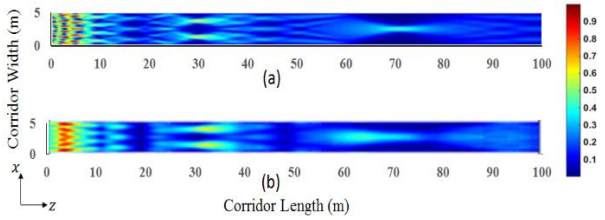

Fig. 2. Magnitude of normalized electric field, x-z plane, for two corridor segments at frequency band 0.90 GHz: (a) FEKO model, and (b) constant wall impedance model.

III. SPACE AND FREQUENCY CORRELATION BETWEEN MULTI-SOURCES

In this section the correlation between the electric field excited by two array elements is discussed [11-15]. This is a critical tool for optimizing the location of the transmitters with minimum cross talk as to obtain best coverage and minimize dead zones. The correlation coefficient $\rho^{E}_{j_1 j_2}(z)$ between the electric field produced by the transmitting elements j_1 and j_2, and received in a transverse plane at an axial distance z is obtained by:

$$\rho^{E}_{j_1 j_2}(z) = \frac{\iint_{xy} E_{j_1} \cdot E^{*}_{j_2}\, dx\, dy}{\sqrt{\iint_{xy} |E_{j_1}|^2\, dx\, dy \iint_{xy} |E_{j_2}|^2\, dx\, dy}}, \qquad (9)$$

where E_{jx} is electric field for the corresponding source which can be obtained using the proposed model.

The correlation between sources is calculated for space diversity in the transverse and axial planes, where in the transverse plane both the source elements are fixed in the transverse plane with Δd spacing between them and the correlation is calculated between the electric field received in the transverse plane, x-y plane, at distance z from the transmitters, while for the latter one, the transmitters are in the axial plane with Δz and the correlation is calculated between the to the electric field received in the x-z plane. On the other hand, frequency correlation between sources is calculated at different frequency bands, channels, as to optimize the operating frequency channels of the sources with minimum cross talk and phase difference between received signals.

A. Transvers correlation

Transverse correlation is the correlation between sources that are located in the corridor/tunnel transverse plane [13] and it is calculated from the values of the electric field in a transverse plane. In order to verify the proposed formula for the correlation of Equation (9), a comparison with previously published results is presented. Figure 3 shows the correlation coefficient between adjacent elements at 0.9 GHz band for two cases, where the elements are λ and 2λ apart [12]. The tunnel is rectangular in shape with width and height of 4 m and 4.5 m, respectively. The maximum axial distance from the transmitter is 600 m. The transmitters in the tunnel are 50 cm from the ceiling and at 1/8 of the tunnel width from the side wall.

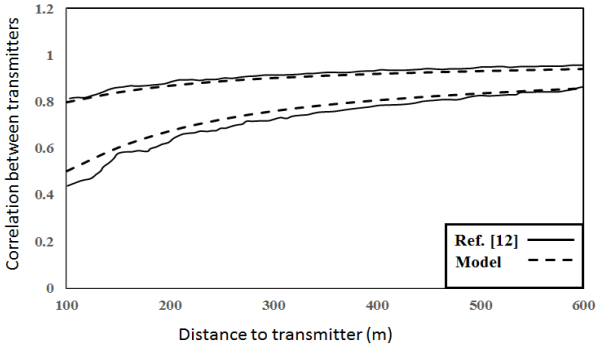

Fig. 3. Average correlation between the electric field produced by the two transmitters in the a tunnel for different spacing$(\lambda, 2\lambda)$, f =0.90 GHz, $\varepsilon_r = 5, \sigma = 0.01$.

B. Axial correlation

One of the most important challenges in indoor propagation is to determine the location of the transmitters or access points (AP), so as to guarantee maximum signal coverage. Axial correlation is an important tool for determining such locations of the APs with minimum cross talk as it is calculated from the values of the electric field in the axial plane, x-z plane, due to transmitters with Δz spacing along the axis of the corridor. To study this point, it is required to calculate, for a given frequency, the amplitude ρ of the complex correlation coefficient between two sources (j_1, j_2) with Δz separation down the corridor axis using Eq. (9), where the electric field in the x-z plane is calculated due to sources along the corridor axis and numerically integrated to calculate the correlation between the two sources.

Figure 4 shows the electric field correlation coefficient for two transmitters along the corridor axis with different spacing. The adjacent sources are 1 m to 85 m apart. The corridor width, height and length are 3 m, 3 m and 100 m, respectively. The walls permittivity is 3 and conductivity is 0.01 S/m [22]. It can be noted from Fig. 4 that, the correlation coefficient has peaks at

some points. These points should be avoided when designing the locations of the access points. In order to check the effect of the correlation value on the electric field distribution, the electric field is calculated using FEKO for the mentioned corridor with two sources, where the calculation is repeated for two cases; in the first case the sources are 25 m apart and the second one the sources are 45 m apart.

Figure 5 (a) shows the magnitude of the simulated electric field in the plane parallel to the ground at a height 1.5 m from the ground with transmitter locations at z = 1 m and 46 m, respectively. On the other hand, Fig. 5 (b) shows the magnitude of the electric field with transmitter locations at z = 1 m and 26 m, respectively. It can be noted that the zones with almost no signal are less in Fig. 5 (a) than in Fig. 5 (b). Thus, electric field distribution for the case of minimum correlation between the transmitters is better than the case with higher correlation. It can be concluded from the above discussion, that the correlation coefficient between transmitters is a good tool for planning appropriate wireless links in indoor environment with optimum access point location.

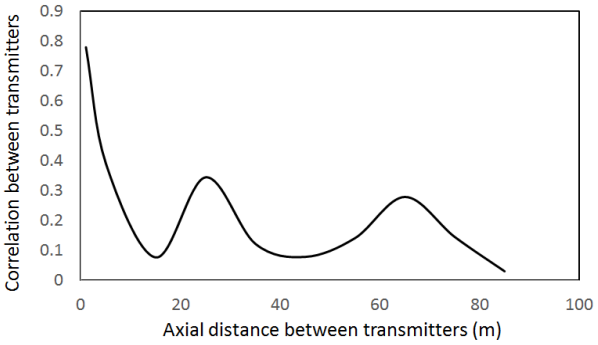

Fig. 4. Average correlation between the electric field produced by the two Transmitters in the corridor for different spacing (from 1 m to 85 m apart), $f = 0.9$ GHz, $\varepsilon_r = 3, \sigma = 0.01$.

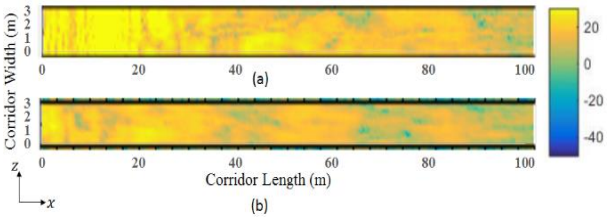

Fig. 5. Electric field distribution in $dB\mu V/m$ for x-z plane. (a) Field distribution for transmitter at locations at z = 1 m and 46 m. (b) Field distribution for transmitter locations at z = 1 m and 26 m.

C. Frequency correlation

Frequency correlation between sources is calculated at different frequency bands or channels, in order to optimize the operating frequencies for minimum cross talk between received signals. The same simulation example previously discussed is repeated for two frequency bands to calculate correlation between two sources with frequency steps Δf, where the two sources are at same position while the operating base frequency for the first band is $f_0 = 0.9\ GHz$ and for the second case $f_0 = 2.4\ GHz$. One of the two sources will be configured to operate in the base band while the other source is operating with higher frequency $f = f_0 + \Delta f$, where Δf is changed from 10 MHz to 100 MHz.

Figure 6 shows the electric field correlation coefficient between the sources due to frequency diversity at two frequency bands. It can be noted that the correlation decreases at higher operating band.

It can be concluded that correlation between transmitters can be reduced by either using space diversity, frequency diversity or by combining both. It should be noted that the optimal locations of indoor access points in corridors are these locations with minimum correlation between transmitters where the cross talk between transmitters is minimum and signal quality is better.

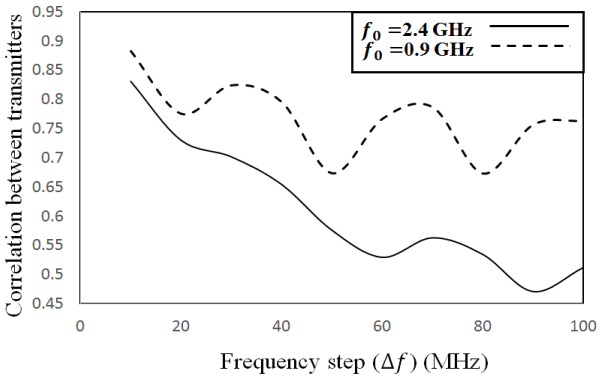

Fig. 6. Average correlation between the electric field produced by the two Transmitters in the corridor for different frequency bands, $f = 0.9$ GHz, 2.4 GHz, $\varepsilon_r = 5$, $\sigma = 0.01$.

IV. MEASUREMENTS

In this section sample results are presented to verify the accuracy of the present model by comparing the obtained results with measurement results. The proposed model is used to simulate indoor propagation in long corridor section with imperfectly conducting walls and to calculate the correlation between two sources.

This scenario of a straight corridor section is verified experimentally at Wi-Fi frequency 2.4 GHz in corridor of commercial building with gypsum walls. The experimental setup consists of three wooden carts. One cart is used to hold the first transmitting antenna and the transmitter and the second one is used to hold the second transmitter, while the third is used to hold the receiving

antenna, the receiver and data collecting computer as shown in Fig. 7. TP-LINK TL-WA701ND access points with dipole antenna with gain of 5 dBi are used as transmitters. The transmitting and receiving antennas are kept vertically polarized. The measurements were taken with one transmitter located at a fixed location and the other transmitter moving into 5 m steps along a straight line away from the first transmitter, while receiver is moved along the corridor to measure the axial correlation between the transmitters. Figure 7 shows the locations of the transmitters and the receiver for the relevant measurements. The length of the corridor is about 100 m while the width and height are 3.7 m and 3.4 m, respectively. The building walls is gypsum walls with permittivity 2.4 and conductivity 0.08 [25]. The heights of both receiving and transmitting antennas are kept 60 cm above the ground.

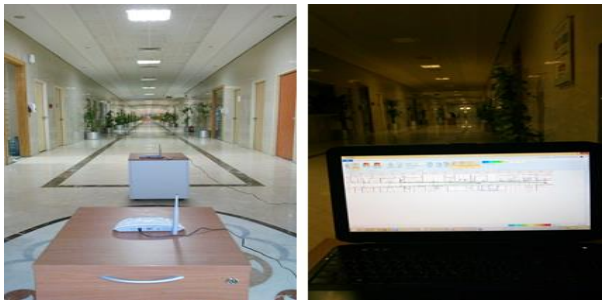

Fig. 7. Measurement setup in corridor section

Figure 8 shows a comparison between the measured received power in dBm and calculated power by using proposed modal analysis. Good agreement between the calculated and the measured power is obtained. The slight differences can be explained as errors in the positioning of the antenna and differences due to the boundary conditions of the actual corridor. The calculated error between the model and measured results is about 9.029%.

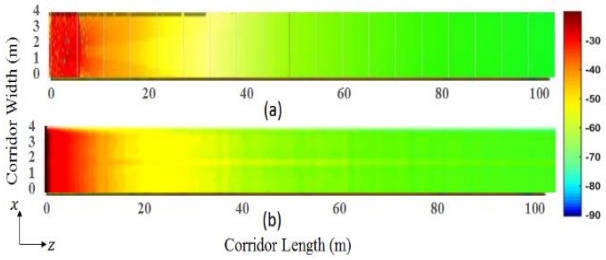

Fig. 8. Received power distribution (dBm) across the corridor. (a) Measured power strength, and (b) calculated power strength using modal analysis.

On the other hand, Fig. 9 shows a comparison between the measured and calculated correlation by proposed analytical model. The calculated error between the measured and model results is about 9.3%. It should be noted that the correlation is minimum at 40 m which can be the best location of the access point with minimum cross talk.

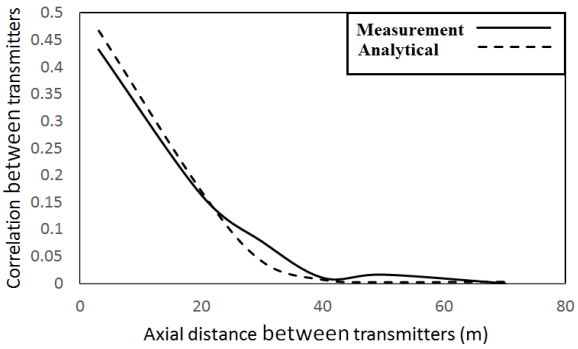

Fig. 9. Average correlation between the received power of two transmitters in the corridor with different axial spacing (from 3 m to 70 m apart), $f = 2.48$ GHz.

The same setup is used to test the model for corridor segment with another hotel building with brick walls with permittivity 3.73 and conductivity 0.37 S/m [25] as shown in Fig. 10. In this case the corridor width is 3.1 m and height is 2.8 m, while the length is about 35 m. The measurements were taken with one transmitter located at a fixed location and the other transmitter moving into 5 m steps along a straight line away from the first transmitter while receiver is moved along the corridor to measure the axial correlation between the transmitters. The axial distance between the transmitters is from 5 m to 30 m.

Figure 11 shows a comparison between the measured and calculated correlation by proposed analytical model. The calculated error between the model and measured results is about 8%. It should be noted that the correlation is lower than 0.2 at 15 m which can be the best location of the access point with minimum cross talk for location after 15 m aside.

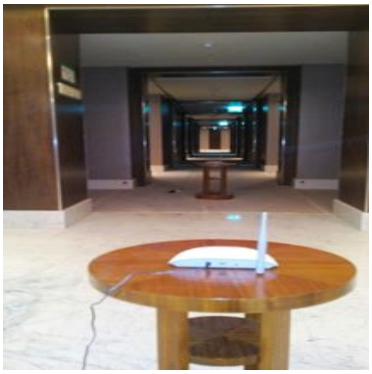

Fig. 10. Measurement setup in hotel.

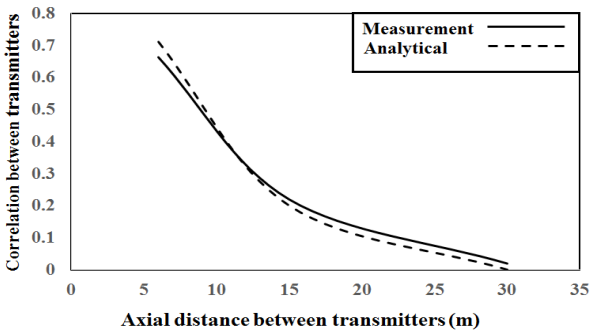

Fig. 11. Average correlation between the received power of two transmitters in the corridor with different axial spacing apart (from 5 m to 30 m apart), $f = 2.48$ GHz.

It should be deduced from the presented approach that designers of indoor wireless system should consider the optimal location of the access point that corresponds to minimum correlation between sources. Also it can be concluded that the proposed model is a good tool for designing indoor wireless system with high accuracy and low computational resources.

V. CONCLUSION

A model based on 3D waveguide model for simulating long corridor sections and tunnels is proposed. This approach is based on assuming that the boundaries of the waveguide section are constant impedance surfaces. Space and frequency correlation between transmitters are presented. A new approach for determining the best locations of the indoor access points is introduced based on minimum correlation between sources and minimum cross talk. It can be deduced, that the correlation coefficient between transmitters is a good tool for planning appropriate wireless links in indoor environment with optimum access point location. The results of the presented model are verified by comparison with numerical results and experimental results. Good agreements are obtained from these comparisons.

REFERENCES

[1] M. Ayadi, A. Ben Zeinab, and S. Tabbane, "A novel approach for indoor wave propagation modeling," *Wireless Communications and Mobile Computing Conference (IWCMC)*, pp. 1544-1547, Aug. 2015.

[2] M. A. Erol, S. S. Seker, F. Kunter, and A. Y. Citkaya, "Optimized indoor propagation model for office environment at GSM frequencies," *Antennas and Propagation in Wireless Communications (APWC)*, pp 1284-1287, Sep. 2015.

[3] D. G. Dudley, M. Lienard, S. F. Mahmoud, and P. Degauque, "Wireless propagation in tunnels," *IEEE Antennas Propag. Mag*., vol. 49, no. 2, pp. 11-26, Apr. 2007.

[4] J. Andersen, T. Rappaport, and S. Yoshida, "Propagation measurements and models for wireless communications channels," *IEEE Communications Mag*., vol. 33, no. 1, pp. 42-49, Jan. 1995.

[5] J. Medbo and J. E. Berg, "Simple and accurate path loss modeling at 5 GHz in complex indoor environments with Corridors," *Proc. of COST Conference 273*, Espoo, Finland, pp. 30-36, May 2002.

[6] A. M. Najafi, *Indoor propagation path loss measurements and empirical models for 2.4 GHz*, M.Sc. Dissertation, Royal Institute of Technology and Ericsson Research, Stockholm Sweden, Nov. 2011.

[7] S. Sidhu, A. Khosla, and A. Sharma, "Implementation of 3-D Ray tracing propagation model for indoor wireless communication," *International Journal of Electronics Engineering*, vol. 4, pp. 43-47, Apr. 2012.

[8] J. Zhong, L. Bin-Hong, W. Hao-Xing, C. Hsing-Yi, and K. Sarkar, "Efficient Ray-tracing methods for propagation prediction for indoor wireless communications," *IEEE Antenna and Propagations Mag*., vol. 43, no. 2,pp. 41-49, Apr. 2003.

[9] P. Kyritsi, *Multiple element antenna systems in an indoor environment*, Ph.D. dissertation, Stanford University, 2001.

[10] D. Porrat and D. Cox, "UHF propagation in indoor hallways," *IEEE Transactions on Wireless Communications*, pp.1188-1198, July 2002.

[11] J.-M. Molina-Garcia-Pardo, M. Lienard, and P. Degauque, "Propagation in tunnels: Experimental investigations and channel modeling in a wide frequency band for MIMO applications," *EURASIP J. Wireless Commun. Netw*., vol. 2009, pp. 560-571, 2009.

[12] J.-M. Molina-Garcia-Pardo, M. Liénard, P. Degauque, D. Dudley, and L. J. Llácer, "Interpretation of MIMO channel characteristics in rectangular tunnels from modal theory," *IEEE Trans. Veh. Technol.*, vol. 57, no. 3, pp. 1974-1979, Apr. 2008.

[13] M. Lienard, C. Sanchis-Borras, J. M. Molina-Garcia-Pardo, D. P. Gaillot, P. Laly, and P. Degauque, "Performance analysis of antenna arrays in tunnel environment," *IEEE Antennas and Wireless Propagation Letters*, vol. 13, no. 3, pp. 122-125, Jan. 2014.

[14] M. Liénard, P. Degauque, J. Baudet, and D. Degardin "Investigation on MIMO channels in subway tunnels," *IEEE Journal on Selected Areas in Comm.*, vol. 21, no. 3, Apr. 2003.

[15] M. Lienard, J. M. Molina-Garcia-Pardo, C. Sanchis-Borras, and P. Degauque, "Impact of spacing between array elements on the

performances of diversity schemes in tunnels," *Latest Trends on Communications*, 2014.
[16] M. Lienard, J. M. Molina-Garcia-Pardo, P. Laly, C. Sanchis-Borras, and P. Degauque, "Communication in tunnel: Channel characteristics and performance of diversity schemes," *IEEE General Assembly and Scientific Symposium*, Beijing, 16-23 Aug. 2014.
[17] M. Lienard, J. M. Molina-Garcia-Pardo, P. Laly, C. Sanchis-Borras, and P. Degauque, "MIMO and diversity techniques in tunnels," *International Conference on Computing, Management and Telecommunications (ComManTel)*, 27-29 Apr. 2014.
[18] J. Molina-García-Pardo, M. Lienard, P. Degauque, C. García-Pardo, and L. Juan-Llácer, "MIMO channel capacity with polarization diversity in arched tunnels," *IEEE Anetnnas and Wireless Propagation Letters*, vol. 8, 2009.
[19] FEKO Suite 7.0, Altair Engineering, 2014.
[20] S.F. Mahmoud, *Wireless Transmission in Tunnels*. Mobile and Wireless Communications Physical Layer Development and Implementation, InTech 2010.
[21] S. F. Mahmoud "Modal propagation of high frequency electromagnetic waves in straight and curved tunnels within the earth" *J. of Electromagn. Waves and Appl*., vol. 19, no. 12, pp. 1611-1627, 2005.
[22] J. Leung, *Hybrid waveguide theory-based modeling of indoor wireless propagation*, M.Sc. Dissertation, Department of Electrical and Computer Engineering, University of Toronto, 2009.
[23] J. B. Keller, "Geometrical theory of diffraction," *J. Opt. Soc. Amer*., vol. 52, pp. 116-130, Feb. 1962.
[24] R. Akl, D. Tummala, and X. Li "Indoor propagation modeling at 2.4 GHz for IEEE 802.11 networks," *The Six IASTED International Muti-Conference on Wireless and Optical Communication*, 3-5 July 2006, Banff, AB, Canada.
[25] Laszlo Solymar and Donald Walsh, *Electrical Properties of Materials*. Oxford 2009.

Hany M. El-Maghrabi received the B.S. degree, with Honor Degree, and M.S. degree in Electrical Engineering from the Cairo University (Egypt). Hany has got a position of Research Assistant in Housing and Building National Research Center (HBNRC), Institute of Electromechanical, Department of Communication (Egypt) at 2005. He became Assistant Researcher at HBNRC at 2011. He has co-authored technical journal article and conference papers. Hany has an experience in electromagnetics, antennas, microstrip structures, numerical methods, wave propgation and their applications in microwave. Hany was awarded the Best Paper in NRSC 2015.

Samir F. Mahmoud graduated from the Electronic Engineering Dept., Cairo University, Egypt in 1964. He received the M.Sc. and Ph.D. degrees in the Electrical Engineering Department, Queen's University, Kingston, Ontario, Canada in 1970 and 1973. During the academic year 1973-1974, he was a Visiting Research Fellow at the Cooperative Institute for Research in Environmental Sciences (CIRES) Boulder, CO, doing research on Communication in Tunnels. He spent two sabbatical years, 1980-1982, between Queen's Mary College, London and the British Aerospace, Stevenage, where he was involved in design of antennas for satellite communication. He spent several years as Professor at the EE Department, Kuwait University. Currently Mahmoud is a Full Professor at the Electronic and Telecommunication Engineering Department, Cairo University. Recently, he has visited several places including Interuniversity Micro-Electronics Centre (IMEC), Leuven, Belgium and spent a sabbatical leave at Queen's University and the Royal Military College, Kingston, Ontario, Canada in 2001-2002. His research activities have been in the areas of antennas, geophysics, tunnel communication, and e.m wave interaction with composite materials. Mahmoud is a Fellow of IET and one of the recipients of the Best IEEE/MTT Paper for 2003.

Ahmed M. Attiya received his M.Sc. and Ph.D. in Electronics and Electrical Communications, Faculty of Engineering, Cairo University in 1996 and 2001 respectively. He joined Electronics Research Institute as a Researcher Assistant in 1991. In the period from 2002 to 2004, he was a Postdoc in Bradley Department of Electrical and Computer Engineering at Virginia Tech. In the period from 2004 to 2005, he was a Visiting Scholar in Electrical Engineering Dept. in University of Mississippi. In the period from 2008 to 2012, he was a Visiting Teaching Member in King Saud University. He is currently Full Professor and the Head of Microwave Engineering Dept. in Electronics Research Institute.

Mostafa El-Said graduated from the Electronic Engineering Dept., Cairo University, Egypt in 1963. He received the Dipl.Ing and Dr.Ing. degrees from Karlsruhe University, West Germany, in 1970 and 1974. Since 1992, he is Professor at the Electronic Engineering and Telecommunication Department Cairo University. His research activities have been in the areas of microstrip, wave propagation and nano technology.

Essam A. Hashish (M'96) received the B.Sc., M.Sc., and Ph.D. degrees from the Electronics and Communications Department, Faculty of Engineering, Cairo University, Giza, Egypt, in 1973, 1977, and 1985, respectively. He is currently a Professor with the Electromagnetics Group at the same department. His main interest is electromagnetic remote sensing, wave propagation, and microwave antennas.

Notch Antenna Analysis: Artificial Neural Network-based Operating Frequency Estimator

Kadir Sabanci, Ahmet Kayabasi, Abdurrahim Toktas, and Enes Yigit

Department of Electrical and Electronics Engineering
Engineering Faculty, Karamanoglu Mehmetbey University, 70100, Karaman, Turkey
kadirsabanci@kmu.edu.tr, ahmetkayabasi@kmu.edu.tr, atoktas@kmu.edu.tr, enesyigit@kmu.edu.tr

Abstract ─ An artificial neural network (ANN) based estimator is presented for notch antenna analysis in terms of the operating frequency. The notch antenna is formed by loading an asymmetric slot on one side of a rectangular patch. Architecture of the estimator is constructed over an ANN model trained with the simulated data of the notch antennas. In order to constitute a data pool for training and testing the ANN model, 96 notch antennas with seven antenna parameters are simulated with respect to the operating frequency. Antenna parameters including the patch dimensions, height and relative permittivity of the substrate are used as input vector of the ANN model. The simulated data of 80 notch antennas are employed to train the ANN model. The estimator is corroborated through testing with the remainders 16 antenna data, verifying with antenna data in the literature and validating with a prototyped notch antenna data. The results show that the estimator simply and fast computes the operating frequency of the notch antennas in very close to real one without performing simulations or measurement.

Index Terms ─ Antenna, antenna analysis, Artificial Neural Network (ANN), estimator, notch antenna, operating frequency, patch antenna.

I. INTRODUCTION

Slot loading technique are widely used to form small and comfortable patch antennas suitable for modern wireless technologies, since it yields a miniaturization in size and tuning the operating frequency [1-13]. Therefore, various slot antennas with *C* [1-4], *E* [5, 6], *H* [1, 7], *L* [8, 9] and rectangular ring [1, 10] shapes are well studied in the literature. The slots of those antennas are loaded in symmetrical with respect to the edge of the patch. However, notch antenna is a form of slot antenna constituted by asymmetrical notching one side of the patch [11]. Thus, lower operating frequency according to rectangular patch antenna can be achieved by notching the patch with the same outer size. Note that the analysis of such antennas needs great effort because of having irregular shapes. There exist several analytic techniques like cavity model [12] and transmission line model [13] inspired from waveguide and transmission line theory, especially for regular shapes such as rectangular, triangular and circular. However, the mentioned techniques could not be employed to analyze the slot antennas alone. Nevertheless, analysis of the slot antennas may be facilitated thanks to computer-based software incorporated with computational electromagnetic (CEM) [14]. The CEMs generally employ complicated numerical method such as finite difference time domain (FDTD) [15] and method of moment (MoM) [16]. CEMs numerically solve the rigorous Maxwell equations in integral or differential forms by discretizing simulated model. On the other hand, the ownership cost of the CEM-based simulation tools are very expensive and one requires deep background knowledge to model and simulate an antenna. Therefore, finding alternative ways for simply analyzing the antennas, especially determining the operating frequency is promising research. Expert systems using artificial intelligence are interesting methods being developed for analyzing the antenna structures [4, 6, 9, 10, 17-20] and estimating various antenna parameters. The well-known computer-based artificial intelligent techniques are the artificial neural network (ANN) [21] and the adaptive neuro-fuzzy interference system (ANFIS) [22] and the support vector machine (SVM) [23].

ANN has evolved in various engineering applications owing to being accurate simulation and modelling with fast and simple manner. It has remarkably advanced in field of wireless communication as well. ANN contains artificial neurons designed into several layers. The neurons resembling the human brain are the processing elements of the network and they consist of non-linear types of functions that are mutually connected by synaptic weights. ANN can be trained through measured or simulated data pool having inputs and outputs with respect to objective of minimizing the error between target and output. During the training, the synaptic weights weaken or strengthen to bring closer output to the target. Meanwhile, the ANN is modelling the nonlinear relationship between the output and the target

Submitted On: January 12, 2017
Accepted On: March 6, 2017

by utilizing some mathematical functions.

In this study, a robust ANN-based estimator for operating frequency is proposed. To this end, a notch antenna is formed and the estimator built on multilayer perceptron (MLP) [21, 24] is constructed for analyzing the antenna. The notch antenna is designed with six physical parameters and a relative permittivity of the substrate. To generate the training and testing data pool, 96 notch antenna with different parameters are simulated in terms of operating frequency by using a CEM software. The simulated data of 80 notch antenna representing the overall problem space is employed to train the estimator and the remainders 16 are utilized to test the accuracy. Hence, the estimator is successfully trained with mean absolute errors (MAE) of 0.003. The estimator is then tested through 16 testing data with MAE of 0.022, and verified via 19 simulated and measured data of notch antennas reported elsewhere [1, 3, 4, 11] with MAE of 0.023. Finally, the proposed estimator is validated using notch antenna prototyped in this study.

II. DESIGN OF NOTCH ANTENNA STRUCTURE

The geometry of the notch antenna is illustrated in Fig. 1. The antenna consists of a rectangular patch of *LxW* fed by a probe feed, ground layer, substrate with *h* thickness and ε_r relative permittivity therein between the patch and ground layer. The probe feed is positioned in the point of (x_0, y_0). The rectangular patch is loaded with a *lxw* slot shifted as *d* from the upper side.

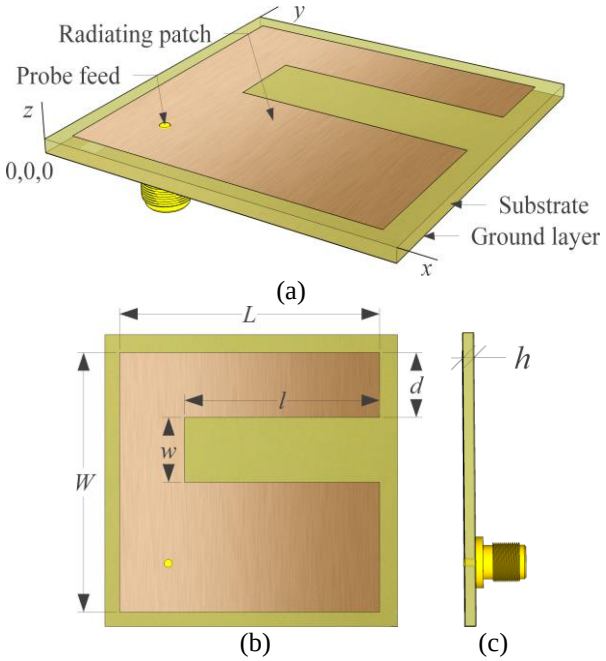

Fig. 1. Geometry of the notch antenna: (a) 3D view, (b) front view, and (c) side view.

III. CONSTRUCTING THE ESTIMATOR

The construction of operating frequency estimator is outlined in Fig. 2. The notch antenna with 7 parameters are simulated to determine the operating frequency (f_{sim}), which is the target of the ANN model. These antenna parameters are also used as input vector of the ANN model so as to estimate the operating frequency (f_{est}). The ANN model is trained with 80 antenna data so that fitting the estimator's outputs to simulated operating frequency in the objective of minimizing MAE calculating the mean absolute error between the target and output.

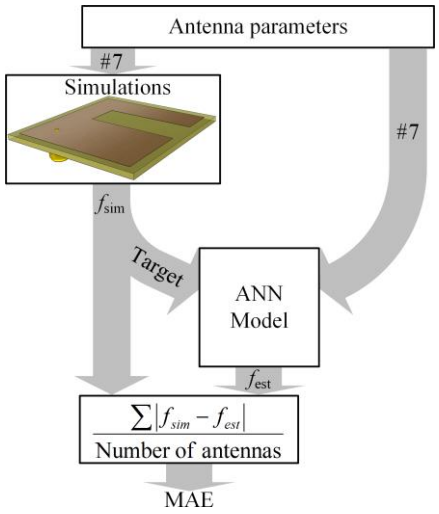

Fig. 2. The working principle of the estimator.

A. Simulations

Simulations of 96 notch antennas are performed with respect to the operating frequency according to parameters given in Table 1. The antennas' parameters are determined so that they operate between 1.15 GHz and 3.35 GHz, which appropriates to ultra-high frequency (UHF) band applications. The notch antenna structures are modelled and simulated by means of CEM software HyperLynx® 3D EM [25] running method of moment (MoM). In order to constitute a uniformly distributed data pool, the outer dimensions (*L* and *W*) are selected in three groups each of which has 32 antenna, and the outer dimensions of the groups are 30, 20; 40, 30 and 50, 40, including different parameters of *l*, *w*, *d*, *h* and relative permittivity ε_r. In the simulations, the antennas are fed with a probe of 1 Volt wave source in the point of x_0=5 mm, y_0=5 mm. The antenna models are meshed with lines per wavelength ratio of 30 and maximum frequency of 5 GHz. It is simulated at the frequency range of 1 GHz and 5 GHz on 81 discrete frequency points.

B. The ANN model

The ANN model is constructed over MLP with 3 layers as shown in Fig. 3. In the MLP, the neurons are

inter-connected in feed forward back propagation (FFBP).

The layers of input, hidden and output layers have 7, 4 and 1 neurons, respectively. In order to investigate a proper model, networks with higher hidden layers are also essayed. However, merely slightly improvement is achieved with those networks rather than with single hidden layer. Therefore, the network with single hidden layer is preferred for the sake of simplicity. For both input and hidden layers, "tangent sigmoid" function is used; in output layer "purelin" function is utilized.

Table 1: Simulated notch antenna parameters

Patch Dimension (mm)					h (mm)	ε_r
L	W	l	w	d		
30	20	10; 20	5; 10	3; 6	1.6; 2.5	2.33; 4.4
40	30	15; 30	7.5; 15	5; 10		
50	40	20; 40	10; 20	7; 14		

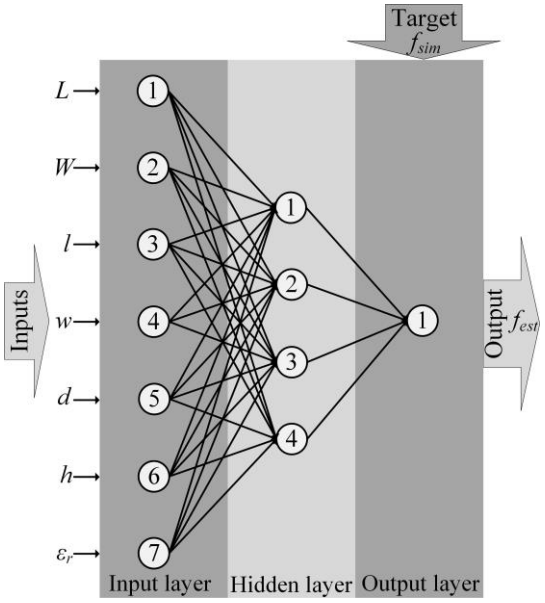

Fig. 3. The proposed ANN model.

C. Training the ANN model

The ANN model is trained with Levenberg-Marquardt learning algorithm [26-28] according to the flowchart given in Fig. 4. Training data set in Table 1 with respective operating frequency values is firstly loaded once starting the algorithm. Training of the ANN starts with a random seed value and it is being trained through the loaded data for 350 epochs, which is the number of return cycles in this step. Seed value is a factor that fixes the weights of the network for getting the same result in every run. After training the model, if MAE is less than objective values of 0.005; the seed value is saved for subsequent runs of the trained ANN. Otherwise, the training repeat with a new random seed value. Therefore, the ANN model is properly trained with MAE of 0.003. In the proposed ANN model, learning coefficient, epoch number, momentum parameter and seed number are determined as 0.5, 350, 0.001 and 1681524111, respectively.

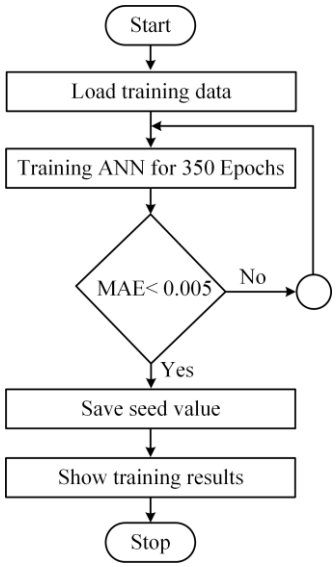

Fig. 4. Flowchart for training the ANN model.

IV. CORROBORATING THE ESTIMATOR

The estimator is corroborated via a graphical user interface (GUI) created in MATLAB® software as given in Fig. 5. The trained estimator is corroborated in three phase: testing with simulated data, verifying with simulated/ measured data in the literature and validating with data of a prototyped notch antenna in this study.

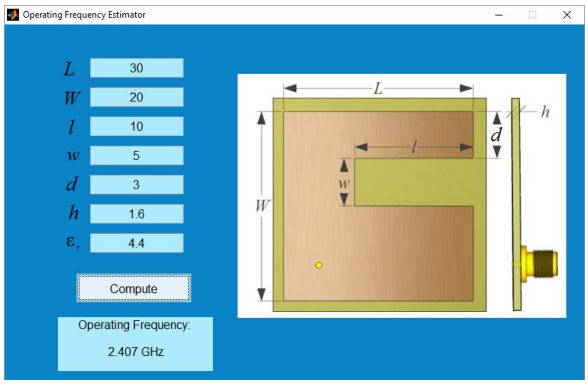

Fig. 5. A screenshot for GUI of the estimator.

A. Testing the estimator

The accuracy of the estimator is tested through 16 notch antenna data that is not utilized in training the estimator. Parameters of 16 simulated antennas with respective operating frequency values are given in

Table 2. The trained estimator successfully computes the frequency (f_{est}) with MAE of 0.022.

B. Verifying the estimator

The proposed estimator is verified over the simulated and measured results reported elsewhere [1, 3-4, 11]. Data of 19 notch antennas including parameters with respective simulated and measured operating frequency values are tabulated in Table 3. The estimators' frequencies are compared with both of the simulated and measured value in terms of absolute error (AE). The estimated operating frequencies well match with the results in the literature. The frequencies computed by the estimator remain less than absolute error of 0.08 for simulated results. Hence, the estimator simply calculates the operating frequency with MAE of 0.023 and 0.072 for simulated and measured values.

C. Validating the estimator

The notch antenna illustrated in Fig. 6 is printed on a 25x35 mm^2 FR4 PCB substrate of which dielectric permittivity, tangent loss and thickness are 4.4, 0.02 and 1.6 mm, respectively. The prototyped antenna of which parameters given in Table 4 is measured by the agency of Keysight Technologies N5224A PNA network analyzer. The measured $|S_{11}|$ parameter is shown in Fig. 7 in comparison with the simulated one.

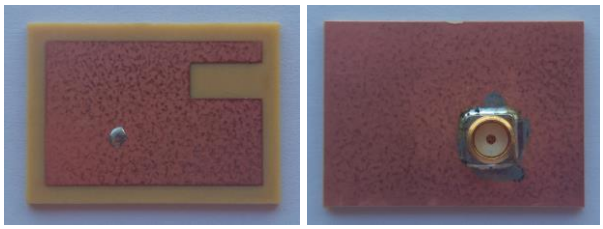

(a) (b)

Fig. 6. The photograph of prototyped notch antenna: (a) front view and (b) back view.

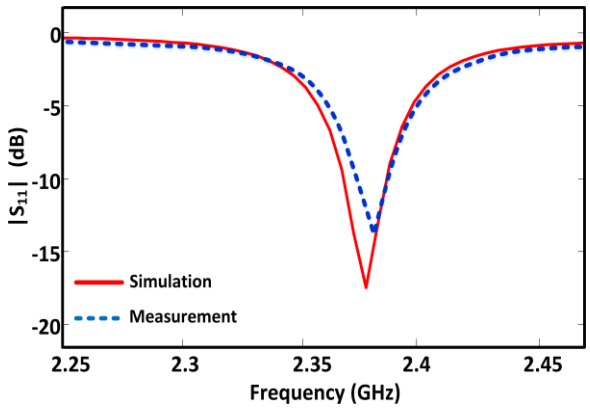

Fig. 7. S_{11} parameter of simulated and measured prototyped notch antenna.

Simulated 2D gain radiation patterns of the notch antenna at the operating frequency points of 2.38 GHz are illustrated in Fig. 8. The maximum gains are -4.12 dBi (in direction of 180° on *x*-*z* plane), -4.11 dBi (in direction of 355° on *y*-*z* plane) and -6.84 dBi (in direction of 165° on *x*-*y* plane).

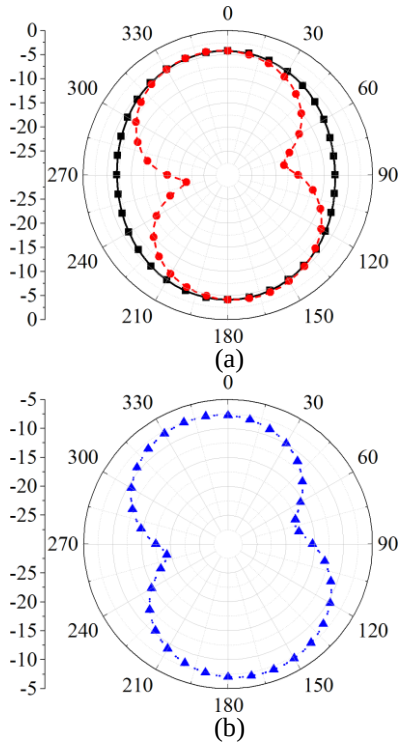

Fig. 8. Radiation patterns of the notch antenna at 2.38 GHz: (a) *x*-*z* plane (black solid line) and *y*-*z* plane (red dashed line), and (b) *x*-*y* plane (blue dot line).

Figure 9 indicates the peak gain plot versus frequency. The peak gain varies between -4.0 dBi and -8.0 dBi levels across 2.3 GHz to 2.5 GHz, whereas a maximum gain occurs 4.0 dBi at 2.38 GHz. It has minus gain in relative to an isotropic radiation, since the antenna radiates nearly omnidirectional pattern.

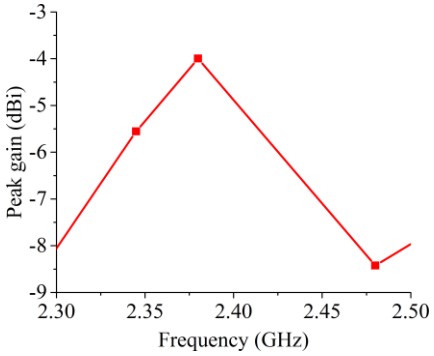

Fig. 9. Peak gain variation of the notch antenna.

From Tables 2-4, the estimator's operating frequencies are much close to the simulated/measured results. Therefore, the estimator can be successfully used to compute the operating frequency of the notch antennas without handling sophisticated mathematical functions and transformations. Moreover, the proposed estimator can be modified or improved to use similar tasks of nonlinear electromagnetic problems. The proposed estimator for notch antenna analysis is more versatile than methods suggested for C or U-shaped patch antennas, since the slot's position of the notch antenna varies rather than the mentioned antennas.

Table 2: The simulated notch antennas for testing the estimator

Antenna Parameter							Operating Frequency		Absolute Error (AE)
Patch Dimension (mm)					h (mm)	ε_r			
L	W	l	w	d			f_{sim}	f_{est}	
30	20	10	5	3	2.5	4.4	2.426	2.415	0.012
30	20	10	5	6	1.6	2.33	3.348	3.151	0.197
30	20	10	10	6	2.5	2.33	3.140	3.145	0.004
30	20	20	5	3	1.6	4.4	1.611	1.605	0.006
30	20	20	5	6	1.6	2.33	2.015	2.045	0.030
30	20	20	10	6	1.6	4.4	1.512	1.505	0.007
40	30	15	7.5	5	1.6	4.4	1.860	1.864	0.004
40	30	15	15	5	2.5	2.33	2.107	2.096	0.011
40	30	30	7.5	5	1.6	2.33	1.357	1.369	0.012
40	30	30	7.5	10	2.5	2.33	1.311	1.301	0.010
40	30	30	15	5	2.5	4.4	1.695	1.691	0.004
50	40	20	10	7	1.6	4.4	1.466	1.478	0.011
50	40	20	10	14	2.5	4.4	1.174	1.179	0.005
50	40	20	20	14	1.6	2.33	1.585	1.586	0.000
50	40	40	10	7	2.5	4.4	1.421	1.407	0.014
50	40	40	20	7	2.5	2.33	1.814	1.813	0.001
MAE									0.022

Table 3: Simulated and measured notch antennas in the literature for verifying the estimator

Ref. #	Antenna Parameter							Operating Frequency			Absolute Error (AE)	
	Patch Dimension (mm)					h (mm)	ε_r					
	L	W	l	w	d			f_{sim}	f_{mea}	f_{est}	AE_{sim}	AE_{mea}
[1]	40	60	5	5	27.50	1.5900	2.33	1.562	–	1.578	0.016	–
[1]	40	60	10	10	25.00	1.5900	2.33	1.445	–	1.419	0.026	–
[1]	40	60	15	15	22.50	1.5900	2.33	1.286	–	1.289	0.003	–
[1]	40	60	20	20	20.00	1.5900	2.33	1.130	–	1.176	0.046	–
[1]	40	60	25	25	17.50	1.5900	2.33	0.991	–	1.010	0.019	–
[1]	40	60	30	40	10.00	1.5900	2.33	0.899	–	0.900	0.001	–
[1]	40	60	30	5	27.50	1.5900	2.33	0.929	–	0.928	0.001	–
[1]	40	60	30	10	25.00	1.5900	2.33	0.887	–	0.935	0.048	–
[1]	40	60	30	2	29.00	1.5900	2.33	0.964	–	0.957	0.007	–
[3]	20	30	7	3	13.50	1.5700	2.33	2.810	2.822	2.813	0.003	0.009
[4]	20	30	5	20	5.00	1.5700	2.33	2.870	2.930	2.951	0.081	0.021
[11]	38	30	4	5	6.50	1.5875	2.4	2.987	2.957	3.066	0.079	0.109
[11]	38	30	6	5	6.50	1.5875	2.4	2.901	2.921	2.965	0.064	0.044
[11]	38	30	8	5	6.50	1.5875	2.4	2.777	2.477	2.778	0.000	0.301
[11]	38	30	10	5	6.50	1.5875	2.4	2.623	2.603	2.597	0.026	0.006
[11]	38	30	12	5	6.50	1.5875	2.4	2.416	2.316	2.422	0.006	0.106
[11]	38	30	14	5	6.50	1.5875	2.4	2.256	2.270	2.255	0.001	0.015
[11]	38	30	16	5	6.50	1.5875	2.4	2.101	2.200	2.099	0.002	0.101
[11]	38	30	18	5	6.50	1.5875	2.4	1.956	1.960	1.957	0.001	0.003
MAE											0.023	0.072

Table 4: Simulated and measured notch antenna prototyped in this study for validating the estimator

Antenna Parameter							Operating Frequency			Absolute Error (AE)	
Patch Dimension (mm)					h (mm)	ε_r					
L	W	l	w	d			f_{sim}	f_{mea}	f_{est}	AE_{sim}	AE_{mea}
30	20	10	5	3	1.6	4.4	2.380	2.390	2.407	0.027	0.017

V. CONCLUSION

In this article, an estimator using ANN built on MLP is implemented for computing the operating frequencies of the notch antennas. An ANN including three layers is modelled: input layer with 7 neurons, hidden layer with 4 neurons and output layer with 1 neuron. In order to constitute data for training and testing the estimator, number of 96 notch antennas having various physical and electrical parameters is simulated with the help of HyperLynx® 3D EM in terms of the operating frequency. The seven antenna parameters are also input to the ANN model to compute the operating frequency of the notch antenna. Number of 80 antennas are used for training and the remainders 16 antennas are utilized for testing the ANN model. In training, the ANN model is optimized by fitting the output of operating frequency to the simulated one. The proposed estimator is corroborated through three steps: testing with simulated antennas, verifying with literature and validating with prototyped antenna data. It is pointed out that the estimator computes operating frequency closely to real one. Once the estimator is properly trained, it can fast and accurately compute the operating frequency of patch antennas.

REFERENCES

[1] A. A. Deshmukh and G. Kumar, "Formulation of resonant frequency for compact rectangular microstrip antennas," *Microw. Opt. Techn. Let.*, vol. 49, pp. 498-501, 2007.

[2] A. Akdagli, M. B. Bicer, and S. Ermis, "A novel expression for resonant length obtained by using artificial bee colony algorithm in calculating resonant frequency of C-shaped compact microstrip antennas," *Turk J. Elec. Eng. & Comp. Sci.*, vol. 19, pp. 597-606, 2011.

[3] A. Toktas, M. B. Bicer, A. Akdagli, and A. Kayabasi, "Simple formulas for calculating resonant frequencies of C and H shaped compact microstrip antennas obtained by using artificial bee colony algorithm," *J. Electromagn. Waves. App.*, vol. 25, pp. 1718-1729, 2011.

[4] A. Akdagli, A. Kayabasi, and I Develi, "Computing resonant frequency of C-shaped compact microstrip antennas by using ANFIS," *Int. J. Elec.*, vol. 102, pp. 407-417, 2015.

[5] A. Toktas and A. Akdagli, "Computation of resonant frequency of E-shaped compact microstrip antennas," *J. Fac. Eng. Arch. Gazi Univ.*, vol. 27, pp. 847-854, 2012.

[6] A. Kayabasi and A. Akdagli, "Predicting the resonant frequency of E-shaped compact microstrip antennas by using ANFIS and SVM," *Wireless Pers. Commun.*, vol. 82 pp. 1893-1906, 2015.

[7] A. Akdagli and A. Toktas, "A novel expression in calculating resonant frequency of H-shaped compact microstrip antennas obtained by using artificial bee colony algorithm (ABC)," *J. Electromagn. Wave*, vol. 24, pp. 2049-2061, 2010.

[8] Z. N. Chen, "Radiation pattern of a probe fed L-shaped plate antenna," *Microw. Opt. Techn. Let.*, vol. 27, pp. 410-413, 2000.

[9] A. Kayabasi, A. Toktas, A. Akdagli, M. B. Bicer, and D. Ustun, "Applications of ANN and ANFIS to predict the resonant frequency of L-shaped compact microstrip antennas," *Appl. Comput. Electrom.*, vol. 29, pp. 460-469, 2014.

[10] A. Akdagli, A. Toktas, M. B. Bicer, A. Kayabasi, D. Ustun, and K. Kurt, "ANFIS model for determining resonant frequency of rectangular ring compact microstrip antennas," *Int. J. Appl. Electrom.*, vol. 46, pp. 483-490, 2014.

[11] S. Bhunia, "Effects of slot loading on microstrip patch antennas," *International Journal of Wired and Wireless Communications*, vol. 1, pp. 1-6, 2012.

[12] W. F. Richards, Y. T. Lo, and D. D. Harrisson, "An improved theory for microstrip antennas and applications," *IEEE T. Anten. Propag.*, vol. 29, pp. 38-46, 1981.

[13] K. Bhattacharyya and R. Garg, "A generalized transmission line model for microstrip patches," *IEE PROC-H.*, vol. 132, pp. 93-98, 1985.

[14] D. B. Davidson, *Computational Electromagnetics for RF and Microwave Engineering*. Cambridge University Press, Cambridge, United Kingdom, 2005.

[15] A. Taflove, *Computational Electrodynamics: The Finite-Difference Time Domain Method*. Artech House, Boston, 1995.

[16] R. F. Harrington, *Field Computation by Moment Methods*. IEEE Press, Piscataway, NJ, 1993.

[17] K. Guney and N. Sarikaya, "Adaptive neuro-fuzzy inference system for computing the resonant frequency of circular microstrip antennas," *The Applied Computational Electromagnetic Society*, vol. 19, pp. 188-197, 2004.

[18] F. Güneş, N. T. Tokan, and F. Gürgen, "A consensual modeling of the expert systems applied to microwave devices," *International Journal of*

RF and Microwave Computer-Aided Engineering, vol. 20, pp. 430-440, 2010.

[19] Y. Tighilt, F. Bouttout, and A. Khellaf, "Modeling and design of printed antennas using neural networks," *International Journal of RF and Microwave Computer-Aided Engineering*, vol. 21, pp. 228-233, 2011.

[20] A. R. Venmathi and L. Vanitha, "Support vector machine for bandwidth analysis of slotted microstrip antenna," *International Journal of Computer Science, Systems Engineering and Information Technology*, vol. 4, pp. 67-61, 2011.

[21] S. Haykin, *Neural Networks: A Comprehensive Foundation*. Macmillan College Publishing Company, New York, A.B.D, 1994.

[22] J. S. R. Jang, "ANFIS: Adaptive-network-based fuzzy inference system," *IEEE Transactions on Systems*, vol. 23, pp. 665-685, 1993.

[23] V. N. Vapnik, *Statistical Learning Theory*. Wiley, New York, 1998.

[24] I. Develi, "Application of multilayer perceptron networks to laser diode nonlinearity determination for radio-overfibre mobile communications," *Microwave and Optical Technology Letters*, vol. 42, pp. 425-427, 2004.

[25] HyperLynx® 3D EM, Version 15, Mentor Graphics Corporation, 8005 SW Boeckman Road, Wilsonville, OR 97070.

[26] M. T. Hagan and M.B Menhaj, "Training feed forward networks with the Marquardt algorithm," *IEEE Transactions on Neural Networks*, vol. 5, pp. 989-993, 1994.

[27] C. M. Bishop, *Neural Networks for Pattern Recognition*. Oxford University Press, London, 1995.

[28] M. Zandieh, A. Azadeh, B. Hadadi, and M. Saberi, "Application of neural networks for airline number of passenger estimation in time series state," *J. Appl. Sci.*, vol. 9, pp. 1001-1013, 2009.

Kadir Sabanci was born in 1978. He received his B.S. and M.S. degrees in Electrical and Electronics Engineering (EEE) from Selcuk University, Turkey, in 2001, 2005 respectively. In 2013, he received his Ph.D. degree in Agricultural Machineries from Selcuk University, Turkey. He has been working as Assistant Professor in the Department of EEE at Karamanoglu Mehmetbey University. His current research interests include image processing, data mining, artificial intelligent, embedded systems and precision agricultural technology.

Ahmet Kayabasi was born in 1980. He received his B.S. and M.S. degrees in EEE from Selcuk University, Turkey, in 2001, 2005 respectively. In 2015, he received his Ph.D. degree in Electrical and Electronics Engineering from Mersin University, Turkey. From 2001 to 2015, he was a Lecturer in the Electronics and Automation Department of Selcuk University. He has been working as Assistant Professor in the Department of Electrical and Electronics Engineering at Karamanoglu Mehmetbey University. His current research interests include antennas, microstrip antennas, computational electromagnetic, artificial intelligent.

Abdurrahim Toktas received B.S. degree in EEE at Gaziantep University, Turkey, in July 2002. He worked as Telecom Expert from Nov. 2003 to Dec. 2009 for Turk Telecom. He received M.S. and Ph.D. degrees in EEE at Mersin University, Turkey, in Jan. 2010 and July 2014, respectively. He worked in Department of Information Technologies at Mersin University from Dec. 2009 to Jan. 2015. Since Jan. 2015, he has been Assistant Professor with Department of EEE, Karamanoglu Mehmetbey University, Turkey. His current research interests include electromagnetics, antenna design, MIMO systems, UWB systems, computational electromagnetic, evolutionary optimization algorithms

Enes Yigit received his MSE and Ph.D. degrees in Electrical and Electronics Engineering from Mersin University, Turkey, in 2007, 2013 respectively. From 2004 to 2007, he was a Research Assistant in the Department of Electrical and Electronics Engineering and from 2007 to 2014, he was a Lecturer in the Vocational School of Technical Science at Mersin University, Mersin, Turkey respectively. He completed his Post-doc research at the University of Texas Arlington, TX, USA between 2014-2015. He is currently an Assistant Professor at the Department of Electrical-Electronics Engineering, Karaman, Turkey.

Bandwidth-Enhanced Compact Meander Printed Dipole Antenna

Chongyi Yue [1,2], Atef Elsherbeni [2], Veysel Demir [3], and Wenxing Li [1]

[1] Department of Information and Communication Engineering
Harbin Engineering University, Harbin, Heilongjiang 150001, China
yuechongyi@hrbeu.edu.cn, liwenxing@hrbeu.edu.cn

[2] College of Engineering and Computational Sciences
Colorado School of Mines, Golden, CO 80401, US
cyue@mines.edu, aelsherb@mines.edu

[3] Department of Electrical Engineering
Northern Illinois University, DeKalb, IL 60115, US
vdemir@niu.edu

Abstract ─ A miniaturization design of printed dipole antenna is proposed in this paper with enhanced operating bandwidth. As an example, three designs including a printed dipole, a meander dipole and a loop meander dipole, used in the wireless communication at 2.46 GHz are presented. The parameters regarding expanding bandwidth and reducing antenna size are discussed in details. These two antennas are modeled, simulated and optimized using HFSS and CEMS. Fabrication of the antennas are also performed. The simulation results and measurements show that the method proposed in this paper make the printed dipole more compact and bandwidth efficient.

Index Terms ─ Antenna miniaturization, meander antenna, wideband dipole antenna.

I. INTRODUCTION

With the expanding of the wireless terminals and hardware, the antenna miniaturization has been attracting more and more attention [1, 2]. Because the antennas are often integrated on a small circuit board and the space reserved for the antenna in the communication system such as the cell phones is usually smaller than one wavelength. The antenna elements printed on the substrate are generally a type of dipoles or monopoles and the design of electrically small antennas can be obtained by folding or meandering the antenna arm [3-5]. One of the main issues of reducing the antenna dimensions is the limitation of the bandwidth.

The expand of the bandwidth of printed dipoles is challenging. A previous study shows the 10 dB bandwidth of a dipole can be expanded from 2.9% to 4.8% at 2.43 GHz by folding the antenna [6], which is not very satisfactory.

In this paper, we focus on the better miniaturization and bandwidth extension of the printed dipole, thus three novel designs of printed dipole are proposed. With the intention to demonstrate the bandwidth enhancement, a printed dipole antenna (unfolded) operating at 2.46 GHz is first modeled and simulated. Then, in order to reduce the size of the antenna, a design of a meander antenna is introduced. This meander antenna has the same operating frequency as the printed dipole; however, this design reduces the size of the antenna arm by 30.6%. Another meander loop antenna is also designed afterwards. Although the size of the meander loop antenna is the same as the meander antenna mentioned above, the bandwidth of the meander loop antenna is increased by 43.5%.

The parameters in all the designs are discussed in details and the difference in the frequency performance due to the adjustment of the parameters are shown in the simulation. The software package Ansoft high-frequency structure simulator (HFSS) is used to numerically analysis all the designs. To verify the simulation results produced by HFSS, the home made software package CEMS [7], which is a 3D electromagnetic simulation tool based on the finite-difference time-domain method (FDTD), is employed to compute the return loss. The simulation results from these two simulation tools fit well. Fabrications and measurement of return loss of three antennas mentioned above are performed. The measurements and the simulation results have a good agreement.

II. PRINTED DIPOLE ANTENNA

In this part, a dipole antenna operating at 2.46 GHz is presented. The dipole is printed on both sides of a substrate with dimensions of 62 mm × 50 mm × 0.75 mm.

Submitted On: January 31, 2017
Accepted On: March 9, 2017

The front and back view of the printed dipole are shown in Fig. 1 (a) and Fig. 1 (b). The dielectric of the substrate has relative permittivity ε_r=2.2. The dipole arm is 1 mm wide and 24.5 mm long. The dipole arm on the front side is along negative z direction, while the arm on the back side is towards positive direction.

The HFSS with finite element method (FEM) kernel is employed for all the simulations in the research, and the FDTD software package CEMS (based on [7]) is used to verify the simulated results. One of advantages of using CEMS is that all the program can be running on the GPU, which has been proved to be quite efficient for the simulation process. In order to find more suitable designs for these three antennas, the optimetrics module in the HFSS is used to do the automate parametric sweeps, which allows us to get the appropriate parameters for each design more efficiently. The magnitude of S_{11} parameter from 2 GHz to 3 GHz is shown in Fig. 2. The printed dipole operates from 2.36 GHz to 2.57 GHz and the resonant frequency is centered at 2.46 GHz. The bandwidth of the antenna is 8.53%. It can be observed that the curves of the return loss produced by these two simulation tools match very well, which indicates that the simulation results are accurate and believable.

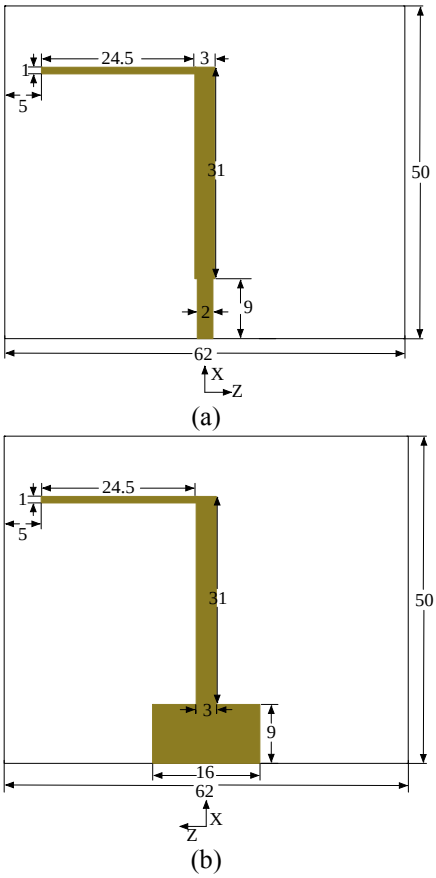

Fig. 1. Front view (a) and back view (b) of the printed dipole. The unit of all dimensions is mm.

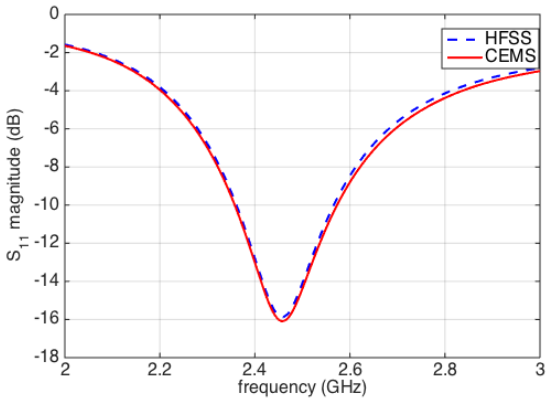

Fig. 2. The comparison of S_{11} parameter of the printed antenna from HFSS and CEMS.

The 2D gain patterns for θ and φ polarizations in *xy*, *xz*, and *yz* planes at 2.46 GHz are presented in Fig. 3. It is shown that the dipole is an omni-directional antenna and the maximum gain is 2.28 dB. In addition, the gain for φ polarization in these three planes are all below -15 dB, which implies that the printed dipole is mainly a linearly polarized antenna.

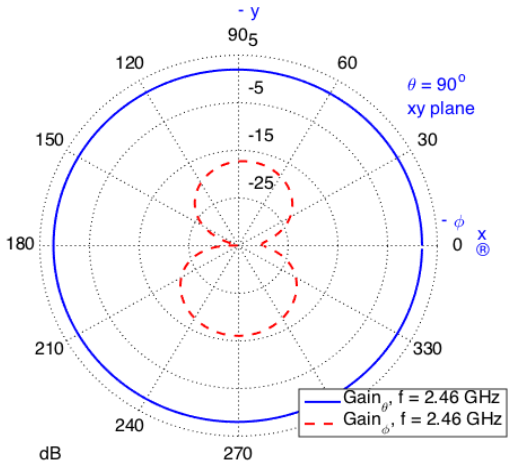

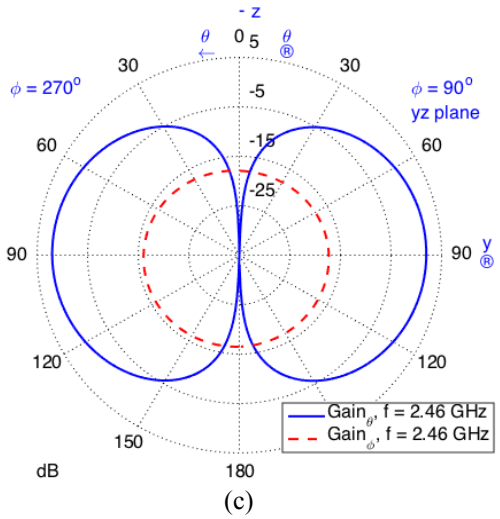

(c)

Fig. 3. The gain patterns of printed dipole for θ and φ polarizations at 2.46 GHz: *xy* plane, *xz* plane and *yz* plane are shown in (a), (b) and (c) respectively.

III. MEANDER ANTENNA

Although the printed dipole operates at 2.46 GHz, the size of the dipole arm should be reduced to get a better miniaturization. On the basis of the printed dipole, a meander antenna with a smaller size operating at 2.46 GHz is presented in this section.

The front and back view of the meander antenna are shown in Figs. 4 (a) and (b) respectively. The meander antenna is printed on a substrate with dimensions of 50 mm × 50 mm × 0.75 mm. The relative permittivity of the substrate is ε_r=2.2. Two design parameters, L denoting the width of the meandered strip and G denoting the width of the gaps, have the largest effect on the bandwidth and are chosen to be optimized for the antenna to work on the desired operating frequency.

Firstly, the cases of meander antenna with different widths of strip line are simulated. The width of the strip line increases from 0.5 mm to 1.5 mm with step of 0.25 mm. The return loss is shown in Fig. 5, from which we can see that as the width of the meandered strip increases, the bandwidth increases a little bit. Therefore, 1.5 mm is chosen as the width of the strip in order to obtain a larger bandwidth. Then, we conduct the simulations with different gap widths from 1.5 mm to 2 mm, which aims to keep the resonant frequency at 2.46 GHz. Finally, we choose 1.8 mm as the width of the gap. The return loss of the meander dipole with different gap widths are shown in Fig. 6. The length of the antenna arm with different L and G are shown in Table 1.

According to the simulation results above, the strips in the meander part are set to be 1.5 mm wide, and the gaps are set to be 1.8 mm wide. Each arm of the meander antenna is 18.4 mm long.

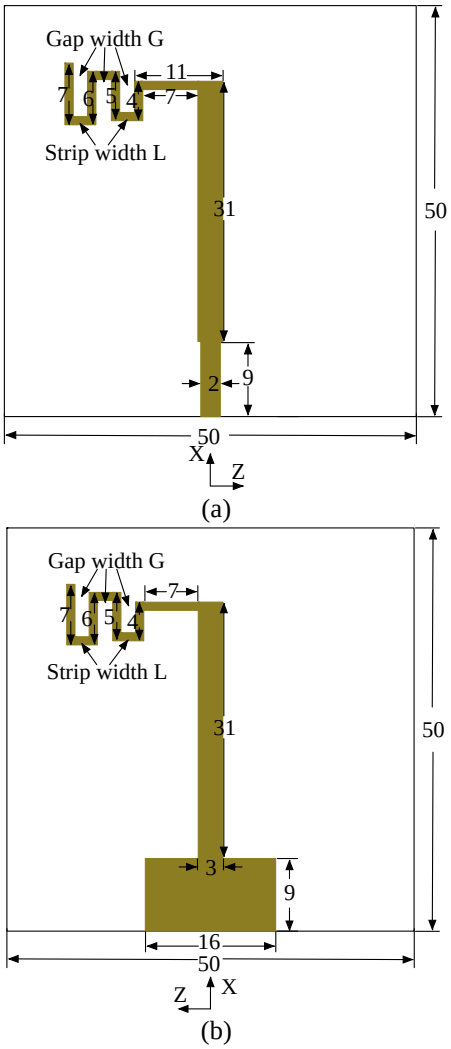

Fig. 4. Front view (a) and back view (b) of the meander antenna. The unit of all dimensions is mm.

Table 1: The length of the meander dipole arm with different strip width and gap width

Strip Width (L)	Gap Width (G)	Arm Length
0.5 mm	1.8 mm	14.4 mm
0.75 mm	1.8 mm	15.4 mm
1 mm	1.8 mm	16.4 mm
1.25 mm	1.8 mm	17.4 mm
1.5 mm	1.8 mm	18.4 mm
0.5 mm	2 mm	15 mm
0.75 mm	2 mm	16 mm
1 mm	2 mm	17 mm
1.25 mm	2 mm	18 mm
1.5 mm	2 mm	19 mm

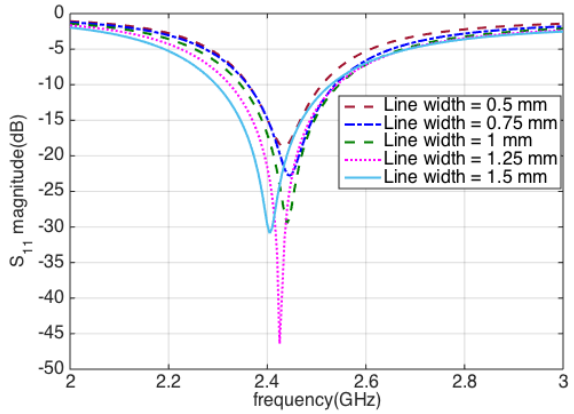

Fig. 5. Return loss of meander antenna with different widths of the strip.

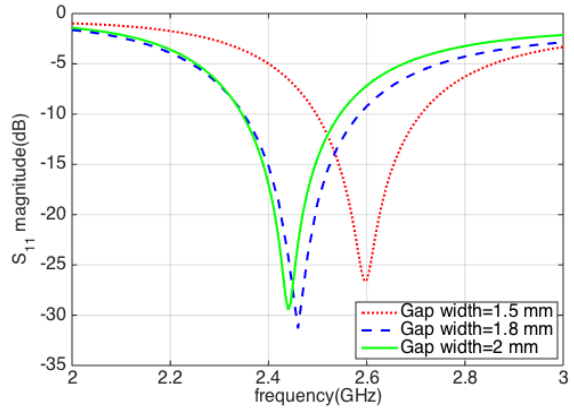

Fig. 6. Return loss of meander antenna with different widths of gap.

The design of the optimised meander antenna is also verified by CEMS. Return loss of meander antenna from HFSS and CEMS are shown in Fig. 7. The results from these two software match very well.

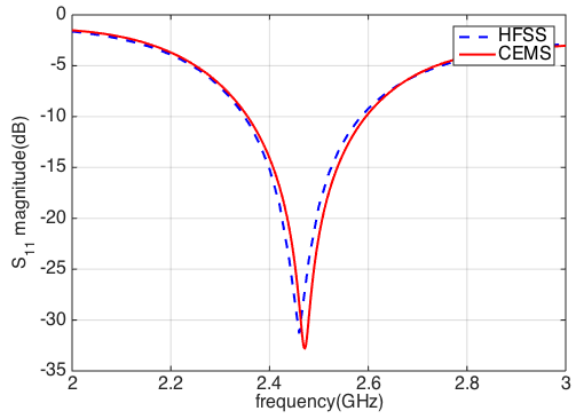

Fig. 7. The results of S_{11} parameter of optimized meander antenna from HFSS and CEMS.

As it is shown in Table 2, the operating frequency of printed dipole and meander antenna are the same. However, the design of this meander antenna allows a reduction of the antenna size. Compared to the arm length 24.5 mm of the printed dipole, the reduction of the size of the meander antenna arm is 24.89%.

Table 2: The frequency and size of printed dipole and meander antenna

Quantity	Dipole	Meander Antenna
f_{lower} /GHz	2.36	2.35
f_0 /GHz	2.46	2.46
f_{upper} /GHz	2.57	2.585
Bandwidth	8.53%	9.59%
Arm size /mm	24.5	18.4

The gain patterns for θ and φ polarizations are shown in Fig. 8. The maximum gain of the meander antenna is 2.2 dB, the same as that of the printed antenna. The gain of φ orientation on these three planes are all below -15 dB, which indicates the linear polarization of the meander antenna.

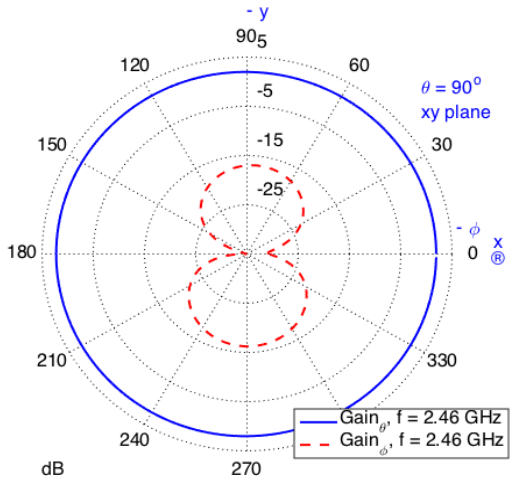

(a)

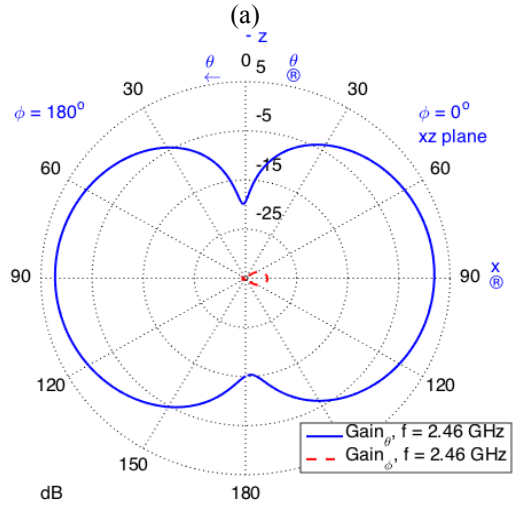

(b)

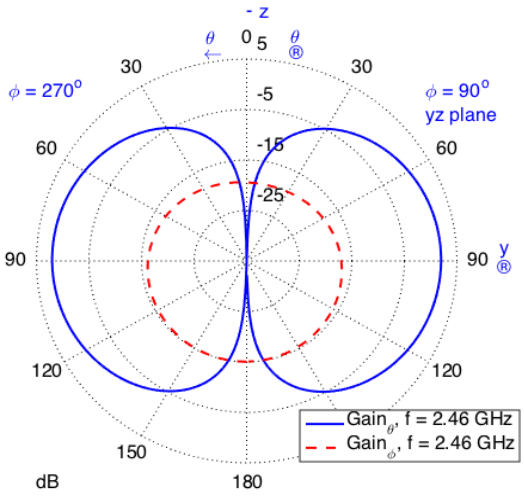

(c)

Fig. 8. The gain patterns of meander antenna for θ and φ polarizations at 2.46 GHz: *xy* plane, *xz* plane and *yz* plane are shown in (a), (b) and (c) respectively.

IV. MEANDER LOOP ANTENNA

Compared to the printed dipole, the design of the meander antenna reduces the size of the antenna. However, a better bandwidth of the antenna is desired. So in this part we aim to do an optimization to the meander antenna to obtain a wider frequency band without big change in antenna size.

After trying several configurations of the antenna, the geometry model of the meander loop antenna which has a larger bandwidth is finally obtained. In this design, the antenna arm is a meander loop consisting the upper meander part and the lower meander part, as shown in Fig. 9. The dimensions of the substrate are also 50 mm × 50 mm × 0.75 mm. The loop configuration is similar to the wideband design of anti-pedal bow-tie antennas operating in the C and X bands [8].

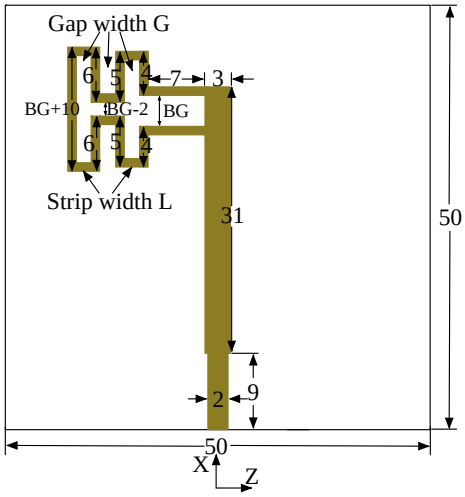

(a)

Fig. 9. Front view (a) and back view (b) of the meander loop antenna. The unit of all dimensions is mm.

The parameter BG denoting the distance between the upper and lower meander part is optimized first. Widths of gaps and strips of the meander loop antenna are 1.8 mm and 1.5 mm, respectively, which are the optimized values of the meander antenna mentioned in Section III. Different values of BG slightly affect the bandwidth of the meander loop antenna, and a better bandwidth is obtained when the value of BG is 2.75 mm. While the value of BG changes, the resonant frequency of the antenna almost keeps the same value at 2.6 GHz, as is shown in Fig. 10.

Since the desired resonant frequency of the antenna is 2.6 GHz, further work should be done in order to let the resonant frequency go back to 2.46 GHz. Therefore, models of the meander loop antenna with different gap widths (GL) are simulated in this part. The width of the gap is 1.8 mm in the optimization of BG, and we increased the width to 2.1 mm, 2.3 mm and 2.5 mm respectively in the new geometry models. The S_{11} parameter curves of different gap widths are shown in Fig. 11, in which we can see that as the gap width increases, the resonant frequency goes down. The resonant frequency is 2.46 GHz when the gap width is 2.3 mm. The length of the arm of the meander loop dipole is shown in Table 3.

In order to verify the simulation results from HFSS, the optimized meander loop antenna is also simulated by CEMS. The S_{11} curves of the optimized meander loop antenna from HFSS and CEMS are shown in Fig. 12. The results show that the curves have a good match, which indicates the accuracy of the simulation results of the meander loop antenna.

The meander loop antenna has the same resonant frequency as the dipole antenna and meander antenna. However, the meander loop antenna has a larger

bandwidth. The comparison of arm sizes, operating frequencies and bandwidths of these three antennas are shown in Table 2. f_{lower}, f_{upper} and f_0 represent the minimum, maximum and resonant frequency, respectively. From the results in the Table 4, we can see that the meander loop antenna has a 18.7% reduction in size and a 47.7% increase in bandwidth compared to the dipole antenna.

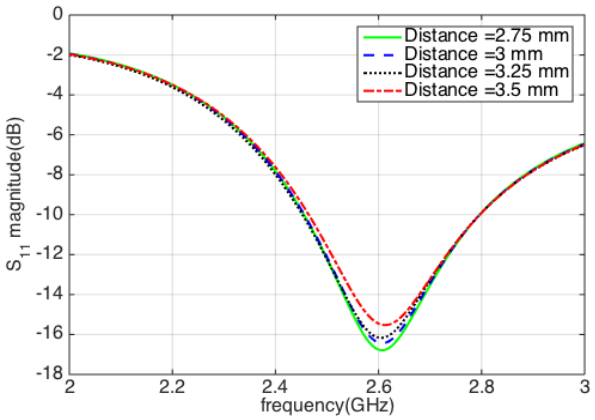

Fig. 10. S_{11} parameter curves of meander loop antenna with different distance between the upper meander part and the lower meander part.

Table 3: The length of the arm of the meander loop dipole with different gap width

Gap Width (GL)	Loop Distance (BG)	Arm Length
1.8 mm	2.75 mm	18.4 mm
2.1 mm	2.75 mm	19.3 mm
2.3 mm	2.75 mm	19.9 mm
2.5 mm	2.75 mm	20.5 mm

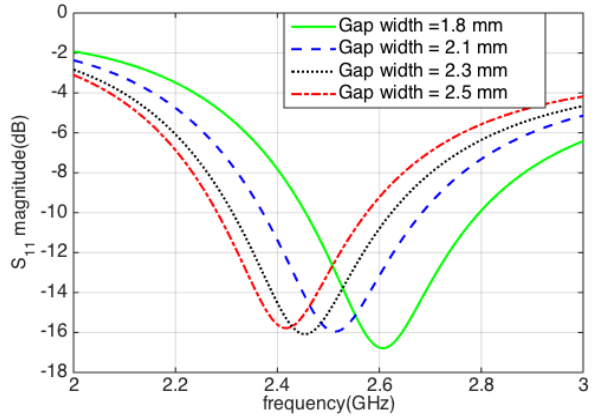

Fig. 11. The S_{11} curves of meander loop meander with different gap width.

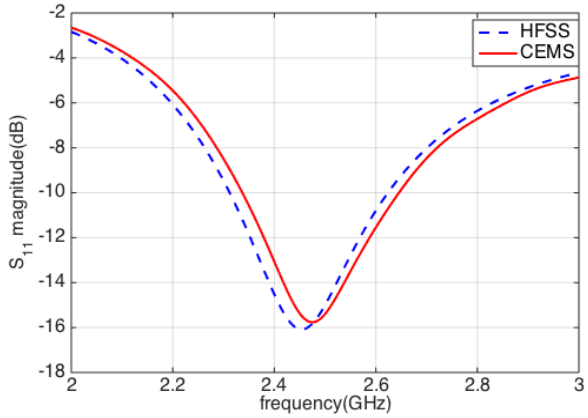

Fig. 12. The comparison of S_{11} curves of optimized meander loop antenna from HFSS and CEMS.

Table 4: The operating frequencies and arm size of these three antennas

Quantity	Dipole Antenna	Meander Antenna	Meander Loop Antenna
f_{lower} /GHz	2.36	2.35	2.315
f_0 /GHz	2.46	2.46	2.46
f_{upper} /GHz	2.57	2.585	2.625
Bandwidth	8.53%	9.59%	12.6%
Arm size /mm	24.5	18.4	19.9

The gain patterns for θ and φ polarizations of the meander loop antenna are shown in Fig. 13. It is shown from these patterns that the maximum gain of the meander loop antenna is 2.16 dB and the gain in φ polarization in these three planes are all below -15 dB, which indicates the meander loop antenna is also linearly polarized.

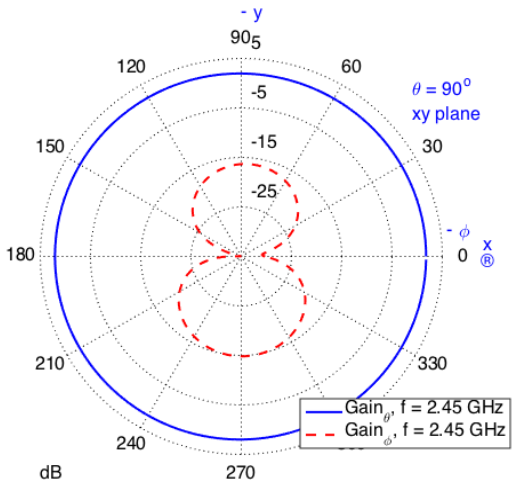

(a)

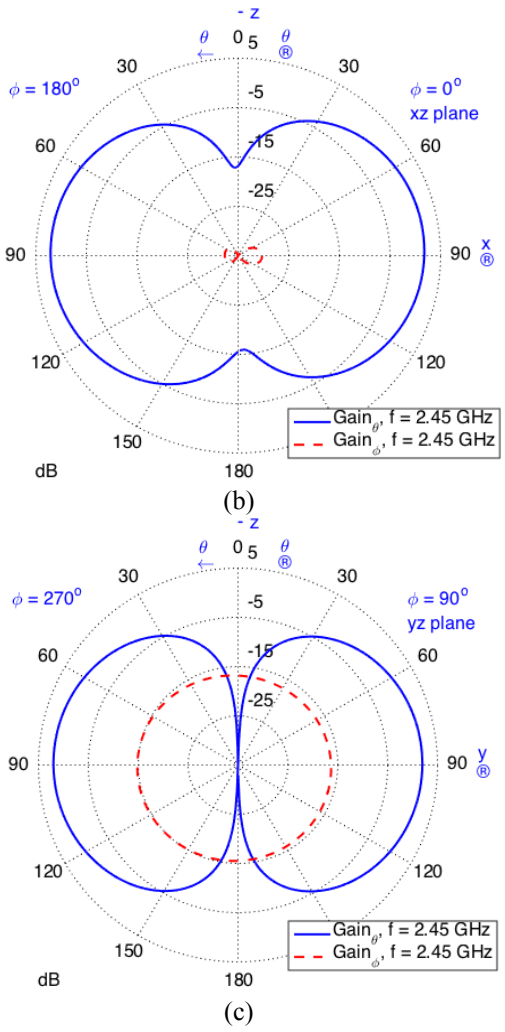

Fig. 13. The gain patterns of meander loop antenna for θ and φ polarizations at 2.45 GHz: *xy* plane, *xz* plane and *yz* plane are shown in (a), (b) and (c) respectively.

V. FABRICATION AND MEASUREMENT

The fabrication and measurement of the printed dipole, meander antenna, and meander loop antenna are presented in this part. The printed dipole is shown in Fig. 14 (a), the dimensions of the substrate is 62 mm × 50 mm. The meander antenna with L=1.5 mm and G=1.8 mm is shown in Fig. 14 (b). The loop meander dipole with L=1.5 mm, G=2.3 mm and BG=2.7 mm is shown in Fig. 14 (c). The dimensions of the substrate of meander dipole and meander loop dipole are 50 mm × 50 mm × 0.75 mm. The relative permittivity of the substrate of all the antennas is ε_r=2.2.

The measurements of the S_{11} parameter of these three antennas are shown in Fig. 15. The measurements of these three antennas in terms of the operating frequency and resonant frequency are shown in Table 5.

From Fig. 15, Table 4 and Table 5 we can see that the simulation results and measurements are in good agreement for the printed dipole and the meander antenna. Slight deviation is observed between simulated and measured results for the meander loop antenna, which could be attributed to unexpected tolerances in fabrication due to the more complicated structure of the its arm. Compared to the dipole antenna, the meander antenna and the meander loop antenna both have larger bandwidth, and the bandwidth of the meander loop antenna is the largest. Based on the measurement results, the bandwidth of the meander antenna and meander loop antenna increase by 21.1% and 54.5% respectively.

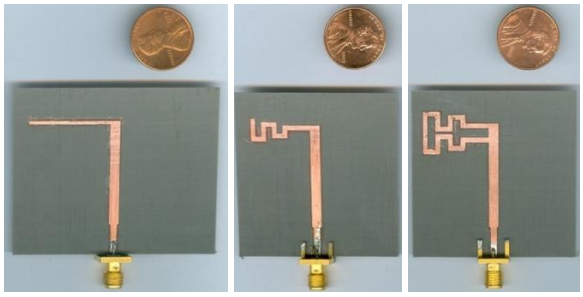

Fig. 14 The picture of printed dipole (a), meander antenna (b), and meander loop antenna (c).

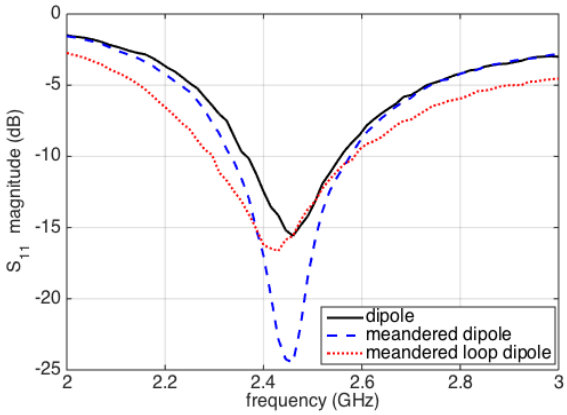

Fig. 15. The measurements of S_{11} parameter of three antennas.

Table 5: The operating frequencies of three antennas from measurements

Quantity	Dipole Antenna	Meander Antenna	Meander Loop Antenna
f_{lower}/GHz	2.36	2.34	2.30
f_0/GHz	2.46	2.46	2.43
f_{upper}/GHz	2.55	2.57	2.59
Bandwidth	7.72%	9.35%	11.93%

VI. CONCLUSION

The three antennas including a printed dipole, a meander antenna, and a meander loop antenna used in the wireless communication system with center frequency of 2.46 GHz are presented in this research. Based on the design of the first printed dipole, the miniaturization of the dipole is obtained by meandering the dipole arm and the bandwidth of the dipole is enhanced by the design of the meander loop. The choice of parameters for each design and the process of the optimization of these three antennas are presented in details one after another. The models of these antennas are simulated by HFSS and verified by CEMS and the simulation results fit well. These three antennas are fabricated and measured and the measurements of the return loss have a good match with the simulated results. From these results it is shown that, compared to the printed dipole, the meander antenna and meander loop antenna both have approximately 19% reduction in the size of the antenna. In addition, the 10 dB bandwidth of both designs increases. Especially the meander loop antenna has an approximately 50% increase in bandwidth compared to the traditional printed dipole.

REFERENCES

[1] C. Soras, M. Karaboikis, G. Tsachtsiris, and V. Makios, "Analysis and design of an inverted-F antenna printed on a PCMCIA card for the 2.4 GHz ISM band," *IEEE Antennas and Propagation Magazine*, vol. 44, no. 1, pp. 37-44, 2002.

[2] C. C. Lin, L. C. Kuo, and H. R. Chuang, "A horizontally polarized omnidirectional printed antenna for WLAN applications," *IEEE Transactions on Antennas and Propagation*, vol. 54, no. 11, pp. 3551-3556, 2006.

[3] H. Ma and H. Y. D. Yang, "Miniaturized integrated folded helical antennas," in *2011 IEEE International Symposium on Antennas and Propagation (APSURSI)*, pp. 753-756, 2011.

[4] C. M. Allen, A. Z. Elsherbeni, C. E. Smith, C. W. P. Huang, and K. F. Lee, "Tapered meander slot antenna for dual band personal wireless communication systems," *Microwave & Optical Technology Letters*, vol. 36, no. 5, pp. 381-385, 2003.

[5] J. Rashed and C. T. Tai, "A new class of resonant antennas," *IEEE Transactions on Antennas and Propagation*, vol. 39, no. 9, pp. 1428-1430, 1991.

[6] Y. Zhang and H. Y. D. Yang, "Bandwidth-enhanced electrically small printed folded dipoles," *IEEE Antennas and Wireless Propagation Letters*, vol. 9, pp. 236-239, 2010.

[7] A. Z. Elsherbeni and V. Demir, *The Finite-Difference Time-Domain Method For Electromagnetics with MATLAB Simulations*. 2nd edition, Edison, NJ: SciTech Publishing, an Imprint of the IET, 2016.

[8] A. A. Eldek, A. Z. Elsherbeni, and C. E. Smith, "Wide-band modified printed bow-tie antenna with single and dual polarization for C - and X-band applications," *IEEE Transactions on Antennas and Propagation*, vol. 53, no. 9, pp. 3067-3072, 2005.

Design of a High Gain Bandwidth Improved Aperture Antenna Using a Frequency Selective Surface

Mahdi Ghorbani and Habib Ghorbaninejad

Department of Electrical Engineering
University of Guilan, Rasht, Iran
ghorbani.me@gmail.com, ghorbaninejad@guilan.ac.ir

Abstract ─ In this paper a wideband, high-gain, and compact design of an aperture antenna has been proposed. In the proposed antenna a patch type frequency selective surface (FSS) as a superstrate has been placed in front of a rectangular aperture, mounted to a conducting ground plane. The proposed simple 3×3 patch type FSS has considerably enhanced the antenna performance, including the gain and the bandwidth concurrently. The proposed structure has been simulated to validate the obtained results. The maximum gain of 16.03 dB and 3-dB gain bandwidth of 19.7% (14.25–17.35 GHz) has been achieved.

Index Terms ─ Frequency Selective Surface (FSS), Partially Reflecting Surface (PRS), Resonant Cavity Antenna (RCA).

I. INTRODUCTION

Waveguide antennas are high efficiency, high polarization purity, and high power handling antennas with good return loss, but the gain of these antennas are low. By adding partially reflecting surface (PRS) in front of the feeding aperture and parallel to the ground plane at suitable distance, directivity and gain of this type of antennas are enhanced. Trentini in 1956 [1] for the first time has introduced these types of antenna and has been investigated later in [2-4] and many other literatures. In these structures, a resonating cavity consisting of conducting ground plane and partially reflecting surface (PRS) as superstrate has been formed to provide electromagnetic wave multi-reflected between these two planes. The electromagnetic wave is leaked to broadside from the superstrate and realized directive and high gain beam. The distance between these two planes should be such that the maximum number of these beams that are leaked from superstrate be in a same direction.

PRS can be made of simple unprinted high permittivity dielectric material [5], [6]. In unprinted dielectric PRSs as a superstrate, most important factor is permittivity. The higher permittivity, allow the higher gain and directivity but increase losses and fabrication cost. The printed PRS is more useful and it has more parameters for optimization. The PRSs may be array of simple square shape FSS [7] or special pattern over dielectric [8]. Also, using two or more layers of PRSs, enhance the gain and the directivity more efficiently, but 3-dB gain bandwidth is decreased. The resonant frequency of each PRS may be designed so that to enhance 3-dB gain bandwidth, but it increases fabrication cost and complexity [9], [10]. In [11], two layers of dielectrics and three layers of metal slabs are laminated to form a more compact size of PRS. The other way for using more compact and efficient structure is double side printed circuit board (PCB) [12], [13]. In [14], meta-material is used as a ground plane for more compact size of the antenna, but charts show weak input impedance and 3-dB gain bandwidth. In [15], horizontally polarized antenna for ultra wideband operation has been presented, so that the antenna maximum achievable gain has been increased, and also the bandwidth has been improved significantly. In [16], novel shape of FSS has been investigated. FSS can also be used for multiband applications [17].

Unprinted dielectrics have a simple structure but usually high cost, that in high frequencies have high power losses. Some techniques are used to enhance the maximum gain, but the antenna bandwidth is not desirable in the given frequency range. So, it is aimed to have an antenna which has advantages of improved 3-dB gain bandwidth and wide band impedance bandwidth in the same time.

In this paper, we investigate an antenna with easy structure that improved 3-dB gain bandwidth, maximum gain and the impedance bandwidth concurrently. A rectangular aperture mounted on a conducting ground plane has been used to feed antenna as primary radiating source. A FSS has been placed above the aperture at the distance of free space half wavelength at the design frequency. The FSS is composed of 3×3 square metal patches laminated on inside of FR4 dielectric slab. The proposed antenna has provided high gain, wide 3-dB gain bandwidth and wideband features in a compact design. Waveguide aperture antenna is widely used in millimeter wave and communication systems that

Submitted On: August 30, 2016
Accepted On: January 21, 2017

provide high gain specification. This kind of antenna can be fabricated to conform to the desired surface, so it is often used in aircraft applications.

II. ANALYSIS AND PHYSICAL INSIGHT

Figure 1 shows a resonant cavity antenna which is formed between FSS and the ground planes. The ray analysis can be used to describe the resonance frequency in terms of the cavity height. This way is approximate because it ignores edge effect, and it investigates the dominant mode of radiation between two planes. The ray is multi-reflected between these two planes and leaked out from superstrate.

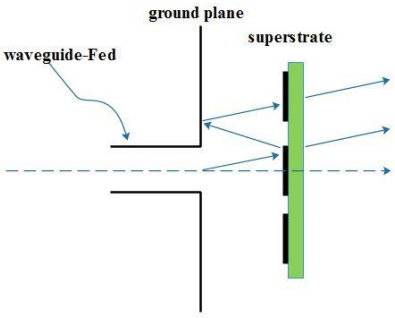

Fig. 1. Resonant cavity antenna formed between FSS and the ground plane.

The resonant height of the cavity or distance between superstrate and ground plane can be obtained as [18]:

$$s_d = \left(\frac{\psi_0}{2\pi} - 0.5\right)\frac{\lambda}{2} + n\frac{\lambda}{2}, \quad (1)$$

where s_d is the cavity height, ψ_0 is the angle of reflection coefficient of the FSS, λ is wavelength of designed frequency at free space, and n is an integer number. In this work for $\lambda = 19.35\,mm$ ($f_0 = 15.5\,GHz$), $\psi_0 = -43.8°$, n=2, s_d is equal to 13.3 mm that is in good agreement with s_d=11 mm, which is used in the simulation to compensate the capacitive loading effect of the FSS.

Also the gain and bandwidth of antenna can be obtained using the following formulas:

$$G = \frac{1+\rho}{1-\rho}, \quad (2)$$

$$BW = \left(\frac{\lambda}{2\pi s_d}\right)\frac{1-\rho}{\rho^{0.5}}, \quad (3)$$

where G is the relative maximum gain, BW is the bandwidth, and ρ is reflection coefficient magnitude.

An alternative procedure to obtain the design parameters of the proposed antenna can be performed using transmission line equivalent model. Figure 2 shows the transmission line equivalent model of the proposed antenna. The model is composed of two transmission line sections. To maximize the radiation field of the proposed antenna, the impedance seen just after FSS should be infinity. Moreover, FSS as superstrate can be modeled as a LC circuit. Hence, it is straight forward to optimize the structure in terms of unit cell dimensions and cavity height to achieve the goal of maximum radiation.

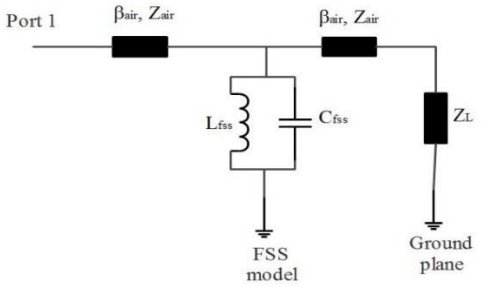

Fig. 2. Circuit model for the proposed antenna.

III. DESIGN AND SIMULATION

A. The proposed antenna configuration

The proposed antenna configuration has been shown in Fig. 3. The proposed antenna is composed of a rectangular aperture mounted on a conductive ground plane along with a FSS as superstrate. FSS in made of 3×3 arrays of square metal patches which is printed on inside surface of FR4 dielectric slab. Feeding waveguide is WR62 with dimensions of 7.9×15.8 mm. The FSS is symmetrically located in front of the aperture at the free space half-wavelength distance at the design frequency.

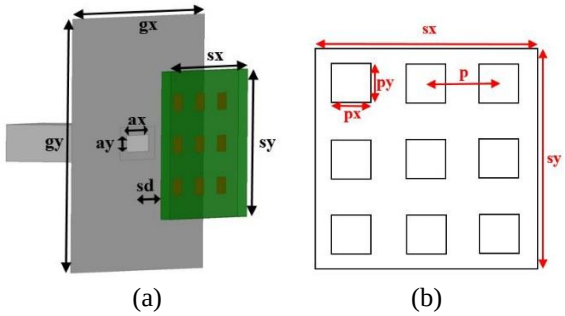

Fig. 3. The proposed antenna configuration: (a) three dimensional view, and (b) FSS structure.

Rectangular aperture (slot) with dimension of a_x and a_y in the center of conductive ground plane of dimensions $g_x \times g_y$, acts as primary radiating exciting source. Electric permittivity of FR4 dielectric is 4.41.

B. Design steps

Step 1: The design frequency of $f_0 = 15.5\,GHz$ is considered, corresponding to $\lambda_0 = 19.35\,mm$ free space wave length. So, the cavity height is about $\lambda_0/2$. Figure 4 shows the gain of the aperture antenna with unprinted dielectric slab for a set of cavity height. It can be concluded that the maximum gain occurs at approximately

$\lambda_0/2$, so that, with increasing the value of s_d, maximum gain occurs at lower frequencies. Moreover, 3-dB gain bandwidth and maximum gain is nearly the same for various parameters of s_d. According to the design consideration, s_d=11 mm ($0.57\lambda_0$) is selected for superstrate height.

Step 2: Figure 5 shows the reflection coefficient of the aperture antenna with and without slot. The antenna aperture size has negligible effect on the antenna gain specifications, but can improve the reflection coefficient. The proposed antenna without slot has a resonant at 16.5 GHz, but week bandwidth at frequencies less than 15.5 GHz. So, the aperture size of a_x=10 mm and a_y=4 mm is applied to the proposed antenna, where a WR62 waveguide aperture (15.8 mm×7.9 mm) at the center of a 60 mm×60 mm ($3.1\lambda_0 \times 3.1\lambda_0$) conductive ground plane is used as primary radiating source.

Step 3: Figures 6 (a), (b) and (c) show the gain, the reflection coefficient and E-plane radiation pattern of the proposed antenna for various values of patch size, in the frequency range. These figures show that increasing of patch dimensions improve maximum gain, but disturb the bandwidth, especially in lower frequencies. So, there should be a tradeoff between the antenna gain and its input impedance bandwidth. Hence, the values of p_x=p_y=4 mm ($0.21\lambda_0$) are the best choice to improve the maximum gain and the bandwidth. In this case, return loss is less than 10 dB and the gain is optimized. Also it shows that using metal patches printed dielectric slab instead of standalone dielectric increase maximum gain and 3 dB gain bandwidth.

Step 4: The other factor which has significant effect on the antenna features is the patch element distance, namely, p. Fig. 7 depicts the gain, the reflection coefficient and E-plane radiation pattern in accordance with p. Decreasing of p parameter is negligibly increased maximum gain and more effectively improve 3-dB gain bandwidth. But p parameter influence on bandwidth, and there is a tradeoff between both gain and bandwidth performance. So, in this design, p=10 mm ($0.52\lambda_0$) is considered as the best value.

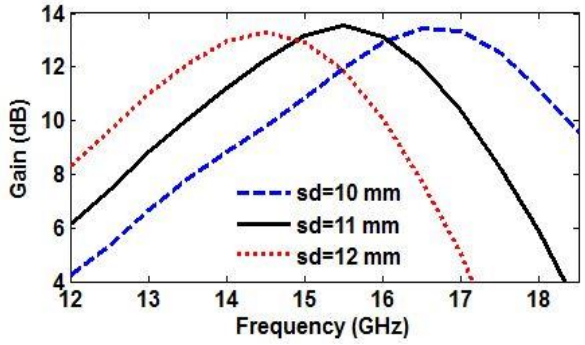

Fig. 4. Gain of the aperture antenna with unprinted dielectric for a set of cavity height.

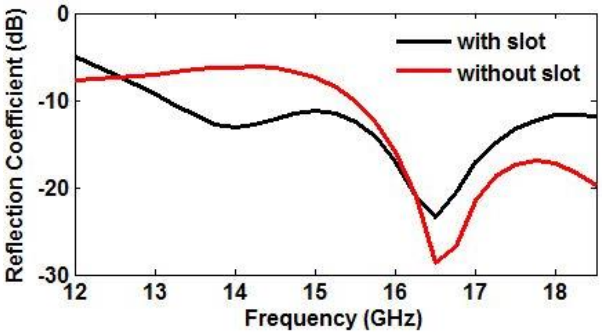

Fig. 5. Reflection coefficient of the aperture antenna with and without slot.

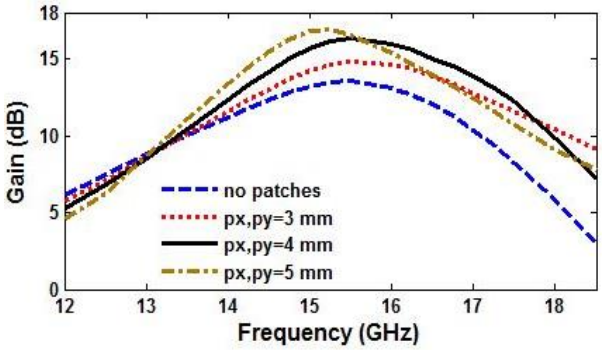

(a)

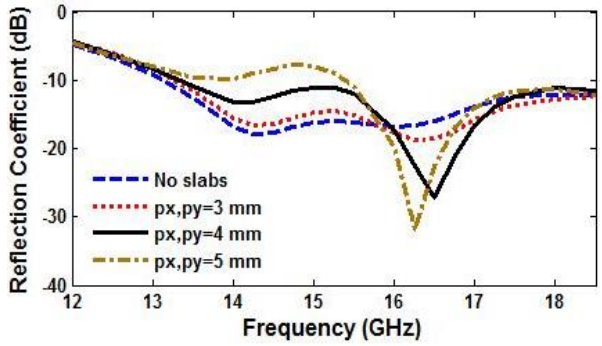

(b)

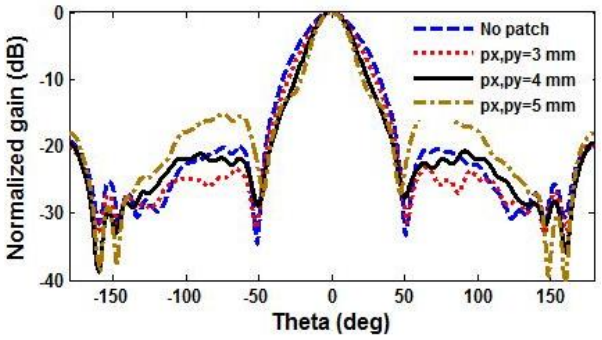

(c)

Fig. 6. (a) Gain, (b) reflection coefficient, and (c) E-plane radiation pattern of the proposed antenna with various metal patches size.

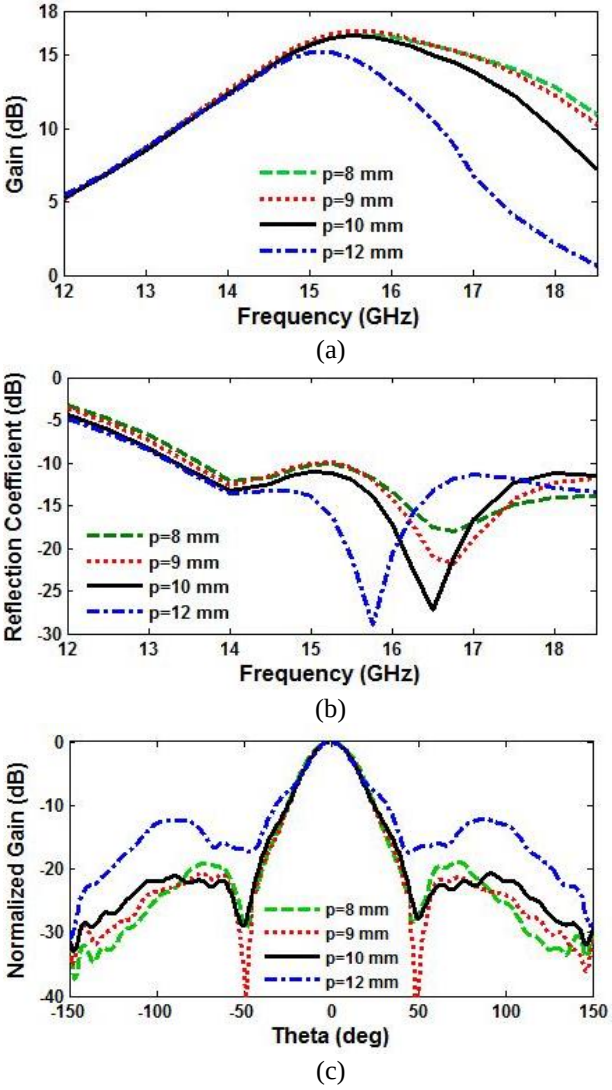

Fig. 7. (a) Gain, (b) reflection coefficient, and (c) E-plane radiation pattern of the proposed antenna with various metal patches distance.

When the patch size increases, stronger current on FSS as the main radiating surface, produce higher gain, but deteriorates input impedance matching. Our target is to increase the maximum gain until the reflection coefficient is less than 10 dB.

Step 5: Figures 8 (a), (b) and (c), show the gain, reflection coefficient and the E-plane radiation plane of the proposed antenna in terms of superstrate size, respectively. It is obvious that significant variations in the antenna performance are noticed. It can be deduced that increasing superstrate size up to 35 mm improves the maximum gain and 3-dB gain bandwidth, and then decreases beyond 35 mm. The bandwidth is also improved with increasing of the superstrate size up to 35 mm and then stands approximately constant for more than 35 mm. Therefore, the superstrate size of 35 mm ($1.81\lambda_0$) has the best maximum gain, however in all of the cases it's approximately constant. Also for s_x=s_y=35 mm, the bandwidth of the proposed antenna has a better performance compared to other values. Then it is considered as an optimum value in the design process.

Step 6: Similar parametric study lead to g_x=60 mm ($3.10\lambda_0$) as the optimum value for size of ground plane.

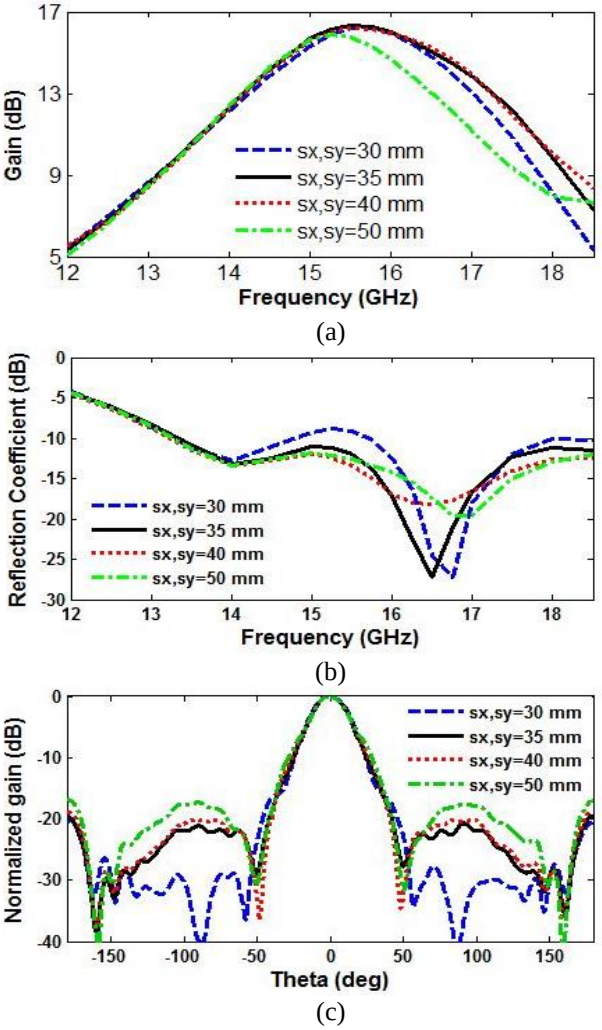

Fig. 8. (a) Gain, (b) reflection coefficient, and (c) E-plane radiation pattern of the proposed antenna with various superstrate sizes.

C. Simulation results and comparison

After determining the optimum design values, the proposed antenna is simulated using HFSS. The proposed antenna has a maximum gain of 16.03 dB at 15.5 GHz, 29.9% (13.42-18.13 GHz), high gain bandwidth (bandwidth with gain more than 10 dB), and 19.7% (14.25-17.35 GHz) of 3-dB gain bandwidth, with good bandwidth in the frequency range (absolute value of return loss greater than 10 dB). Furthermore, this structure uses single layer of FR4 dielectric with one side

printed FSS as a superstrate, so it is realized cheaper and fabricated easier compared to similar ones.

In Table 1, recent related works have been compared. The proposed antenna has improved the antenna performance in terms of (i) maximum gain, (ii) 3-dB gain bandwidth, (iii) high gain bandwidth and, (iv) impedance bandwidth, maintaining low cost and easy fabrication process. These features, occurring simultaneously, are not available in the presented ones in Table 1.

Table 1: A comparison study between the proposed antenna and earlier major available works

Reference	Max Gain (dB)	3-dB Gain Bandwidth (%)	High Gain Bandwidth (%)
[5]	16	18.75 Exactly: 12.5	Exactly: 19
[6]	16.95	16.25	Exactly: 29
[7]	20.07	Exactly: 2.5	Exactly: 5.5
[8]	12.1	17.2% bandwidth	Exactly: 12
[9]	20	15 Exactly: 9	-
[10]	19.0	16	Exactly: 22
[11]	9.0	Bandwidth: 65	-
[12]	12.2	12.3	Exactly: 10
[13]	18.4 16.2	6.4 12.6	Exactly: 18.5 Exactly: 23
[14]	19.2	1.8 Exactly: 1.0	5.5 Exactly: 3.5
[15]	9.0	Exactly: 100	-
[16]	13.93	-	-
[17]	11.1	Multiband application	
The proposed antenna	16.03	19.7	29.9

Figures 9 (a), (b) shows the radiation pattern of E- and H-plane of the proposed antenna at frequency design of 15.5 GHz. Side lobe and back lobe levels are 22.6 dB and 20.2 dB, respectively. Figures 10 (a), (b) show the gain and the reflection coefficient of the proposed antenna compared with main WR62.

Finally, the optimization has been done for 7×7 and 9×9 arrays of patches. Figures 11 (a), (b) show the gain and the reflection coefficient for the case.

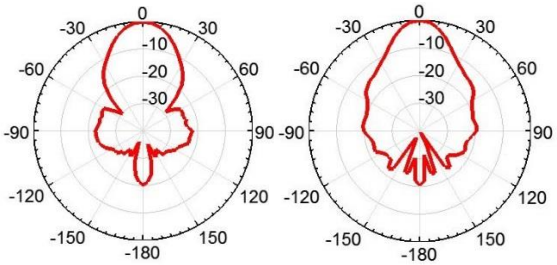

(a) (b)

Fig. 10. (a) E-plane and (b) H-plane radiation pattern of the proposed antenna at 15.5 GHz.

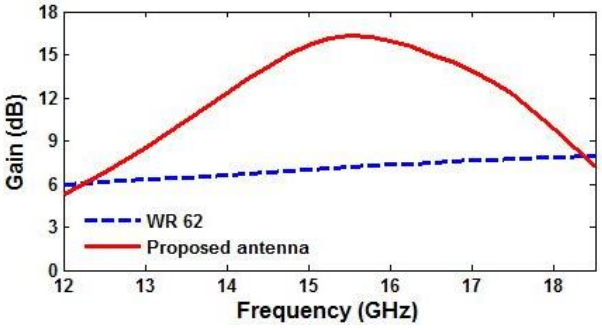

(a)

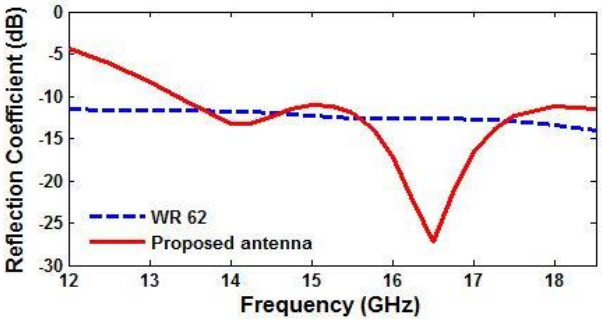

(b)

Fig. 10. (a) Gain and (b) reflection coefficient of the proposed antenna compared to WR62.

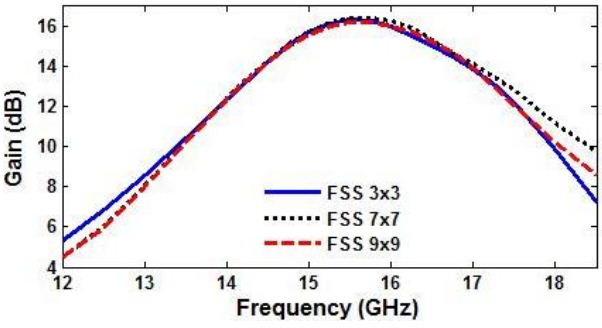

(a)

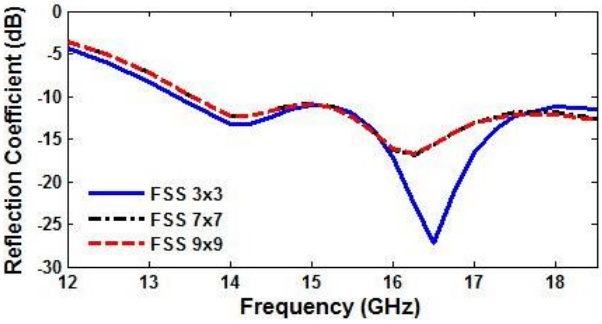

(b)

Fig. 11. (a) Gain and (b) reflection coefficient of the proposed antenna for 3×3, 7×7 and 9×9 arrays of patches.

The results confirm that the number of patches has negligible effect on the antenna performance.

IV. FULL METAL STRUCTURE

In the proposed antenna, printed FR4 dielectric is used for easy and cheap fabrication. This structure also can be considered without dielectric material. In this case superstrate is composed of 3×3 arrays of metal patches, which it is placed above the aperture using foam. In this case, the design parameters are obtained as a_x=11 mm ($0.57\lambda_0$), a_y=6 mm ($0.31\lambda_0$), p_x=p_y=7.5 mm ($0.39\lambda_0$), p=12 mm ($0.62\lambda_0$), s_d=12 mm ($0.62\lambda_0$), g_x=g_y=50 mm ($2.58\lambda_0$). Table 2 shows the design parameters of full metal antenna compared with the FSS with standalone dielectric. It shows that the same result can be obtained with full metal structure.

Table 2: A comparison study between the proposed antenna and its full metal structure counterpart

Antenna Characteristic	FSS with Dielectric	FSS without Dielectric
Max gain (dB)	16.03	16.20
Bandwidth (GHz)	13.14 and above	12.68 and above
3-dB gain bandwidth	3.10 GHz (19.7%)	2.52 GHz (17.0%)
High gain bandwidth	4.71 GHz (29.9%)	4.38 GHz (28.5%)
Side lobe level (dB)	22.6	17.1
Back lobe level(dB)	20.2	19.8

V. CONCLUSION

In this paper, a waveguide fed aperture antenna with a FSS as superstrate is proposed. The proposed antenna is composed of aperture mounted on an extended conducting ground plane, together with a FSS as a superstrate, which is located over the aperture. FSS is composed of common and cheap FR4 with 1.6 mm thickness, which 3×3 array of metal patches that is printed on inside surface of dielectric slab. The proposed antenna has a maximum gain of 16.03 dB at 15.5 GHz, and 29.9% (13.42-18.13 GHz) high gain bandwidth, and 19.7% (14.25-17.35 GHz) of 3-dB gain bandwidth. Moreover, full metal structure with a FSS composed of 3×3 array of metal patches is investigated and the same result has been obtained. The full metal structure antenna have a maximum gain of 16.20 dB at 15.5 GHz, and 28.5% (13.64-18.17 GHz) high gain bandwidth, and 17.0% (14.44-17.12 GHz) of 3 dB gain bandwidth. The proposed antennas have been simulated using HFSS to verify the results.

REFERENCES

[1] G. V. Trentini, "Partially reflecting sheet array," *IRE Trans. Antennas Propagat.*, vol. 4, pp. 666-671, 1956.

[2] Y. Sugio, T. Makimoto, S. Nishimura, and H. Nakanishi, "Analysis for gain enhancement of multiple-reflection line antenna with dielectric plates," *Trans. IEEE*, pp. 80-112, Jan. 1981.

[3] N. G. Alexopoulos and D. R. Jackson, "Fundamental superstrate (cover) effects on printed circuit antennas," *IEEE Trans. Antennas Propagat.*, vol. AP-32, pp. 807-816, Aug. 1984.

[4] D. R. Jackson and N. G. Alexopoulos, "Gain enhancement method for printed-circuit antennas," *IEEE Transactions on Antennas and Propagation*, vol. 33, no. 9, pp. 976-987, 1985.

[5] M. A. Al-Tarifi, D. E. Anagnostou, A. K. Amert, and K. W. Whites, "The puck antenna: A compact design with wideband, high-gain operation," *IEEE Transactions on Antennas and Propagation*, vol. 63, no. 4, pp. 1868-1873, 2015.

[6] B. A. Zeb, R. M. Hashmi, and K. P. Esselle, "Wideband gain enhancement of slot antenna using one unprinted dielectric superstrate," *Electronics Letters*, vol. 51, no. 15, pp. 1146-1148, July 2015.

[7] A. Foroozesh and L. Shafai, "Investigation into the effects of the patch-type FSS superstrate on the high-gain cavity resonance antenna design," *IEEE Transactions on Antennas and Propagation*, vol. 58, no. 2, pp. 258-270, Feb. 2010.

[8] H. Zhu, Y. Yu, X. Li, and B. Ai, "A wideband and high gain dual-polarized antenna design by a frequency-selective surface for WLAN application," *Progress In Electromagnetics Research C*, vol. 54, pp. 57-66, 2014.

[9] K. Konstantinidis, A. P. Feresidis, and P. S. Hall, "Multilayer partially reflective surfaces for broadband Fabry-Perot cavity antennas," IEEE Transactions on Antennas and Propagation, vol. 62, no. 7, July 2014.

[10] K. Konstantinidis, A. P. Feresidis, and P. S. Hall, "Dual-slot feeding technique for broadband Fabry–Perot cavity antennas," *IET Microwaves, Antennas & Propagation*, vol. 9, no. 9, pp. 861-866, 2015.

[11] A. Chatterjee and S. K. Parui, "Gain enhancement of a wide slot antenna using a second-order bandpass frequency selective surface," *Radio-engineering*, vol. 24, no. 2, June 2015.

[12] Y. F. Lu and Y. C. Lin, "Design and implementation of broadband partially reflective surface antenna," *International Symposium on Antennas and Propagation (APSURSI)*, pp. 2250-2253, 2011.

[13] Y. Ge, K. P. Esselle, and T. S. Bird, "The use of simple thin partially reflective surfaces with positive reflection phase gradients to design wideband, low-profile EBG resonator antennas," *IEEE Transactions on Antennas and Propagation*, vol. 60, no. 2, pp. 743-750, Feb. 2012.

[14] S. Wang, A. P. Feresidis, G. Goussetis, and J. C. Vardaxoglou, "High-gain subwavelength resonant cavity antennas based on metamaterial ground planes," *IEE Proceedings - Microwaves, Antennas and Propagation*, vol. 153, no. 1, pp. 1-6, 2006.

[15] R. V. S. Ram Krishna and R. Kumar, "Slotted ground microstrip antenna with FSS reflector for high-gain horizontal polarisation," *Electronics Letters*, vol. 51, no. 8, pp. 599-600, 2015.

[16] J. J. Tang, X. L. Wu, J. Li, and X. Y. Li, "A high gain microstrip antenna integrated with the novel FSS," *2015 4th International Conference on Computer Science and Network Technology (ICCSNT 2015)*, 2015.

[17] N. Wongsin, "High gain multiband circular loop antenna with ring resonators reflectors by using FSS technique," *The 2015 International Workshop on Antenna Technology*, pp. 338-341, 2015.

[18] M. A. Al-Tarifi, D. E. Anagnostou, A. K. Amert, and K. W. Whites, "Bandwidth enhancement of the cavity resonance antenna (CRA) using multiple dielectric superstrate layers," presented at the *2011 IEEE MTT-S Int. Microwave Symp*., Baltimore, MD, June 5-10, 2011.

M. Ghorbani received B.Sc. degree in Electrical Engineering from Isfahan University of Technology (IUT), Isfahan, Iran in 2003. He worked 10 years in the industry as a Design and R&D Manager. He received M.Sc. degree in 2016 in Fields and Wave Communication Engineering from University of Guilan.

H. Ghorbaninejad received B.Sc. degree from University of Guilan in 2003 and M.Sc. and Ph.D. degrees from Iran University of Science and Technology (IUST) in 2005 and 2010 respectively, all in Fields and Wave Communication Engineering.

He is currently Assistant Professor at Department of Electrical Engineering of University of Guilan. His scientific fields of interest are electromagnetic problems including microwave filter design, compact microwave devices and Green's function of microwave structures.

Microstrip Patch Sensors for Complex Permittivity Measurement of Medium Loss Liquids Using 3D-FDTD

G. Moradi and M. Mosalanejad

Department of Electrical Engineering, Microwave Measurement Research Lab
Amirkabir University of Technology, Tehran, 15914, Iran
ghmoradi@aut.ac.ir, mosalanejad@aut.ac.ir

Abstract ─ Two novel microstrip resonators are designed to measure the complex permittivity of medium loss liquids. These resonators have two layers, the first one is the sample layer and the second one is the base layer that the patch is printed on it. The base layer is suspended or inverted on the sample layer and the S-parameter is measured. The complex permittivity of the sample layer is extracted from the resonance frequency and the 3-dB bandwidth of the S-parameter. In this paper, binary mixtures of ethanol and methanol are used as sample layer. FDTD is a well-known computational method and is used for analyzing the structures. The experimental results for both of these resonators are really good and agree with reference values.

Index Terms ─ Microstrip patch resonator, microwave chemistry, permittivity measurement, 3D-FDTD.

I. INTRODUCTION

Complex permittivity measurement has high importance in microwave engineering. Since the permittivity of the materials changes a lot with frequency at high frequencies, so it is important to measure it with high accuracy in microwave frequencies. Determination of dielectric properties of materials is also important for the process control and quality control. The progress made in this direction has been covered in three books [1-3]. Over years, a number of techniques have been reported to measure the dielectric properties of materials at microwave frequency. These methods have used several media, like free-space, coaxial line, metal waveguide, dielectric waveguide, strip line, etc. The classical methods are summarized in the twin books of Hippel [4, 5]. The sensors based on waveguide and coaxial lines are bulky and not convenient for integration with electronic circuits [8-10]. Also, the volume of liquid that is needed for test in these approaches are much more than the volume of liquid which is needed for other methods like the one that is proposed in this paper. On the other hand, planar circuits, such as microstrip lines, coplanar waveguides, and strip lines have lots of advantages like low cost, easy to implementation, portability, online network monitoring and also not being destructive, so they have found their applications in complex permittivity measurements in recent years [11]. Several investigators have used microstrip patch resonators for the determination of the dielectric constant of a substrate [12-15]. Also, some of them have used microstrip patch resonators for complex permittivity measurement of liquids [16, 17]. Since it is hard to form liquids in a particular shape, so all kinds of methods of measuring permittivity are not applicable to measure their permittivities, but some methods are interesting and easy to implement. For example in [17], authors have suggested a two layer microstrip patch for investigation of complex permittivity of materials in sheet, liquid and paste forms. In this case, they have proposed some formulas for computation of total Q-factor and resonance frequency for this microstrip patch at first and then, they have explained the process of extracting the complex permittivity of low loss materials using these two parameters, total Q-factor and resonance frequency. As can be seen, the structures which have been used in this paper are very similar to those used in [17], however the adopted methods are completely different. In [17], the complex permittivity has been extracted by using some formulas, but in this paper, full-wave analysis is used to compute the complex permittivity. The planar circuit methods for measuring complex permittivity of liquids can be classified into two groups, resonant and non-resonant methods. Resonant methods are used because of their accuracy and sensitivity and non-resonant methods are used because of their broadband applications [18]. There are a lot of liquids which have medium or high permittivity and are very important in microwave chemistry, so a method is needed to measure their permittivity.

One of the most important methods of estimating the permittivity of materials including liquids in a wide range of frequency is using of formulas which need some initial parameters. One of these formulas comes from Debye theory that was introduced for the first time by Robert in 1988. According to Debye theory, the complex permittivity of a dielectric can be expressed as follows

Submitted On: September 20, 2016
Accepted On: February 28, 2017

[1, 19]:

$$\varepsilon_r = \varepsilon_{r\infty} + \frac{\varepsilon_{r0} - \varepsilon_{r\infty}}{1 + j\beta}, \quad (1)$$

$$\varepsilon_{r\infty} = \lim_{\omega\to\infty} \varepsilon_r, \quad (2)$$

$$\varepsilon_{r0} = \lim_{\omega\to 0} \varepsilon_r, \quad (3)$$

$$\beta = \frac{\varepsilon_{r0} + 2}{\varepsilon_{r\infty} + 2}\omega\tau, \quad (4)$$

where τ is the relaxation time and ω is the operating angular frequency. Equation (1) indicates that the dielectric permittivity due to Debye relaxation is mainly determined by three parameters, ε_{r0}, $\varepsilon_{r\infty}$ and τ. As can be seen, such formulas like Debye function are really useful, since the permittivity of materials can be calculated for a wide range of frequency, but the problem is that using of such formulas needs to determine some parameters like determining ε_{r0}, $\varepsilon_{r\infty}$ and τ in Debye formula. In [19], the complex permittivity of binary mixtures of ethanol–methanol in the range from 200 MHz to 26.5 GHz have been measured and parameters including ε_{r0}, $\varepsilon_{r\infty}$ and τ have been extracted for these binary mixture for using in Debye formula.

In this paper, 2 resonators are introduced to find the complex permittivity of the medium loss liquids, i.e., suspended and inverted patch resonators. Using the scattering responses of these structures, permittivity of medium loss liquids is extracted.

II. MICROSTRIP PATCH RESONATORS AS SENSORS

Figure 1 shows the simple schematic of the resonators used in our study. They have two layers, the first layer is the liquid under test and the second layer is the substrate that the patch is printed on it. The first layer is called the sample layer and the second layer is called the base substrate. The thickness, dielectric constant, and loss tangent for the base layer are known but for the sample dielectric are unknown. Taconic RF-35 with relative permittivity of 3.5 is used as substrate for the base layer. The sample thickness (h_{sam}) is 2 mm and the base thickness (h_{base}) is 1.524 mm. The dimensions of the patch for both of these patch resonators are the same and is 35 mm×25 mm. The ground is the empty metallic cavity that should be filled with the liquid under test. The ground of the cavity should be large enough not to infect the parameters of our structure, so its dimension is 10 cm×10 cm. The feed of the microstrip resonator is connected to a SMA adapter and the SMA connector should be kept away from the liquid solutions. The cavity is filled with the sample and the base layer is put on it, then the S_{11}-parameter of the resonator is measured. The resonance frequency and 3-dB bandwidth of the structures are calculated from measured data. When the sample is changed, the resonance frequency and the 3-dB bandwidth changes too, so the resonance frequency shift and the 3-dB bandwidth variation reflect the complex permittivity of the liquid under test.

As can be seen in Fig. 1, for one of these resonators, the base layer is suspended on the patch and for the other one the base layer is inverted on the patch. Suspended patch resonator is used to measure the complex permittivity of medium loss liquids for the frequency about 2.3 GHz and inverted patch resonator is used to measure the complex permittivity of medium loss liquids for the frequency about 480 MHz. Ethanol and methanol are two types of liquids which have medium loss. Therefore, binary mixtures of ethanol and methanol with different volume fractions are used as material under test for the sample layer. In [19], complex permittivity of these two types of liquids is measured and the parameters which are needed in Debye function are specified for different volume fractions of their binary mixtures in the room temperature. It is worth to say that the data which have been reported in [19] is used as reference for this paper and the results of this paper have been compared with them.

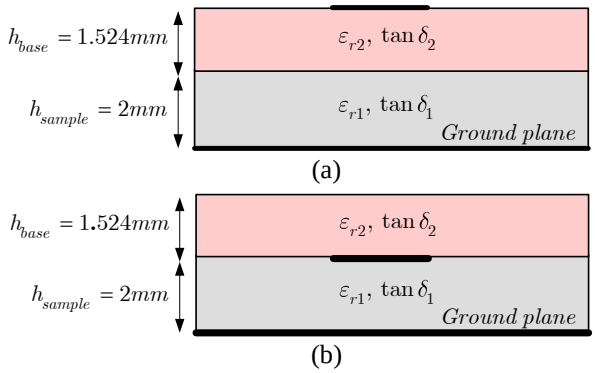

Fig. 1. Microstrip patch resonator structures as a sensor: (a) suspended patch resonator, and (b) inverted patch resonator.

III. FDTD METHOD

Finite-difference time-domain (FDTD) is a popular computational electrodynamics modeling technique. This method is easy to understand and also easy to implement in software. Since it is a time-domain method, solutions can cover a wide frequency range with a single simulation run. The FDTD method belongs to the general class of grid-based differential time-domain numerical modeling methods. The time-dependent Maxwell's equations in partial differential form are discretized using central-time central-space scheme. The resulting electric field vector components in a volume of space are solved at a given instant in time, then the magnetic field vector components in the same volume are solved at the next instant, and the process is repeated over and over until the desired transient or steady-state electromagnetic field behavior is fully evolved [6, 7]. In this paper,

the structures are simulated by 3D-FDTD method and 2 different CADs are written in C++ programming language, so it takes little time to run the codes for simulation of the structures.

Discretization of Maxwell's equations are done using well-known Yee algorithm. For example, Ampere-Maxwell equation (in 2D format) can be expressed as:

$$\frac{D_z^{n+\frac{1}{2}} - D_z^{n-\frac{1}{2}}}{\Delta t} = \frac{1}{\sqrt{\varepsilon_0 \mu_0}} \left\{ \frac{H_y^n\left(i+\frac{1}{2}, j\right) - H_y^n(i-\frac{1}{2}, j)}{\Delta x} - \frac{H_x^n\left(i, j+\frac{1}{2}\right) - H_x^n(i, j+\frac{1}{2})}{\Delta y} \right\}. \quad (5)$$

In preparation of the software code, it is important to consider the effect of complex permittivity or conductivity of the dielectric. In this case, the frequency-domain's relation between D and E, i.e.:

$$\tilde{D}(\omega) = \varepsilon \tilde{E}(\omega) + \frac{\sigma}{j\omega\varepsilon} \tilde{E}(\omega), \quad (6)$$

is converted to time domain and then discretized as:

$$E^n \approx \frac{D^n - \sigma \Delta t \sum_{i=0}^{n-1} E^i}{\varepsilon + \sigma \Delta t}. \quad (7)$$

Another important thing which must be taken into account is employing a perfect matched layer (PML) in our code. A lossy material is used as this absorbing layer which can be represented by the following discretized scheme:

$$\begin{aligned} \frac{\partial D_z}{\partial t} + \frac{\sigma_D}{\varepsilon_0} D_z &\approx \frac{D_z^{n+\frac{1}{2}} - D_z^{n-\frac{1}{2}}}{\Delta t} \\ &\quad + \frac{\sigma_D}{\varepsilon_0} . \frac{D_z^{n+\frac{1}{2}} + D_z^{n-\frac{1}{2}}}{2} \\ &= D_z^{n+\frac{1}{2}} \frac{1}{\Delta t} \left\{ 1 + \frac{\sigma_D \Delta t}{\varepsilon_0} \right\} \\ &\quad - D_z^{n-\frac{1}{2}} \frac{1}{\Delta t} \left\{ 1 - \frac{\sigma_D \Delta t}{\varepsilon_0} \right\}, \end{aligned} \quad (8)$$

in which we have used $D_z \approx \frac{D_z^{n+\frac{1}{2}} + D_z^{n-\frac{1}{2}}}{2}$.

IV. EXTRACTION OF COMPLEX PERMITTIVITY

In this paper, the structures are simulated by 3D-FDTD method. The forward problem is to compute the resonance frequency and the 3-dB bandwidth of resonators when the permittivity of the liquid under test is given. To compute the resonance frequency and 3-dB bandwidth of the structures, 2 CAD programs are written to simulate 2 structures. For each structure, the code is run for many different cases of complex permittivity for the sample layer, so a database is created of the resonance frequency and 3-dB bandwidth of the structure for different cases of sample layer. The reverse problem is to measure the resonance frequency and 3-dB bandwidth of resonator in presence of the sample layer and then recognizing the permittivity of the sample by using the database which has been prepared before. As if, each CAD for each structure was run for about 300 different cases of complex permittivity of sample layer and as if it takes about 2 minutes to run each code for one case, it took about 10 hours to create the database for each structure. At first, it may seem that making a database for each structure takes a long time, but it should be considered that this database is created just once and is used forever.

There are 2 points that should be considered. The first one is that the complex permittivity of samples are frequency dependent and the resonance frequency of each structure will changes by the change in complex permittivity of the sample, but when the CAD of each structure is run to solve the forward problem and making the database, it is supposed that the complex permittivity of the samples are constant. This supposition is right if the change in the real part and imaginary part of complex permittivity of samples is negligible or the change of resonance frequency by the change of complex permittivity of the samples is not considerable. The second considerable point is that there is a frequency shift between the resonance frequency of measurement and FDTD simulation as will be seen. As mentioned before, the method of reconstructing the complex permittivity of the sample is to measure the S_{11}-parameter of the resonator in presence of the sample and extracting the resonance frequency and 3-dB bandwidth of S_{11}-parameter, then comparing these information with the ones which have been prepared as database before and extracting the real and imaginary parts of the complex permittivity of the sample. But the frequency shift between measurement and simulation will cause a great error in extracting the sample permittivity. There is a solution for this problem and decreasing the error. The solution is to find the mean of frequency shifts for different samples and then subtracting this mean from the resonance frequency of each sample that its complex permittivity is unknown, then doing the process of finding the sample permittivity by referring to the database.

In the following part, results of simulation and measurement for both patch resonators are introduced. Section V.A reports the results of measurement and simulation for suspended resonator and Section V. B. reports the results of measurement and simulation for inverted resonator.

V. RESULTS OF MEASUREMENT AND SIMULATION

A. Suspended patch resonator

In this section, a suspended patch resonator is suggested. This suspended patch resonator is used to reconstruct the permittivity of medium loss liquids. The shape and dimensions of the structure are shown in Fig. 2. The binary mixtures of ethanol and methanol are used as samples. The proposed structure is designated to work at frequency of about 2.3 GHz. The patch dimensions are 35 mm×25 mm and the feed dimensions are 30 mm × 4 mm.

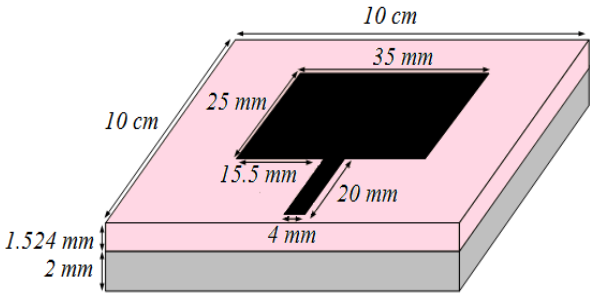

Fig. 2. Suspended patch structure.

Top view of the structure and measurement setup is shown in Fig. 3. The sample liquid is injected into the cavity by a syringe via two holes that are created in the substrate on both sides of the patch. The resonance frequency and 3-dB bandwidth of the structure are calculated from the measured data. When the sample is changed, the resonance frequency and the 3-dB bandwidth changes too, so the resonance frequency shift and the 3-dB bandwidth variation reflect the complex permittivity of the liquid under test. Figure 4 (a) is the measurement data and shows the change in the resonant frequency and quality factor when the liquid sample changes. It must be noted that in this figure eth(x) & meth(y) introduces a mixture of x% ethanol and y% methanol.

The results of simulation and measurement are depicted in Fig. 4 (b). It shows a good agreement between simulation and measurement, but there is a frequency shift between simulation and measurement which is almost constant. The mean of frequency shifts is 121.36 MHz that can be treated as mentioned before. It seems one of the most common origins for the error is that we have not used a full-wave model for the SMA connector. Also, it is seen that putting an absorbing layer in a proper distance above the circuit under test will slightly affect the results. Actually, this seems to be another reason for the difference of simulation and measurement results. It should be noted that the resonance frequency changes from 2.25 GHz to 2.41 GHz. The real and imaginary part of complex permittivity of the liquid samples are frequency dependent and will change during this frequency band, but this change is little and negligible. Therefore, in the FDTD code, the complex permittivity of our sample is supposed to be constant.

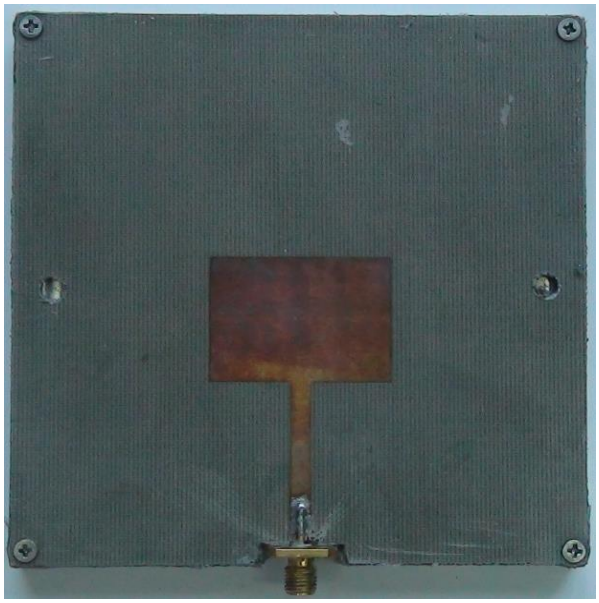

(a)

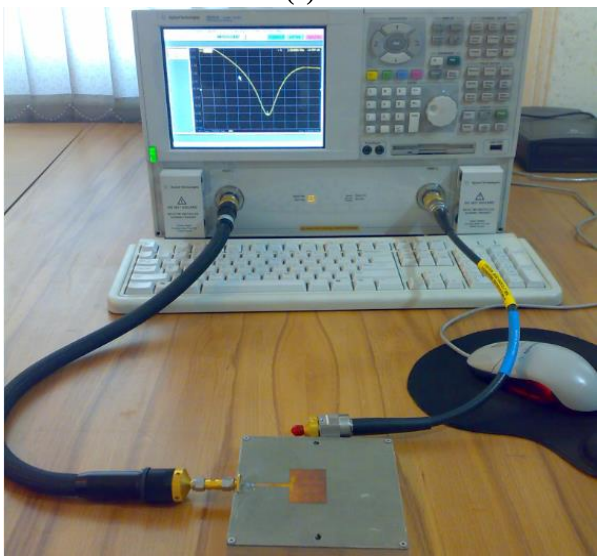

(b)

Fig. 3. (a) Top view of fabricated patch for suspended patch resonator, and (b) measurement setup.

B. Inverted patch resonator

In this section, an inverted patch resonator is proposed. This inverted patch resonator is used to reconstruct the permittivity of medium loss liquids. The shape of the structure are shown in Fig. 1 (b). Again, the binary mixtures of ethanol and methanol are used as samples. The proposed structure is designated to work at frequency of about 480 MHz. The patch

dimensions are 35 mm×25 mm and the feed dimensions are 30 mm× 4 mm. Figure 5 (a) is the measurement data and shows the change in the resonance frequency and quality factor when the liquid sample changes. In this figure eth(x) & meth(y) introduces a mixture of x% ethanol and y% methanol.

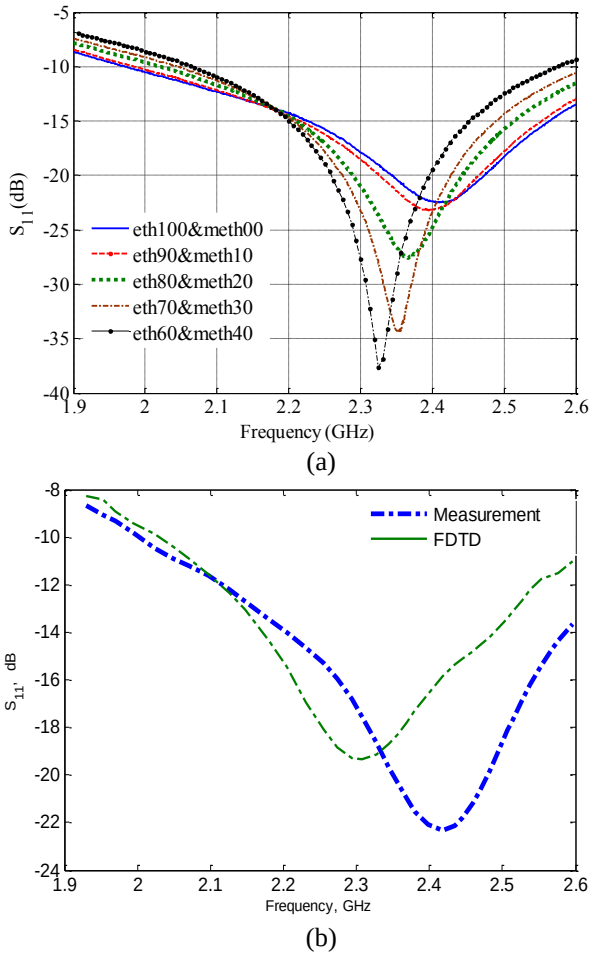

Fig. 4. (a) Measurement data of different samples for suspended patch resonator, and (b) comparison of S_{11} of measurement and 3D-FDTD simulation for ethanol 100%.

The results and errors of the test with different volume fractions of ethanol and methanol are listed in Table 1. The first column is the type of the sample. The second and fourth columns are respectively the actual values of ε' and ε'' at resonance frequency which are calculated by using the Debye function according to the data that are reported in [19]. Finally, the third and the fifth columns are the measurement errors compared to the values listed in the second and forth columns. The results show that the errors of ε' reconstruction is negligible, but the errors of ε'' reconstruction is more than ε' reconstruction, but it is acceptable.

The simulation and measurement results are depicted in Fig. 5 (b). It shows a good agreement between simulation and measurement, but there is a frequency shift between simulation and measurement and it is almost constant. The mean of frequency shifts is 37.61 MHz which can be treated as stated in the previous section. The results and errors of the test with different volume fraction of ethanol and methanol are listed in Table 2. The results show that the ε' extraction error is quite low, but that of ε'' is more, although it is satisfying.

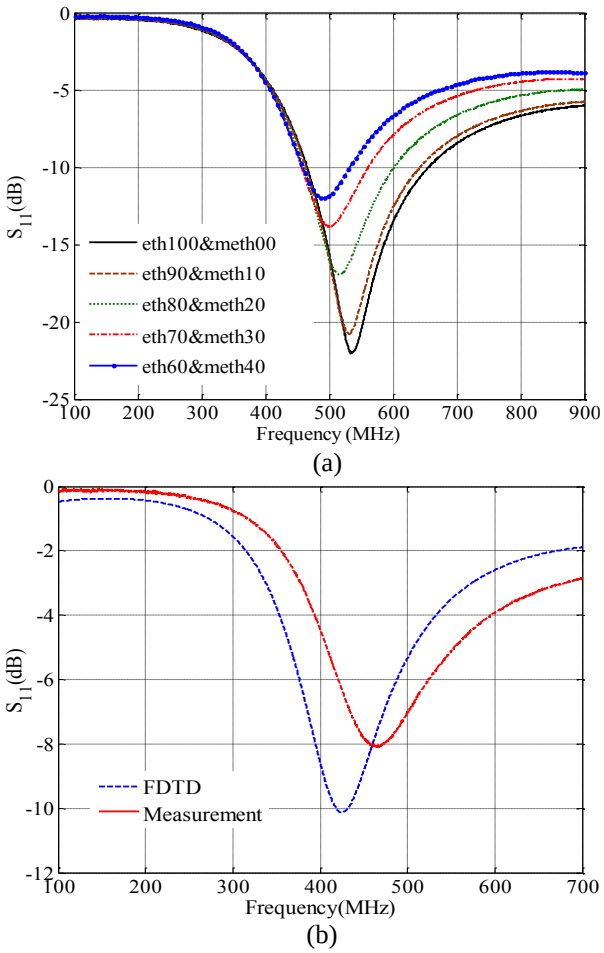

Fig. 5. (a) Measurement data of different samples for inverted patch resonator, and (b) comparison of S_{11} of measurement (----) and 3D-FDTD simulation (—).

VI. COMPARISON OF PATCH RESONATORS AS SENSORS

Two types of microstrip patch resonator are shown in Fig. 1. Both of these two patch resonators have low Q-factor as compared to the metallic cavity resonators like the one that is used in [15], but the S_{11}-parameter is deep enough to extract the accurate resonance frequency and 3-dB bandwidth from the measured S_{11}-parameter. For these two resonators, the size of the patch is determined

by the operating frequency. Also, the total substrate thickness, between patch and ground plane has a strong influence on the total Q-factor of the patch cavity. By comparing the Fig. 4 and Fig. 5, it can be seen that the S_{11}-parameter of the suspended patch resonator is much deeper than the S_{11}-parameter of inverted patch resonator, so in this case, the resonance frequency of the suspended patch resonator can be distinguished more accurately than resonance frequency of the inverted patch resonator. On the other hand, the difference between the resonance frequency of the simulation and measurement for the inverted patch is less than that for the suspended patch resonator. It means that the simulation results are closer to the measurement results for the inverted patch resonator compared to the suspended patch resonator.

According to the Tables 1 and 2, for both of the resonators, the ε'' reconstruction error is more than that of ε'. It can be seen that the error of ε' reconstruction is really low and negligible, but the error of the ε'' reconstruction is more but it is also acceptable. The mean of the ε' reconstruction error for inverted patch resonator is 1.81%, but the mean of the ε' reconstruction error for the suspended patch resonator is 1.2%, so it can be concluded that ε' reconstruction process for both of the patch resonators are accurate, but it is more exact for the suspended patch resonator. The mean of the ε'' reconstruction error for the inverted patch resonator is 6.73%, but the mean of ε'' reconstruction error for the suspended patch resonator is 8.12%. Therefore, it can be derived that ε'' reconstruction process is not as accurate as ε' reconstruction process, but it is good enough to be accepted.

It is worth to compare the results of this paper and the results in [16], because in [16] a microstrip resonator with a slot in its ground plane is enclosed in a metallic cavity and is used to reconstruct the complex permittivity of binary mixtures of ethanol and methanol in a frequency band around 2.4 GHz. In that paper, it is mentioned that the maximum relative errors of ε' and ε'' are 4.4% and 8.6%, respectively. In this paper, the maximum relative errors of ε' and ε'' for suspended patch resonator are 3.8% and 12.26% and for inverted patch resonator are 4.18% and 12.43%. In this case, it can be concluded that the ε' reconstruction in this paper is more accurate than the one in [16], but the ε'' reconstruction in [16] is more exact than the one in this paper. Also, it should be considered that the mean error for ε' extraction in this paper is really lower than that of [16] and there is a big difference between them. On the other hand, the mean error for ε'' extraction in [16] is lower than the mean error for ε'' reconstruction in this paper but there is a small difference between them. Therefore, the advantage of this paper on [16] is that the ε' reconstruction process in this paper is greatly more accurate than the one in [16].

According to the discussion above, both of the patch resonators are proper for the permittivity measurement of medium loss liquids in the frequency band about their resonance because the simulation results are really close to the measurement results. Furthermore, the permittivity extraction errors for both of these resonators are low and acceptable.

Table 1: Real and imaginary part of complex permittivity of samples and errors for suspended patch resonator

Material Under Test	ε'	Error of ε'	ε''	Error of ε''
Ethanol 100% - methanol 00%	8.0359	1.29%	7.693	5.20%
Ethanol 90% - methanol 10%	8.774	0.95%	8.544	5.80%
Ethanol 80% - methanol 20%	10.12	0.20%	9.565	7.30%
Ethanol 70% - methanol 30%	11.31	1.30%	10.44	9.03%
Ethanol 60% - methanol 40%	12.54	0.96%	11.01	10.00%

Table 2: Real and imaginary part of complex permittivity of samples and errors for inverted patch resonator

Material Under Test	ε'	Error of ε'	ε''	Error of ε''
Ethanol 100% - methanol 00%	21.45	3.72%	9.098	5.07%
Ethanol 90% - methanol 10%	23.42	3.93%	8.941	3.80%
Ethanol 80% - methanol 20%	24.97	4.18%	8.027	3.45%
Ethanol 70% - methanol 30%	26.1	1.34%	7.626	2.26%
Ethanol 60% - methanol 40%	27.5	0.90%	7.33	5.72%

VII. CONCLUSION

Two double layer microstrip resonators have been designed and fabricated for complex permittivity measurements of liquids. Complex permittivity of binary mixtures of ethanol and methanol with different volume fractions have been measured with the novel microstrip resonators. Both of these resonators were used to measure the complex permittivity of medium loss liquids. For both of these patch resonators, the simulation results are similar to the measurement results. The error of ε' extraction for both of these patch resonators are really low and negligible. The error of ε'' extraction is a little more than that of ε', but it is also acceptable. In this case, it can be concluded that both of these resonators are good for permittivity measurement in the frequency range about their resonance frequency.

REFERENCES

[1] E. Nyfors, and P. Vainikainen, *Industrial Microwave Sensors*. Artech House, USA, 1989.

[2] H. Baltes, W. Gopel, and J. Hesse (Eds.), *Sensors Update*. Wiley Inc, Germany, vol. 7, 2000.

[3] L. F. Chen, C. K. Ong, C. P. Neo, V. V. Varadan, and V. K. Varadan, *Microwave Electronics, Measurement and Materials Characterization*. John Wiley & Sons, USA, 2004.

[4] A. V. Hippel, *Dielectric Materials and Application*. Artech House, USA, 1995.

[5] A. V. Hippel, *Dielectrics and Wave*. Artech House, USA, 1995.

[6] A. Taflove, and S. C. Hagness, *Computational Electrodynamics: The Finite-Difference Time-Domain Method*. Artech House, USA, 2000.

[7] Dennis M. Sulivan, *Electromagnetic Simulation Using The FDTD Method*. IEEE Press, 2000.

[8] S. I. Ganchev, N. Qaddoumi, S. Bakhtiari, and R. Zoughi, "Calibration and measurement of dielectric properties of finite thickness composite sheets with open-ended coaxial sensors," *IEEE Trans. on Instrument, and Meas*, vol. 44, pp. 1023-1029, 1995.

[9] U. C. Hasar, "Permittivity determination of fresh cement-based materials by an open-ended waveguide probe using amplitude-only measurements," *Progress In Electromagnetics Research, PIER 97*, pp. 27-43, 2009.

[10] R. Huang and D. Zhang, "Application of mode matching method to analysis of axisymmetric coaxial discontinuity structures used in permeability and/or permittivity measurement," *Progress In Electromagnetics Research, PIER 67*, pp. 205-230, 2007.

[11] P. Queffelec and P. Gelin, "Influence of higher order modes on the measurements of complex permittivity and permeability of materials using a microstrip discontinuity," *IEEE Trans. Microw. Theory Tech*, vol. 44, no. 6, pp. 816-824, 1996.

[12] D. Shimin, "A new method for measuring dielectric constant using the resonant frequency of a patch antenna," *IEEE Trans. Microw. Theory Tech*, vol. 34, no. 9, pp. 923-931, 1986.

[13] Y. K. Verma and A. K. Verma, "Accurate determination of dielectric constant of substrate materials using modified Wolff model," *IEEE MTT-S Int. Microw. Symp. Dig*, pp. 1411-1414, 2000.

[14] M. Bogosanovich, "Microstrip patch sensor for measurement of the permittivity of homogeneous dielectric materials," *IEEE Trans. on Instrument, and Meas*, vol. 49, no. 5, pp. 1145-1148, 2000.

[15] A. K. Verma and Nasimuddin, "Determination of dielectric constant and loss-tangent of substrate sheet using microstrip patch resonator," *Microw. Opt. Technol. Lett.*, vol. 35, no. 3, pp. 175-179, 2002.

[16] L. Changjun and P. Yang, "A microstrip resonator with slotted ground plane for complex permittivity measurements of liquids," *IEEE Microw. Wireless Compon. Lett*, vol. 18, no. 4, pp. 257-259, 2008.

[17] A. K. Verma, Nasimuddin, and A. S. Omar, "Microstrip resonator sensors for determination of complex permittivity of materials in sheet, liquid and paste forms," *IEE Proc. Microw. Antennas Propag*., vol. 152, no. 1, pp. 48-54, 2005.

[18] J. Hinojosa, K. Lmimouni, S. Lepilliet, and G. Dambrine, "Very high broadband electromagnetic characterization method of film-shaped materials using coplanar waveguide," *Microw. Opt. Technol. Lett.*, vol. 33, pp. 352-355, 2002.

[19] Z. Bao, M. L. Swicord, and C. Davis, "Microwave dielectric characterization of binary mixtures of water, methanol, and ethanol," *Journal of Chemical Physics*, vol. 104, pp. 4441-4450, 1996.

Gholamreza Moradi received his B.Sc., M.Sc. and Ph.D. degrees all in Electrical Engineering, respectively from University of Tehran, in 1989, Iran University of Science and Technology in 1992 and Amirkabir University of Technology (Tehran Polytechnic) in 2002.

His main research interests include analysis and design of active and passive microwave/mm-wave circuits and systems, antennas, microwave measurements, planar structures, and numerical electromagnetics.

Moradi is currently an Associate Professor with Amirkabir University of Technology.

Mohammad Mosalanejad received the B.Sc. degree in Electronics Engineering in 2007 and the M.Sc. degree in Telecommunication Engineering in 2010, both from Amirkabir University of Technology, Tehran, Iran. He is currently pursuing the Ph.D. degree in Electrical Engineering at University of Leuven, Belgium. His research interests include antenna analysis and design, computational electromagnetics, and microwave measurement.

Analytical Model for E-Shaped Microstrip Patch Antenna

Kim H. Yeap [1], Widad Ismail [1], and Kim H. Yeap [2]

[1] School of Electrical and Electronic Engineering
Universiti Sains Malaysia, Engineering Campus, Seberang Perai Selatan, 14300 Nibong Tebal, Penang, Malaysia
kimhuat18@gmail.com, eewidad@usm.my

[2] Department of Electronic Engineering
Universiti Tunku Abdul Rahman, Jalan Universiti, Bandar Barat, 31900 Kampar, Perak, Malaysia
yeapkh@utar.edu.my

Abstract ─ This paper presents a comprehensive insight of the E-shaped microstrip patch antenna through the introduction of its cavity model and circuit model. The cavity model of the E-shaped antenna postulates a central magnetic wall that subdivides the structure into two halves, each with the TM_{001} field configuration. On the other hand, the circuit model is formulated based on the segmentation yielded from the cavity model. It infers the dual-resonance of the antenna through its circuit equivalent aspect, while avoiding cumbersome computations. Both these models offer an in depth view on the operating principles of the E-shaped antenna and effectively relates to its desired performance. A proof-of-concept design has been implemented. With the size of 147 × 112 mm^2, the antenna design resonates at 2.4 GHz and 2.5 GHz. It is noted that the reflection coefficients of its circuit model yield a deviation of less than 4 dB from the actual board measurement.

Index Terms ─ Cavity model, circuit equivalent, current distribution, E-shaped, microstrip antenna.

I. INTRODUCTION

Communication technology today serves to improve the efficiency of not only industrial systems, but also various services like military applications and medical area [1]. One of the popular patch antennas design used in the communication technology is the E-shaped microstrip patch antenna. Resembling the letter "E" in appearance, this antenna exhibits a dual-resonant behaviour on a single radiating structure, thus produces two different frequencies concurrently. Such feature avoids the need of separate antennas and provides antenna size reduction. Its applications include vehicular-satellite communication modules as well as synthetic-aperture radars (SAR) and multi-spectral scatterometers. Its potential is deemed promising.

Throughout the years, numerous research works have been performed on the E-shaped antenna [2-11], mostly conducted with computer-aided design (CAD) simulations, as summarized in Table 1. The utilization of CAD tools, such as HFSS and CST, is apparently indispensable. However it is equally important for not to solely rely on the tool itself but also to appreciate its operational insight, as exemplified in [12]. This is well evident in the case of the rectangular patch, where the introduction of its transmission line model and cavity model has since played a revolutionary role that realizes patch designs of miscellaneous sizes and geometries.

To date, the available literature on a detailed elaboration of the E-shaped patch design appears yet to require a rigorous treatment of the topic, not to mention its operating principle and design computation [7-11]. This is much due to its arbitrary shape and complex structure.

Table 1: Summary for researches on E-shaped antenna

Work	Frequency (GHz)	Simulation Tool	Features
[2]	1.9, 2.4	HFSS	30.3% bandwidth
[3]	2.4	HFSS	Suitable for MIMO applications
[4]	5.05 – 5.88	HFSS	Trim length of centre arm to tune resonances
[5]	1.9 – 2.4	IE3D	32.5% bandwidth
[6]	12, 14.5	CST	Add six slits and a trapezoidal slot to tune resonances
[7]	5 – 6	HFSS	Suitable for WLAN adaptor cards
[8]	0.75 – 0.97	IE3D	Reduces 50% antenna size with tapered slots
[9]	4.5 – 8.5	IE3D	57.36% bandwidth
[10]	5 – 6	Ensemble, HFSS	20% bandwidth
[11]	3.05 – 11.8	HFSS	Achieves ultra wideband using triple E-shaped structures

Submitted On: September 23, 2016
Accepted On: February 14, 2017

As the dual-resonance of the E-shaped antenna requires similar radiation patterns and impedance matching, the study on its basic characteristics and resonance model is critical. This study offers an in depth view of its inherent mechanism and opens a path for not only resolving its parametric issues but also anticipating future optimizations. It is attributed to this prominent reason that this paper offers a comprehensive yet concise explication on the operation of the E-shaped antenna through the introduction of its cavity model and circuit equivalent model.

II. CURRENT DISTRIBUTION AND SEGMENTATIONS

The intrinsic mechanism of the E-shaped patch antenna is intimately associated to its current distribution as shown in Fig. 1. It appears that the E-shape is forged from a rectangular patch by insetting a pair of parallel slots into it. The slots contribute to the current perturbations on the patch structure. As a result, the current flowing in the centre and at the side crosses over each other by meandering along the slots. It is also observed that the surface current concentrates on the centre and scatters at both sides. When scrutinized, the intense current flow along the central path actually forms a mirror line, breaking the antenna into two symmetrized halves. Details on this shall be elaborated in Section III.

Figure 2 illustrates a typical E-shaped patch antenna that is segmented into four sections, namely the dominant section ($S_{dominant}$), the centre section (S_{centre}), and two side sections (S_{side}'s). In principle, however, it is less legitimate to segment the antenna with a definite boundary, since the geometries of each patch are structurally inter-related. The segmentation here, nonetheless, is intended to facilitate its analysis.

$S_{dominant}$ plays the major part in the design, which is responsible for the overall radiation behaviour of the antenna. It determines the antenna resonance range and field configuration. $W_{dominant}$ and $l_{dominant}$ denotes the respective width and length of $S_{dominant}$, while h is the height of the patch substrate. S_{side} and S_{centre} fine-tune $S_{dominant}$ to resonate at the desired frequency precisely. W_{side} and l_{side} denotes the respective width and length of S_{side}, while W_{centre} and l_{centre} denotes the respective width and length of S_{centre}. $\hat{\tau}$ and $\hat{n}$ are the tangential and normal components, respectively.

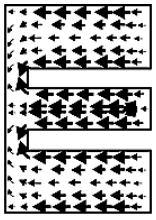

Fig. 1. Current distribution of E-shaped antenna [13].

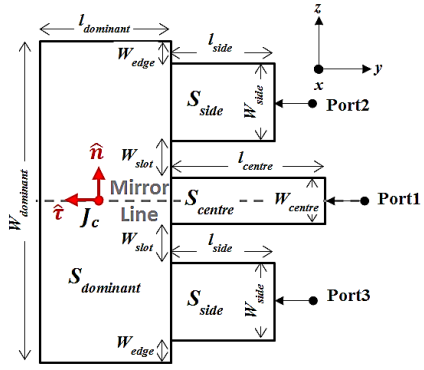

Fig. 2. Segmentation of E-shaped antenna.

III. METHODS OF ANALYSIS

The inherent principle of an E-shaped antenna is operationally complex. By studying its operating mechanism, the cavity model and circuit model have been developed to provide a methodological platform in gaining a deeper insight of its pragmatic nature while in perseverance of its simplicity.

A. Cavity model for E-shaped antenna

It is known a priori that the cavity model for a rectangular patch antenna, the region between the patch and its ground plane is conceived as an electromagnetic (EM) cavity that is bounded by magnetic walls around the periphery and by electric walls on the top and bottom sides [14]. When the patch is energized, the attractive tendency concentrates the charges on the bottom surface while the repulsive tendency pushes the like charges on the bottom surface along the edge to the top. This creates the current densities $\boldsymbol{J_t}$ and $\boldsymbol{J_b}$ on its respective top and bottom surface.

For very thin substrate ($\boldsymbol{h \ll \lambda}$), the attractive tendency dominates and most of the charges concentrate on the bottom of the patch. The current flows along the edges are very small and ultimately assumed zero. Consequently, the tangential component of the magnetic field ($\boldsymbol{H_\tau}$) along the edge is assumed zero as well. Hence, the side walls are modelled as perfect magnetic conductors. Assuming that the patch is perfectly conductive, the electric field bounded by the magnetic walls renders no tangential component ($\boldsymbol{E_\tau}$) in the normal direction. As such, the electric field is only normal directed to the patch while the magnetic field has only the transverse components in the region bounded by the patch metallization and ground plane. This creates the electric walls on the top and bottom of the cavity. According to [15], by the equivalence principle, the current densities along the periphery of the cavity are found as:

$$\boldsymbol{J_s} = \hat{n} \times \boldsymbol{H_a} \text{ and } \boldsymbol{M_s} = -\hat{n} \times \boldsymbol{E_a}. \quad (1)$$

It is noted that this formulation is exact but requires integration over its closed surface. $\boldsymbol{J_s}$, $\boldsymbol{M_s}$ is the

respective electric and magnetic current density while $\boldsymbol{E_a}$, $\boldsymbol{H_a}$ is the respective electric and magnetic field. $\boldsymbol{J_s}$, $\boldsymbol{J_t}$ are zero due to the thin substrate assumption and from image theory,

$$\boldsymbol{M_s} = -2\hat{n} \times \boldsymbol{E_a}, \tag{2}$$

resulted by the presence of the ground plane.

Due to the arbitrary shape of the patch, $S_{dominant}$ is analyzed as it governs the overall field configuration. With $W_{dominant} > \frac{W_{dominant}}{2} > l_{dominant} > h$, $S_{dominant}$ operates in the TM_{002} mode and its cavity model is shown in Fig. 3 (a). With the horizontal mirror line observed from its current distribution and referring to Fig. 2, the surface current density along the line ($\boldsymbol{J_c}$) can be dissolved as:

$$\boldsymbol{J_c} = \hat{t} \cdot J_c + \hat{n} \cdot J_c = -\hat{y} \cdot J_c + \hat{z} \cdot J_c, \tag{3a}$$

since $\hat{t}$ is proportional to the reverse $\hat{y}$ direction while $\hat{n}$ is proportional to the $\hat{z}$ direction. From Fig. 1, $\boldsymbol{J_c}$ is purely tangential, therefore,

$$\boldsymbol{J_c} = -\hat{y} \cdot J_c. \tag{3b}$$

Similar to the derivation for $\boldsymbol{J_s}$ in (1),

$$\boldsymbol{J_c} = \hat{x} \times \boldsymbol{H}, \tag{4}$$

where $\boldsymbol{H}$ is the magnetic field on the patch. Applying $(-\hat{x} \times)$ to both sides and substituting (3b) into (4),

$$\boldsymbol{H} = -\hat{x} \times (-\hat{y} \cdot \boldsymbol{J_c}) = \hat{z} \cdot \boldsymbol{J_c} = \hat{n} \cdot \boldsymbol{J_c}. \tag{5}$$

The resultant $\boldsymbol{H}$ coincides with that at its periphery, where $\boldsymbol{H}$ has only a normal component along the mirror line of the patch. The zero tangential $\boldsymbol{H}$ component implies that a magnetic wall is formed along its centre. Consequently, $S_{dominant}$ is subdivided into two symmetrical halves, $S'_{dominant}$ with each width, $W'_{dominant}$ being:

$$W_{dominant} = 2W'_{dominant}. \tag{6}$$

Likewise, S_{centre} is split into two mirrored halves, S'_{centre}'s and each with width, W'_{centre}. Hence,

$$W_{centre} = 2W'_{centre}. \tag{7}$$

With $W'_{dominant} > l_{dominant} > h$ for $S'_{dominant}$, its field configuration is TM_{001} and reflects a mirrored complement as shown in Fig. 3 (b). One crucial emphasis is $\boldsymbol{M_s}$ found with (1). Its opposite flow on the central magnetic wall notably signifies a counter effect, thereby cancelling its radiation at the centre of the patch. Correspondingly, the field propagating along the magnetic wall at both its edges with length, $l_{dominant}$ forms a pair of radiating slots on the antenna.

From the analysis of its current distribution and with reference to its dimensions, the electric field (E) and magnetic (H) components are expressed as [16]:

$$E_x = -j\omega A_{002} \cos\left(\frac{2\pi}{W_{dominant}} z'\right), \tag{8}$$

$$H_y = -\frac{2\pi}{\mu W_{dominant}} A_{002} \sin\left(\frac{2\pi}{W_{dominant}} z'\right), \tag{9}$$

$$E_y = E_z = H_x = H_z = 0, \tag{10}$$

where the subscripts x, y, z for E and H denote its respective x, y, z direction. A_{002} represents the amplitude coefficient of the TM_{002} mode while z' represents the field within the cavity. In conjunction with E and H as well as by associating it with the width of a basic rectangular patch (W) [15], the resonant frequency of the antenna (f_r) at its dominant mode is expressed as:

$$(f_r)_{002} = \frac{v_o}{W_{dominant}} \sqrt{\frac{2}{\varepsilon_r + 1}}. \tag{11}$$

B. Circuit model for E-shaped antenna

While the cavity model interprets the patch antenna from its charge distribution perspective, the circuit model infers its return losses (RLs) in circuital analogy. Its conception is purely schematic, where the mechanism of the overall patch is manifested with the elements of a high-frequency circuit network.

It has been broadly documented that the E-shaped patch antenna could be analogically represented by two inductor-capacitor (LC) resonant tanks [3], as portrayed in Fig. 4. Its first resonance is exhibited by the original rectangular patch while its second resonance is caused by the slots then inserted. Along the centre of the patch, the current flows like the rectangular design [17], where the inductance, $\boldsymbol{L_r}$ is attributed to the current path length while the capacitance, $\boldsymbol{C_r}$ is subjected to the sandwich-like structure of the substrate bounded by the patch and ground layers. At the sides of the patch, its current circumnavigates across the slots, causing an increase in its current path. The effect is modeled as an additional series inductance, $\Delta\boldsymbol{L_r}$ while the slot between the centre and side of the patch yields an additional parallel capacitance, $\Delta\boldsymbol{C_r}$. As a result, the sides of the patch resonate at a lower frequency [18].

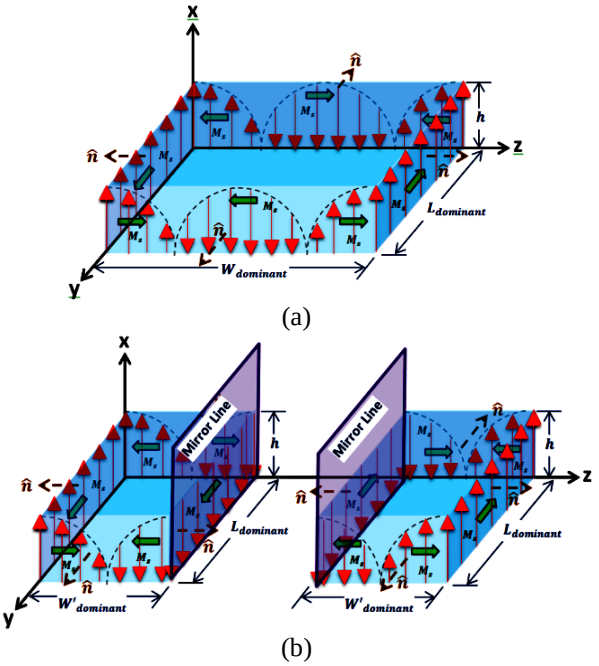

(a)

(b)

Fig. 3. (a) TM_{002} and (b) mirrored halves of $\boldsymbol{S_{dominant}}$.

The LC representation is by no mean the exact model of the E-shaped patch, but merely presents a theoretical explanation of its dual-resonance principle. In [2, 3] for instance, two LC shunt tanks are presented while in [4], two LC series tanks are shown instead. In a much entirely manner, [5, 6] analyze the E-shaped patch design by introducing a full circuit model. The models are introduced in the form of a resistor-inductor-capacitor (RLC) network, which take into account the inherent losses of the patch. Its analysis are elaborated in detail and supported with formulations. Nevertheless, the models are portrayed on a conceptual basis, and lack of prognostication of the antenna characteristics. Conversely, the antennas reported in [7-11] are designed with the aid of CAD tools.

Contrast to the previous models, the circuit equivalent model in this paper presents a full and comprehensive view of the E-shaped patch along with straightforward circuit formulations. In addition, the proposed circuit network is also able to emulate the performance of the actual design, such as its impedance bandwidth and RL. The synthesis of the LC circuit principle with the segmentation from the cavity model brings forth the formation of the proposed circuit network in Fig. 5. In this model, $\boldsymbol{S'_{dominant}}$ adopts the transmission line model of a rectangular patch and is visualized as two radiating slots separated by a transmission line [15]. Its electric field propagation is nonhomogeneous, whereby the major part concentrates in the substrate and the remaining part resides in open space. Hence, an effective dielectric constant, $\boldsymbol{\varepsilon_{reff}}$ is introduced to account for the fringing effects,

$$\varepsilon_{reff} = \frac{\varepsilon_r+1}{2} + \frac{\varepsilon_r-1}{2}\left[1+12\frac{h}{W}\right]^{-\frac{1}{2}}, \frac{W}{h} > 1, \quad (12)$$

where ε_r is the dielectric constant. The fringing length, Δl and length, l of the patch are respectively given as:

$$\Delta l = 0.412h\frac{(\varepsilon_r+0.3)\left(\frac{W}{h}+0.264\right)}{(\varepsilon_r-0.258)\left(\frac{W}{h}+0.8\right)}, \quad (13)$$

$$l = \frac{v_\circ}{2f_r\sqrt{\varepsilon_{reff}}} + 2\Delta l, \quad (14)$$

where $v_\circ$ is the speed of light in free space.

The two radiating slots are represented by two identical lines of equivalent admittance, Y_1 and Y_2 as:

$$Y_1 = Y_2 = G_1 + jB_1, \quad (15)$$

$$G_1 = G_2 = \frac{d}{120\lambda_\circ}\left[1-\frac{1}{24}(k_\circ h)^2\right], \frac{h}{\lambda_\circ} < \frac{1}{10}, \quad (15a)$$

$$B_1 = B_2 = \frac{d}{120\lambda_\circ}[1-0.636ln(k_\circ h)], \frac{h}{\lambda_\circ} > \frac{1}{10}, \quad (15b)$$

where $\lambda_\circ$ and $k_\circ$ is the respective wavelength and wavenumber in free space, G is the conductance and B is the susceptance of the radiating slot. d denotes the length of the slot, that is $l_{dominant}$ for $S'_{dominant}$. Both radiating slots are shorted by a high-admittance transmission line. Thus, its radiation resistance, $R_{dominant}$ and capacitance, $C_{dominant}$ are found by:

$$R_{dominant} = \frac{1}{G_1} = \frac{1}{G_2}, \quad (16)$$

$$C_{dominant} = \frac{B_1}{2\pi f_{dominant}} = \frac{B_2}{2\pi f_{dominant}}, \quad (17)$$

where $f_{dominant}$ is the resonant frequency for $S'_{dominant}$. The conductive and dielectric losses are deemed negligible due to its very thin metallization and substrate layers in comparison with the overall dimension of $S'_{dominant}$.

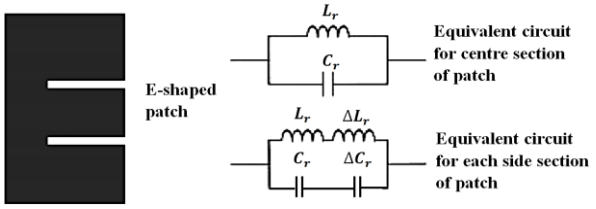

Fig. 4. LC representation of E-shaped antenna.

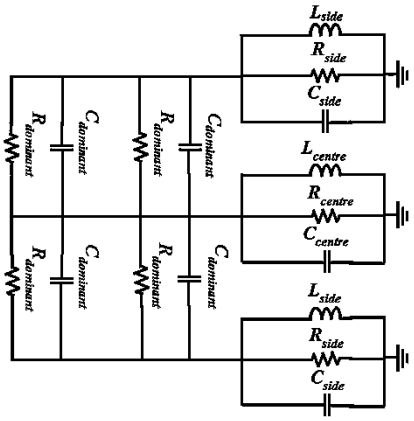

Fig. 5. Circuit equivalent model of E-shaped antenna.

In association to the LC resonant effect, S_{side} and S_{centre} are each modelled as a parallel RLC network. The total resonant resistance, R_{res} accounts for both the radiation resistance, R_r [19] and dielectric loss, R_d [20] while the conductive loss is comparatively negligible.

$$R_{res} = R_r + R_d, \quad (18)$$

$$R_d = \frac{30\tan\delta}{\varepsilon_r}\frac{h\lambda_\circ}{lW}{Q_r}^2, \quad (18a)$$

$$R_r = \frac{Q_r}{2\pi f_r C_{res}}, \quad (18b)$$

where $tan\delta$ is the dielectric loss tangent. Q_r is the radiation quality factor [21] and C_{res} is the capacitance at resonance, which are both given by:

$$Q_r = \frac{v_\circ\sqrt{\varepsilon_{reff}}}{4hf_r} - \frac{\varepsilon_{reff}\Delta l}{h}, \quad (19)$$

$$C_{res} = \frac{\varepsilon_{reff}\varepsilon_\circ Wl}{2h}cos^{-2}\left(\frac{\pi x_\circ}{l}\right), \quad (20)$$

where $\varepsilon_\circ$ is the permittivity in free space and $x_\circ$ is the distance of the feed point from the edge of $S'_{dominant}$. The resonant inductance, L_{res} is subsequently found as:

$$L_{res} = \frac{1}{(2\pi f_r)^2 C_{res}}. \quad (21)$$

In (14) – (17), l, W, f_r, and ε_{reff} correspond to the respective segment of concern, S_{side} and S_{centre}.

$R_{res} = R_{centre}$, $C_{res} = C_{centre}$, and $L_{res} = L_{centre}$ with regards to S_{centre} at resonance, where C_{centre} and L_{centre} are respectively denoted by C_r and L_r in the LC circuit representation. Similarly, $R_{res} = R_{side}$, $C_{res} = C_{side}$, and $L_{res} = L_{side}$ with regards to S_{side} at resonance. C_{side} accounts for both C_r and ΔC_r, while L_{side} accounts for both L_r and ΔL_r in the LC circuit representation.

IV. PROPOSED E-SHAPED ANTENNA

In corroborating the conception presented, an E-shaped patch antenna is proposed to operate in the Industrial, Scientific, and Medical (ISM) band. The patch is designed to resonate at 2.5 GHz through S_{centre} and 2.4 GHz through both S_{side}'s. With reference to the designation in Fig. 2, f_{r_centre} = 2.5 GHz is excited from Port 1, while f_{r_side} = 2.4 GHz is excited from Port 2 and 3, respectively. The antenna is designed on a flame retardant level-4 (FR-4) substrate with ε_r = 4.5, $tan\delta$ = 0.021, and h = 1.6 mm. Its dimensions are listed in Table 2.

Table 2: Dimensions of proposed E-shaped antenna

Segment	Dimension	Length
$S_{dominant}$	$W_{dominant}$	83.0 mm
	$l_{dominant}$	34.0 mm
S_{centre}	W_{centre}	12.0 mm
	l_{centre}	40.0 mm
S_{side}	W_{side}	20.0 mm
	l_{side}	27.0 mm
$Slots$	W_{slot}	8.5 mm
	l_{slot}	7.0 mm

A. ADS Momentum design

The proposed antenna is designed using ADS Momentum and the simulated current distribution in Fig. 6 (a) significantly indicates a tangential flow along its centre resembling that in Fig. 1. This substantiated the postulation of a mirror line bisecting the patch into two mirrored halves. Figure 6 (b) visualizes the antenna radiation pattern, which portrays a broadside radiation as customary for microstrip patch antennas.

The simulated co and cross polarizations of its radiation patterns are shown in Fig. 7. Notably, at both resonances, the radiation patterns are rather similar. At the E plane, the peak cross polarization is around 20 dB lower than the peak co polarization while its 3-dB beamwidth is 60°. At the H plane, the peak cross polarization is about 15 dB lower than the peak co polarization while its 3-dB beamwidth is 48°.

Apart from this, a parametric study has been conducted by varying the width of the slot (W_{slot}) from 6.5 mm to 10.5 mm [16], as the slots impose a direct perturbation to the surface current of the patch. The bandwidth response with respect to the changes in W_{slot} is shown in Fig. 8. It is noted that as W_{slot} expands, the bandwidths at all three ports increase proportionally.

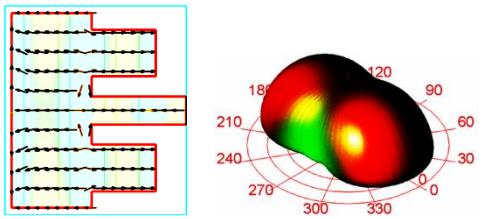

(a) (b)

Fig. 6. Simulated (a) current distribution and (b) radiation pattern for proposed E-shaped antenna.

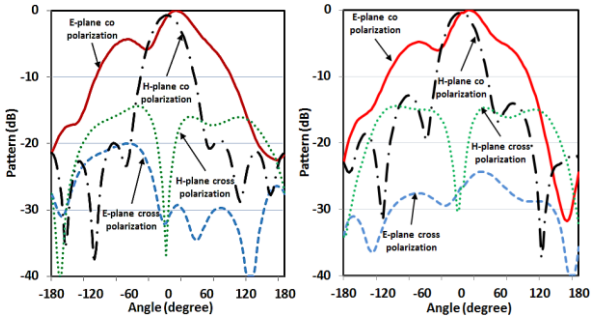

(a) (b)

Fig. 7. Simulated co and cross polarizations for radiation patterns at: (a) 2.4 GHz and (b) 2.5 GHz.

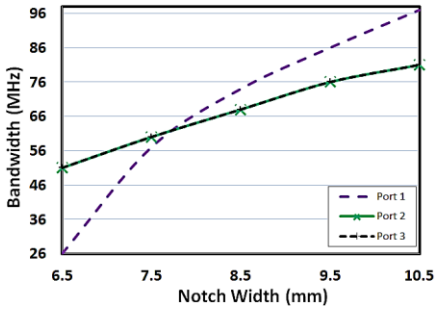

Fig. 8. Bandwidth response as W_{slot} varies [16].

B. ADS circuit model design

The circuit model is designed by substituting the dimensions in Table 2 into (12) – (21) and the parameters found are summarized in Table 3. For optimum output matching, C_{centre} and C_{side} are respectively tuned to 45.5 pF and 52 pF, through gradual decrements of the capacitances with reference to realistic part values.

It is noted that L_{side} appears lower than L_{centre}. This is attributed to the dimension for S_{centre}, which is deliberately elongated as shown in Fig. 6 (a), yielding a longer current path in the centre and thereby causing the higher inductance. This is necessary as the inductance and capacitance of a regular-sized S_{centre} is insufficient

to produce the dual resonance in close proximity. This method forces both frequencies to resonate at 100 MHz apart, without causing additional parasitic which may be deleterious to its performance.

Table 3: Circuit model parameters for proposed antenna

Parameters	Value
$R_{dominant}$	441.0 Ω
$C_{dominant}$	0.4 pF
R_{side}	63.0 Ω
L_{side}	83.0 pH
C_{side}	53.0 pF optimized to 52.0 pF
R_{centre}	63.0 Ω
L_{centre}	87.0 pH
C_{centre}	46.7 pF optimized to 45.5 pF

C. Measurement and simulation

The proposed E-shaped antenna is evaluated base on its 10 dB RL, which is expressed with its reflection coefficients specification (spec) given as:

$$\begin{cases} S11 < -10\ dB, & f = 2.5\ GHz \\ S22, S33 < -10\ dB, f = 2.4\ GHz \end{cases}. \quad (22)$$

The fabricated antenna is shown in Fig. 9, while its measured reflection coefficients and simulated reflection coefficients for the ADS Momentum and circuit model designs are plotted in Fig. 10.

The deviation of less than 4 dB between the circuit model design and the actual measurement deems that both results are co-related. It is observed that the notches for all three plots dip about its respective frequency of interest. This ascertains that the ports match remarkably at its designated frequency. It is also evident that the antenna performance complies to the spec with sufficient margins as indicated below the spec line. The plots signify that the circuit model simulated results agree coherently with the ADS Momentum simulated results as well as its measured performance. This justifies the rationale of the postulations in the cavity model.

The minor discrepancies observed between the circuit model and the measured reflection coefficients are conceivably due to the parasitic and coupling losses associated to the measurement setup that are unprecedented in the circuit model. Nevertheless, its theoretical explication is pragmatically sufficient for the analysis of an E-shaped patch design.

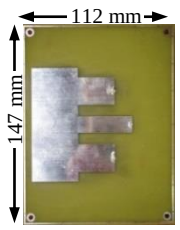

Fig. 9. Fabricated E-shaped antenna board.

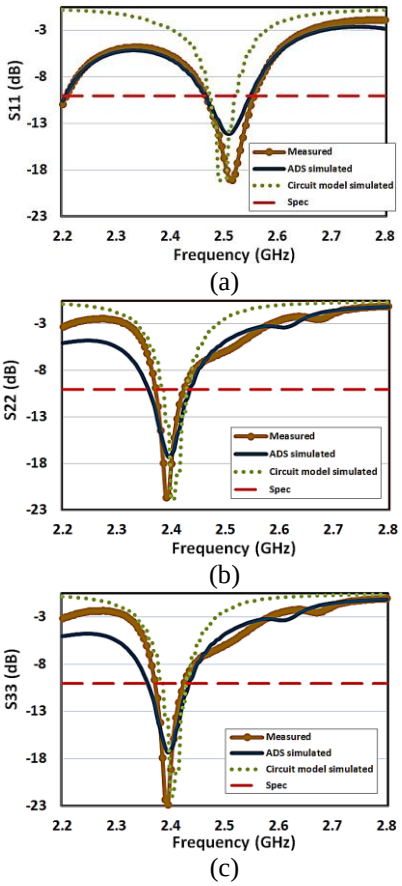

Fig. 10. (a) S11, (b) S22, and (c) S33 of the proposed E-shaped antenna as well as its circuit model.

Additionally, by substituting $W_{dominant}$ into W of (11), f_r is found as 2.2 GHz. This result appears close to the desired resonances at 2.4 GHz and 2.5 GHz of the proposed design, and thus signifies the correlation between the theoretical and its actual resonances.

V. CONCLUSION

In overall, the current distribution on the E-shaped antenna visualizes a magnetic wall along the centre of the patch. This in turn implicates its cavity model with two complementary halves. Meanwhile, its circuit model offers an alternative approach in analyzing the dual resonance effect. Rather than involving complex computations and refined meshes, this model characterizes the matching point of the antenna in a much simplistic manner. The results are almost instantaneous compared to the ADS Momentum simulation. In the generality of antenna practice, this analytical approach is believed to play an influential role in future antenna research of arbitrary shapes.

REFERENCES

[1] J. Miranda, J. Cabral, B. Ravelo, S. Wagner, C. F. Pedersen, M. Memon, and M. Mathiasen,

"Radiated EMC immunity investigation of common recognition identification platform for medical applications," *Eur. Phys. J. Appl. Phys*., vol. 69, no. 1(11002), pp. 1-8, Jan. 2015.

[2] F. Yang, X. Zhang, X. Ye, and Y. Rahmat-Samii, "Wide-band E-shaped patch antennas for wireless communications," *IEEE Trans. Antennas Propag*., vol. 49, no. 7, pp. 1094-1100, July 2001.

[3] M. B. Kadu, R. P. Labade, and A. B. Nangaonkar, "Analysis and designing of E-shape microstrip patch antenna for MIMO application," *Int. J. of Eng. and Innovative Technol*., vol. 1, no. 2, pp. 67-69, Feb. 2012.

[4] B. K. Ang and B. K. Chung, "A wideband E-shaped microstrip patch antenna for 5-6 GHz wireless communications," *Prog. Electromagn. Res*., vol. 75, pp. 397-407, 2007.

[5] V. K. Pandey and B. R. Vishvakarma, "Analysis of an E-shaped patch antenna," *Microw. Opt. Technol. Lett*., vol. 49, no. 1, pp. 4-7, Jan. 2007.

[6] Z. Manzoor and G. Moradi, "Optimization of impedance bandwidth of a stacked microstrip patch antenna with the shape of parasitic patch's slots," *Appl. Comput. Electromagn. Society (ACES) J*., vol. 30, no. 9, pp. 1014-1018, Sep. 2015

[7] Y. Ge, K. P. Esselle, and T. S. Bird, "E-shaped patch antennas for high-speed wireless networks," *IEEE Trans. Antennas Propag*., vol. AP-52, no. 12, pp. 3213-3219, Jan. 2005.

[8] A. A. Deshmukh and G. Kumar, "Compact E- and S-shaped microstrip antennas," *Electron. Lett*., vol. 3B, pp. 389-392, July 2005.

[9] P. K. Singhal and P. Moghe, "Design of a single layer E-shaped microstrip patch antenna," *Asia Pac. Microw. Conf*., Suzhou, China, Dec. 2005.

[10] Y. Ge, K. P. Esselle, and T. S. Bird, "Broadband E-shaped patch antennas for 5-6 GHz wireless computer networks," *IEEE Antennas Propag. Society Int. Symp*., pp. 942-945, June 2003.

[11] N. Ojaroudi, S. Amiri, F. Geran, and M. Ojaroudi, "Band-notched small monopole antenna using triple E-shaped structures for UWB systems," *Appl. Comput. Electromagn. Society (ACES) J*., vol. 27, no. 12, pp. 1022-1028, Dec. 2012.

[12] B. Ravelo, "Synthesis of n-way active topology for wide-band RF/microwave applications," *Int. J. Electron*., vol. 99, no. 5, pp. 597-608, May 2012.

[13] K. L. Wong and W. H. Hsu, "A broad-band rectangular patch antenna with a pair of wide slits," *IEEE Trans. Antennas Propag*., vol. 49, no. 9, pp. 1345-1347, Sep. 2001.

[14] Y. T. Lo, D. Solomon, and W. F. Richards, "Theory and experiment on microstrip antennas," *IEEE Trans. Antennas Propagat*., vol. 27, no. 2, pp. 137-145, Mar. 1979.

[15] C. A. Balanis, *Antenna Theory, Analysis and Design*. John Wiley & Sons, 2005.

[16] K. H. Yeap, W. Ismail, S. L. Yap, and K. H. Yeap, "Parametric study for E-shaped microstrip patch antenna," *Malaysian J. of Science*, vol. 35, no. 2, pp. 284-318, Dec. 2016.

[17] K. F. Lee and W. Chen, *Advances in Microstrip and Printed Antennas*. Wiley, 1997.

[18] S. K. Patel and Y. P. Kosta, "E-shape microstrip patch antenna design for GPS application," *Int. Conf. Current Trends Technol*., Dec. 2011.

[19] C. Yildiz and K. Guney, "Simple model for the input impedance of rectangular microstrip antenna," *J. of Eng. Sciences*, vol. 4, no. 3, pp. 733-738, 1998.

[20] Technical Report 00929 Physical Science Laboratory, Theoretical Investigation of the Microstrip Antenna, New Mexico State University, 1979.

[21] K. Guney, "Radiation quality factor and resonant resistance of rectangular microstrip antenna," *Microw. Opt. Technol. Lett*., vol. 7, no. 9, pp. 427-430, June 1994.

Kim Huat Yeap received his B.Eng. (Hons.) from Universiti Tenaga Nasional in 2004 and M.Sc. from Universiti Sains Malaysia in 2012. He is currently pursuing his Ph.D. in Universiti Sains Malaysia. His research interest focuses in the areas of antennas and mixers.

Widad Ismail received her B.Eng. (Hons.) from University of Huddersfield in 1999 and Ph.D. from University of Birmingham in 2004. She is currently a Professor in School of Electrical and Electronic Engineering, Universiti Sains Malaysia. Her research interest focuses in the area of antennas, mixers, and Radio Frequency identification systems.

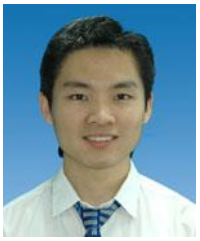

Kim Ho Yeap received his B.Eng. (Hons.) from Universiti Teknologi Petronas in 2004, M.Sc. from Universiti Kebangsaan Malaysia in 2005, and Ph.D. from Universiti Tunku Abdul Rahman in 2011. He is currently an Associate Professor in Faculty of Engineering and Green Technology, Universiti Tunku Abdul Rahman. His research interest includes microelectronics devices, waveguides, and radio telescopes.

A Circularly Polarized Miniaturized Patch Array Using Combination of Circle and Rectangular Lines in the Sequential Phase Feed Structure

Mohammad Hosein Rasekhmanesh, Pejman Mohammadi*, and Asrin Piroutiniya

Department of Electrical Engineering
University of Islamic Azad University, Urmia Branch, Urmia, Iran
*p.mohammadi@iaurmia.ac.ir

Abstract ─ A sequential phase (SP) feed array antenna circularly polarized (CP) with 2×2 patch array is presented. The feeding network consist of two piece of circle that are filled with rectangular lines and have four arms that make 90^0 phase difference for the corner truncated elements which are connected to the feeding network. The combination of circle and rectangular lines reduces the size of the feeding network and thus, the overall size of the antenna with good characteristics to prove the antenna performance, the prototype antennas built and the results come in the form of: the measured 10 dB impedance bandwidth is 0.5 GHz (3.45 - 3.95 GHz), and the measured 3-dB AR bandwidth is 0.3 GHz (3.45 - 3.75 GHz).

Index Terms ─ Circular polarization, feeding network, incomplete ground, microstrip array, radiating patch element, sequential rotation.

I. INTRODUCTION

One of the most important subjects in designing antenna is to achieve circular polarization (CP), which also includes 2×2 patch array design. Sequential rotation (SR) techniques contribute significantly to achieving the optimal CP bandwidth [1].

So far, different feeding networks have been introduced which are discussed in [2-11]. These feeding networks have more complex structures. Nowadays, SR feeding networks with united structure is more interesting in which, narrow CP bandwidth problem can be solved.

Radiating elements in the patch have a smaller bandwidth than the DRAs (dielectric resonator antenna) due to the nature of the patch elements. For example, use of the center-truncated patch element, reduces characteristic of the AR bandwidth. The samples of these antennas have been introduced in [12, 14], which almost have a narrow bandwidth. Therefore, the ability to design 2×2 patch array with a wider bandwidth is very attractive.

Another issue that must be considered is the antennas dimensions. A large feeding network leads to a large antenna. Also, it is preferable that eliminate network complexity as much as possible.

According to the explanations that were given, we conclude that a desire SP feed should be able to provide some conditions. One significant problem is that the feeding network with four arms should have the same amplitude signals and 90^0 phase shifting on the arms to have 0^0, 90^0, 180^0, 270^0 phases. Secondly, the issue of commuting the antenna impedance to the feed I/O port impedance for contractual values should be established. Finally, the dimensions of the antenna have been discussed as to design a small feeding network reduces the size of the antenna.

Of course, in the design of a small antenna we should be careful to maintain desired characteristics of the antenna such as gain and AR bandwidth. In the following, an antenna has been introduced which provides these requirements very good.

II. ANTENNA DESIGN

Figure 1 (a) shows the structure of the patch array. The central section is the feeding network which includes two 90^0 arcs of a circle that is filled with rectangular lines. The reason of using this combination is to minimize the size of the feeding network. This design, based on two essential points: the first point is that by shrinking the size of the antenna, the gain is reduced and to compensate the reduced gain, the rectangular lines are designed quite compressed. Another issue is the impact of the network feeding to CP bandwidth. With regard to these two issues, the feeding network is designed as shown in Fig. 1 (b).

At the radiation patch element, the corner-truncated square technique is used which is connected to the feeding network with four strips. The feeding port located at the center of the substrate and feeding network. The antenna that has been introduced has a single-layer patch that is printed on the FR4 substrate with ε_r=4.4, tan δ = 0.024 and thickness of h=1.6 mm. The patch dimensions have been optimized by the HFSS full wave simulator and details of the patch array are shown in Table 1, and Table 2 showing details of the

Submitted On: November 2, 2015
Accepted On: March 10, 2017

feeding network.

Table 1: Dimensions of the patch

Parameter	mm	Parameter	mm
l_s	80	s_3	15.6
l_1	19.9	s_4	18.625
w_1	20	z	5.3
s_1	15.6	a	90^0
s_2	17		

Table 2: Dimensions of the feeding network

Parameter	mm	Parameter	mm
w_2	0.8	l_7	2.86
w_3	1.25	l_8	3.225
l_2	5.2	l_9	6.36
l_3	1.625	l_{10}	5.735
l_4	2.28	l_{11}	3.125
l_5	3.125	l_{12}	2.86
l_6	1.625	l_{13}	2

The center frequency of the antenna is 3.6 GHz. The value of λ_g is calculated according to the Equation (1) ((w) is the width of the microstrip line in feeding network and (h) is the height of the substrate). Different paths are shown in Fig. 1 (c), that each path creates a 90^0 phase difference. The length of each arc is $\lambda_g/4$. With regard to this issue, the value of the radius is calculated as r=8.15 mm.

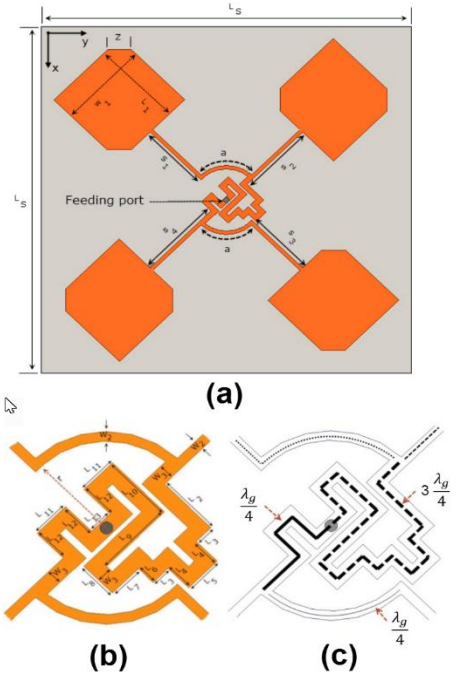

Fig. 1. Geometry of the proposed 2×2 antenna array: (a) dimensions of the antenna, (b) dimensions of the feeding network, and (c) length of paths.

By creating different paths, sequential phases of 0^0, 90^0, 180^0, 270^0 can be seen at the four arms (Fig. 2). The 90^0 phase differences at the center frequency of 3.6 GHz at the four arms of feeding network is visible in the Fig. 2 (c). When the value of the phase in output 2 is about -150^0, the values of the phases of port 3, port 4 and port 5 are -60^0, 30^0 and 120^0 respectively. Furthermore, the simulated results of the scattering parameters when port-1 is excited, is shown in Fig. 2 (b).

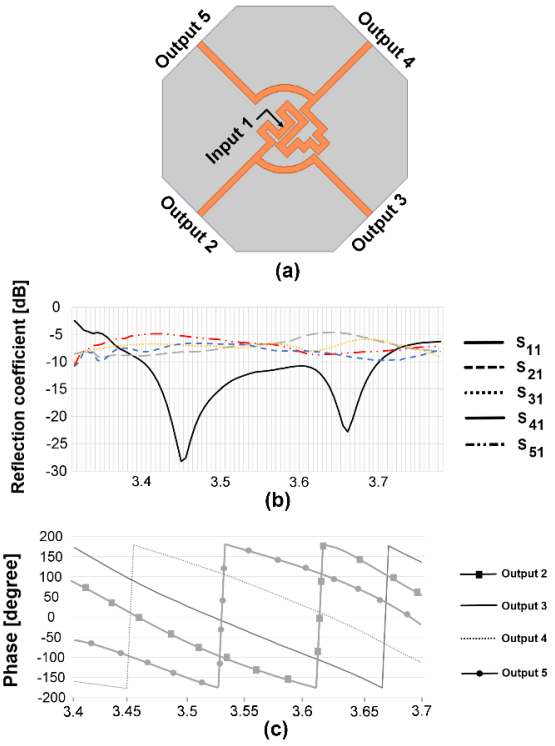

Fig. 2. (a) Structure of feeding network, (b) simulated results of the scattering parameters when port-1 is excited, and (c) simulated sequential phase differences at four arms of feeding network in desired frequency range.

The current distribution on the array at the frequency of 3.6 GHz is shown at Fig. 3. Direction of flow at the phases of 0^0, 90^0, 180^0, 270^0 is counter clockwise and this circular motion leads to the circular polarization:

$$\lambda_g = \frac{v_p}{f} = \frac{c}{f\sqrt{\varepsilon_{eff}}}. \quad (1)$$

If $(\frac{w}{h}) < 1 \rightarrow$

$$\varepsilon_{eff} = \frac{\varepsilon_r + 1}{2} + \frac{\varepsilon_r - 1}{2}\left[\frac{1}{\sqrt{1 + 12\frac{h}{w}}} + 0.04\left(1 - \frac{w}{h}\right)^2\right].$$

If $(\frac{w}{h}) \geq 1 \rightarrow$

$$\varepsilon_{eff} = \frac{1 + \varepsilon_r}{2} + \left[\frac{\varepsilon_r - 1}{2\sqrt{1 + 12\frac{h}{w}}}\right].$$

Figure 4 shows the schematic diagram of the SP feed. One of the impedances of z_1 is for the arm of the feeding network and arc of the circle (doted line in the Fig. 1 (c)) and the other one is for the arm of the feeding network alone (thin dashed line in the Fig. 1 (c)). According to the Fig. 3, the z_1 impedances are parallel with each other and the collection of the z_1 impedances are parallel too. The parallel impedances of z_1 are series with the impedances of z_2. Impedances of z_2 are for the paths of the $\lambda_g/4$ (thick line in the Fig. 1 (c)) and $3\lambda_g/4$ (thick dashed line in the Fig. 1 (c)) in the feeding network. Impedance of the feed line is 50 Ω, so we have a good impedance matching between the feed line and feeding network. According to the Equation (2), the impedance of feeding network has calculated as Z= 65 Ω ((w) is the width of the microstrip line in feeding network and (h) is the height of the substrate):

$$\text{If } \left(\frac{w}{h}\right) < 1 \rightarrow Z = \frac{60}{\sqrt{\varepsilon_{EFF}}} \ln\left(8\left(\frac{h}{w}\right) + 0.25\left(\frac{w}{h}\right)\right). \quad (2)$$

$$\text{If } \left(\frac{w}{h}\right) \geq 1 \rightarrow Z = \frac{120\pi}{\sqrt{\varepsilon_{eff}}} / \left(\frac{w}{h} + 1.393 + 0.667 \ln\left(\frac{w}{h} + 1.444\right)\right).$$

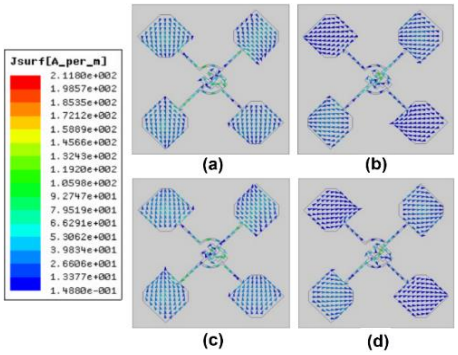

Fig. 3. Current distribution on the proposed array at 3.6 GHz with different phase: (a) 0^0, (b) 90^0, (c) 180^0, and (d) 270^0.

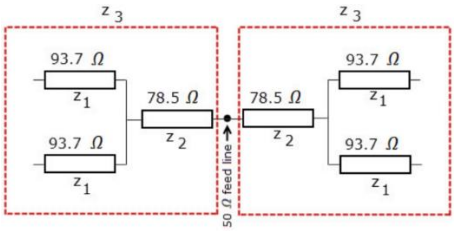

Fig. 4. Schematic diagram of the SP feed.

III. EXPERIMENTAL RESULT

Figure 5 shows the prototype of the antenna with 2×2 patch array. In Fig. 6, the measured value of reflection coefficient is shown. It can be seen that there is a good matching between simulated and measured results. The -10dB reflection coefficient bandwidth is from 3.45 GHz to 3.95 GHz. A little difference between simulated and measured results is related to dielectric loss, fabrication error and differences in the characteristics of the substrate.

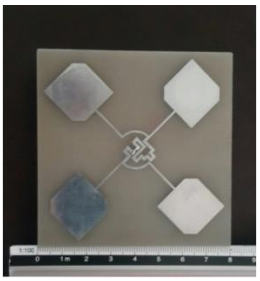

Fig. 5. Prototype of the proposed 2×2 patch array.

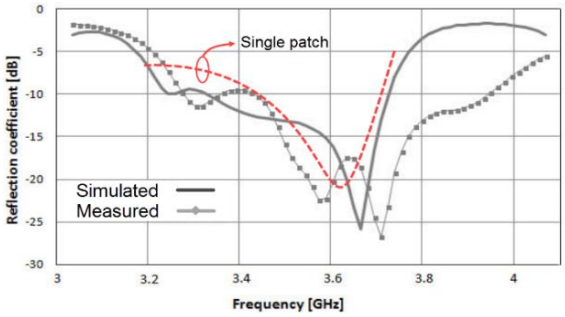

Fig. 6. Simulated and measured reflection coefficient of the 2×2 array.

Figure 7 shows the simulated and measured results of the AR parameter. The AR bandwidth is from 3.45 GHz to 3.75 GHz. In Fig. 8, the simulated and measured results of the gain is shown. According to the AR bandwidth, the gain in the desired range is more than 4 dB and the maximum gain is 7.8 dB, at the frequency of 3.7 GHz. The results of the radiation pattern at the frequencies of the 3.5 GHz and 3.6 GHz are shown at Fig. 9. According to the results, at the +Z direction, the gain of co-polarization (RHCP) is about 12dB higher than the cross-polarization (LHCP) and good agreement is observed between simulated and measured results.

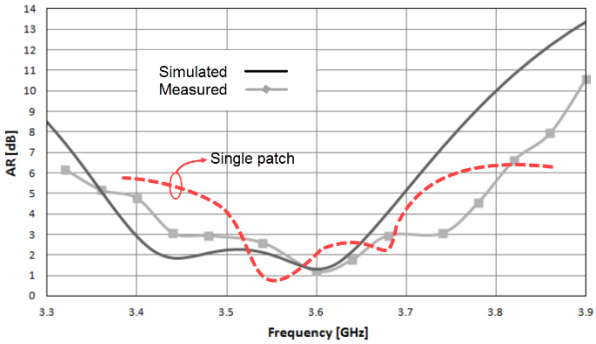

Fig. 7. Simulated and measured axial ratio of the 2×2 patch array.

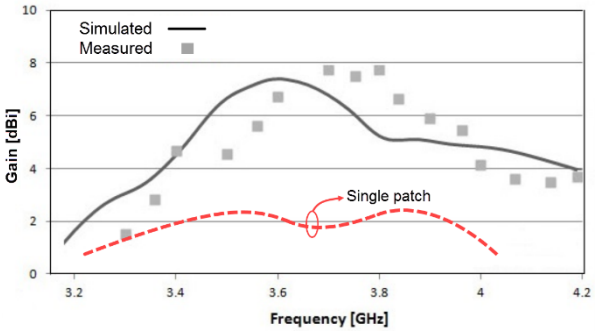

Fig. 8. Simulated and measured gain of the 2×2 patch array.

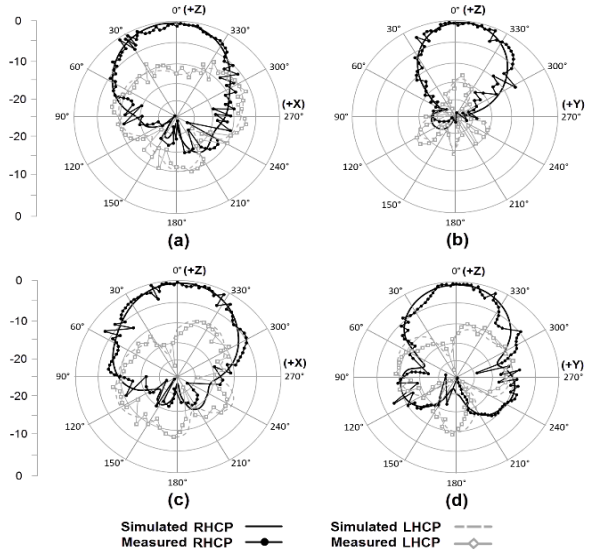

Fig. 9. Normalized radiation pattern at 3.5 and 3.6 GHz: (a) simulated and measured RHCP and LHCP in x-z plane at 3.5 GHz, (b) simulated and measured RHCP and LHCP in y-z plane at 3.5 GHz, (c) simulated and measured RHCP and LHCP in x-z plane at 3.6 GHz, and (d) simulated and measured RHCP and LHCP in y-z plane at 3.6 GHz.

Table 3 shows a comparison between the proposed patch array and the other single-layer patch arrays. One of the significant issues is the size of the feeding network that is small as much as possible. Another important issue is the material of the substrate which is reduced the cost of the antenna. It was also observed that the size of the proposed antenna is smaller than the other antennas.

According to the given explanations and with regard to the common bandwidth of s_{11}< -10 dB and AR< 3dB, we conclude that the operation of the antenna is quite acceptable. In addition, for high gain applications the proposed SP feed can be developed to the large CP planar array. By using compact and uniform properties, the larger scale $2^N \times 2^N$ arrays can be derived from the reported 2×2 SP feed and array element. For instance, the structure of 4×4 arrays by using the extended feeding network based on the module unite of the proposed 2×2 SP feed is shown in Fig. 10.

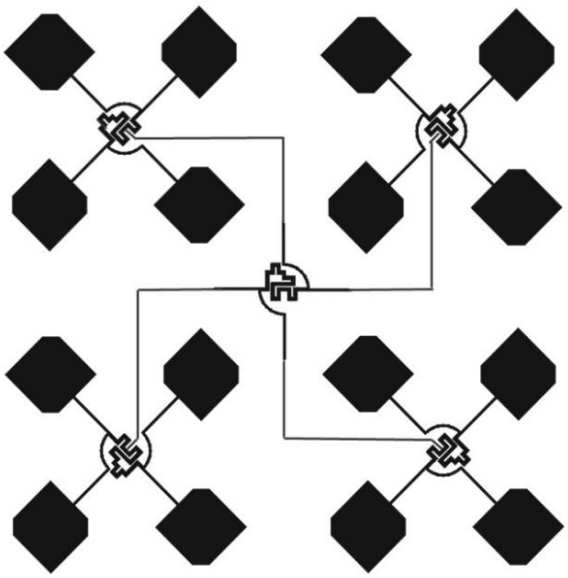

Fig. 10. Extended feeding network to achieve 4×4 SR arrays.

Table 3: A comparison between the proposed patch array and the other single-layer patch arrays

2×2 Patch Arrays	Ref [12]	Ref [13]	Ref [14]	Ref [15]	Proposed Antenna
10-db reflection coefficient bandwidth (%)	7.3	15.45	8	6	13.9
3-db AR bandwidth (%)	4.4	5.4	4.8	6.8	8.3
Material of substrate	Rogers	Rogers	FR4	Teflon	FR4
Substrate dimensions	Not given	3.43×3.43×0.039	3.15×3.15×0.022	2.83×2.83×0.085	2.59×2.59×0.052

IV. CONCLUSION

In this paper, a single layer SP feed array antenna with hybrid design of circle and rectangular lines in feeding network is introduced. The common 10dB impedance bandwidth and 3dB AR bandwidth is 300 MHz or 8.3% corresponding to the center frequency of 3.6 GHz. The maximum gain is 7.8 dB at the frequency of 3.7 GHz. The aim is to design an antenna with a small size and acceptable performance that is proved in comparison with the other single-layer 2×2 patch arrays. Design a SP feed with repeatability is an advantage. The presented design applies in the $2^N \times 2^N$ applications. With a

comparison that is done, it can be seen that in the same material of the substrate, the area of the substrate has greatly decreased (about 67%), while the common bandwidth of 10dB reflection coefficient and 3dB AR is increased about 3.5%.

REFRENCES

[1] T. Teshirogi, M. Tanaka, and W. Chujo, "Wideband circularly polarised array antenna with sequential rotations and phase shifts of elements," *Int. Symp. on Ant. and Prop., ISAP 85*, Tokyo, 1985.

[2] R. Ramirez, F. Flaviis, and N. G. Alexopoulos, "Single-feed circularly polarized microstrip ring antenna and arrays," *IEEE Trans. Antennas Propag.*, vol. 48, no. 7, pp. 1040-1047, 2000.

[3] H. Iwasaki, "A circularly polarized rectangular microstrip antenna using single fed proximity coupled method," *IEEE Trans. Antennas Propag.*, vol. 43, no. 8, pp. 895-897, Aug. 1995.

[4] W. K. Lo, C. H. Chan, and K. M. Luk, "Circularly polarized microstrip antenna array using proximity coupled feed," *Electron. Lett.*, vol. 34, no. 23, pp. 2190-2191, Nov. 1998.

[5] M. H. Rahmani and A. Pirhadi. "Optimum design of conformal array antenna with a shaped radiation pattern and wideband feeding network," *ACES Journal*, vol. 29, no. 1, Jan. 2014.

[6] J. W. Wu and J. H. Lu, "2×2 circularly polarized patch antenna arrays with broadband operation," *Microw. Opt. Technol. Lett.*, vol. 39, no. 5, pp. 360-363, 2003.

[7] L. Bian and X. Q. Shi, "Wideband circularly polarized serial rotated 2×2 circular patch antenna array," *Microw. Opt. Technol. Lett.*, vol. 49, no. 12, pp. 3122-3124, 2007.

[8] Y. Lu, D. G. Fang, and H. Wang, "A wideband circularly polarized 2×2 sequentially rotated patch antenna array," *Microw. Opt. Technol. Lett.*, vol. 49, no. 6, pp. 1405-1407, 2007.

[9] K. H. Lu and T.-N. Chang, "Circularly polarized array antenna with corporate-feed network and series-feed elements," *IEEE Trans. Antennas Propag.*, vol. 53, no. 10, pp. 3288-3292, 2005.

[10] J. Janapsatya, Nasimuddin, and K. P. Esselle, "Jawidening the bandwidth of single-fed circularly polarized microstrip patch antenna using sequential array," in *Proc. Antennas Propag. Soc. (AP-S) Int. Symp.*, pp. 1-4, July 2008.

[11] S. S. I. Mitu and F. Sultan, "Size reduced array antenna with enhanced directivity," *ACES Journal*, vol. 30, no. 11, Nov. 2015.

[12] I. J. Chen, "CPW-fed circularly polarized 2×2 sequentially rotated patch antenna array," in *Microw. Conf. Proc. (APMC)*, vol. 4, 2005.

[13] A. Chen, Y. Zhang, Z. Chen, and S. Cao, "A Kaband high gain circularly polarized microstrip antenna array," *IEEE Antennas Wireless Propag. Lett.*, vol. 9, pp. 1115-1118, 2010.

[14] S. Lin and Y. Lin, "A compact sequential-phase feed using uniform transmission lines for circularly polarized sequential-rotation arrays," *IEEE Trans. Antennas Propag.*, vol. 59, no. 7, pp. 2721-2724, 2011.

[15] Y. Li, Z. Zhang, and Z. Feng, "A sequential-phase feed using a circularly polarized shorted loop structure," *IEEE Trans. Antennas Propag.*, vol. 61, no. 3, pp. 1443-1447, 2013.

Mohammad Hosein Rasekhmanesh was born in Tehran, Iran, in 1986. He received the M.Sc. degree in Electrical Engineering from Department of Electrical Engineering, Science and Research Branch, Islamic Azad University, West Azerbaijan, Iran. His research interests include antennas, circular polarization and radar application.

Pejman Mohammadi was born in 1973 in Tehran, Iran. He received Ph.D. in Electrical Engineering from Middle East Technical University Turkey. Since 2001, he has been with the Department of Electrical Engineering, Islamic Azad University of Urmia, where he is currently a Lecturer. His research interests include microwave component SIW, microstrip antennas, small antennas for wireless communications and reconfigurable structure.

Asrin Piroutiniya was born in 1983 in Urmia, Iran. She received her B.Sc. degree in Electrical Engineering from Azad University, Naein Branch and M.Sc. degree in Electrical Engineering from Department of Electrical Engineering, Science and Research Branch, Islamic Azad University, West Azerbaijan, Iran. Her research interests include substrate integrated waveguide technology, power divider and feeding networks for array antenna and antennas.

A Miniaturized LPF with Sharp Transition-band Using Semi-circle Resonators

Saeed Roshani [1], A. R. Golestanifar [2], A. H. Ghaderi [2], and Sobhan Roshani [1]

[1] Department of Electrical Engineering, Kermanshah Branch, Islamic Azad University, Kermanshah, Iran

[2] Young Researchers and Elite Club, Kermanshah Branch, Islamic Azad University, Kermanshah, Iran

Abstract ─ In this paper, a miniaturized microstrip low-pass filter (LPF) with sharp transition-band, wide stop-band and negligible insertion-loss in pass-band is proposed using semi-circle and butterfly resonators. The cutoff frequency of the proposed LPF is 1.75 GHz. The proposed LPF presents a wide stop-band from 2.1 to 23.73 GHz (2^{nd}-14^{th} harmonics) with -20 dB attenuation level. The overall dimension of the proposed filter is $0.11\lambda_g \times 0.1\lambda_g$. The sharpness of transition-band is 112 dB/GHz, from 1.75 to 2.26 GHz with corresponding attenuation levels of -3 dB and -60 dB, respectively. The insertion-loss in pass-band is less than 0.05 dB. The proposed LPF is simulated, fabricated and measured, which there is a good agreement between the results of simulation and measurement. The LPF has been designed for L-band applications**.**

Index Terms ─ L-band, LPF, open stub, semi-circle resonator, sharp transition-band.

I. INTRODUCTION

Microstrip low-pass filters with small size, low cost, wide stop-band and sharp cut-off frequency are necessary demand for wireless communication circuits to suppress undesirable signals [1, 2]. In [3], a low-pass filter with sharp transition-band was introduced using defected ground structure (DGS). This filter suffers, narrow stop-band and large circuit dimension. In [4], a miniaturized LPF with high return-loss in pass-band was reported using interdigital structure. Slow transition-band and the limited stop-band are draw backs of this work. In [5], a LPF with sharp cut-off frequency was presented using triangular and T-shaped resonators. This structure has low suppression level in stop-band and occupied large area. In [6], a microstrip LPF with stepped-impedance units was presented. Negligible ripple in pass-band and small size are advantages of this work, although roll-off rate is not so sharp. A low-pass filter was reported in [7], which has low suppression level in the stop-band area. In [8], a LPF with hairpin-resonator was presented, which the stop-band is narrow. In [9, 10], LPFs with small size were introduced using hairpin resonators, which gradual transition-band and narrow stop-band are undesired features of these works. In [11], a low-pass filter with defected rectangular resonator was reported. The cut-off frequency of the filter is not sharp and the stopband is narrow. In [12], a LPF with low rejection level and narrow stop-band was introduced. In [13], a microstrip LPF was reported using multi-mode resonators, which the transition-band is not sharp. In [14], a LPF with wide stop-band was presented based on DGS. The transition-band of this filter is not so sharp. In [15], a LPF with Butterworth response was presented. This LPF has a sharp transition-band and wide stop-band, but the structure has low attenuation level compared with conventional Butterworth filter. In [16], a microstrip structure with rectangular resonators was reported. To extend the stop-band, a DGS composed of four u-shaped resonators was utilized. However, the presented LPF suffers, ripple in pass-band and slow transition-band.

In this study, a novel structure with sharp transition–band, wide stop-band, low ripple in passband and miniaturized size is proposed. The stop-band is extended to 23.73 GHz with -20 dB attenuation level. All electro-magnetic (EM) simulations of microstrip layouts and all L-C simulations of equivalent circuits are performed using Advanced Design System (ADS 2011.10) software (Agilent Technologies, Santa Clara, CA). Scattering parameters measurement of fabricated device and EM simulations results of proposed LPF are in good agreement, which confirms the validity of the proposed LPF.

II. DESIGN PROCESS

A. Primitive semi-circle resonator

The primitive semi-circle resonator is designed on RT/Duroid 5880 substrate with relative permittivity of 2.2, thickness of 0.381 mm and loss-tangent of 0.0009. Also copper with thickness of 10μm is utilized as conductor strip lines. In order to design an LPF with wide stopband, a semi-circle resonator is used. The

Submitted On: October 14, 2016
Accepted On: March 19, 2017

layout of the primitive semi-circle resonator is depicted in Fig. 1 (a). This structure consists of a high-impedance line and a semi-circle shaped stub, which they are connected to the transmission line, based on Fig. 1 (a). The L-C equivalent circuit of this resonator is demonstrated in Fig. 1 (b), which, the inductances and capacitance of the corresponding transmission lines are L_1, L_2 and C_1, respectively. L_3 is inductance of high-impedance line and C_2 is the sum of open-ended and low-impedance lines capacitances. The EM simulations and L-C equivalent circuit simulation results are in good agreement and there is a transmission-zero (T_{Z1}) at 8.8 GHz with -55 dB attenuation level as shown in Fig. 1 (c). The L-C equivalent circuit values are optimized by ADS software and they are summarized in Table 1. The dimensions of this structure are: A_1=9.73, A_2=3.96, A_3=0.23, A_4=0.1, A_5=1.17, A_6=1.5, r=4.12 (unit: millimeter) and ϕ_1=170°.

Table 1: The optimized values of L-C equivalent circuit

Parameter	C_1	C_2	L_1	L_2	L_3
Values	1.264	0.561	7	2.74	0.597

(Units: C=[pF]; L=[nH]).

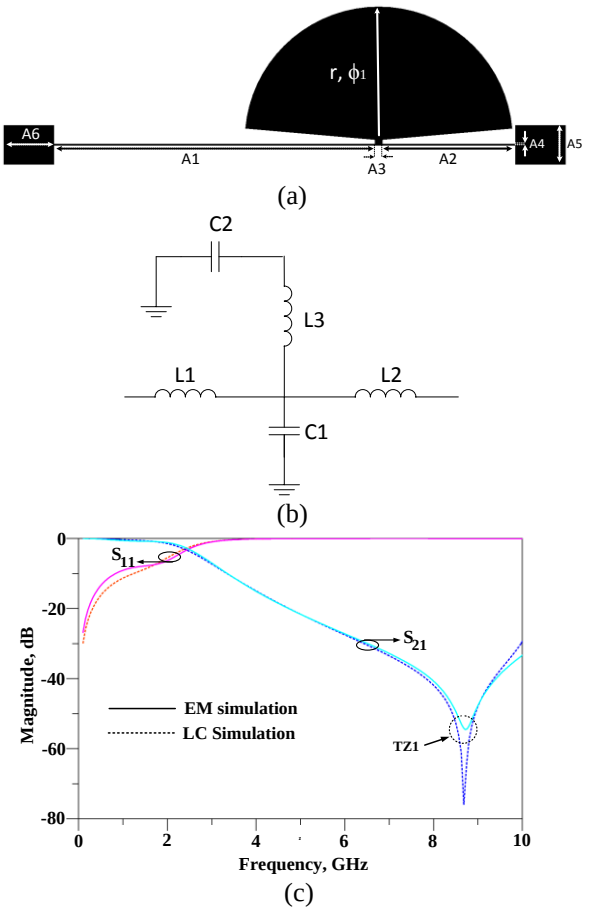

Fig. 1. (a) Layout, (b) L-C equivalent circuit, and (c) EM and L-C simulations of primitive semi-circle resonator.

In order to have a focus on computational theory, the applied resonators are modeled using LC equivalent circuits. To find accurate using LC equivalent circuits, applied microstrip discontinuities and components that are encountered in the proposed filter designs are described in Fig. 2. In the layout of proposed filter steps, open-ends, high-impedance short-line element and low-impedance short-line element are used, which these components and LC equivalent circuits are shown in Fig. 2. For a symmetrical step, the capacitance and inductances of the equivalent circuit indicated in Fig. 2 (a). At the open end of a microstrip line the fields do not stop abruptly but extend slightly further due to the effect of the fringing field. This effect can be modeled either with an equivalent shunt capacitance as shown in Fig. 2 (b). In Fig. 2 (c), a short length of high-impedance line terminated at both ends by low impedance is represented by a π-equivalent circuit. For the dual case shown in Fig. 2 (d), a short length of low-impedance line terminated at either end by high impedance is represented by a T-equivalent circuit.

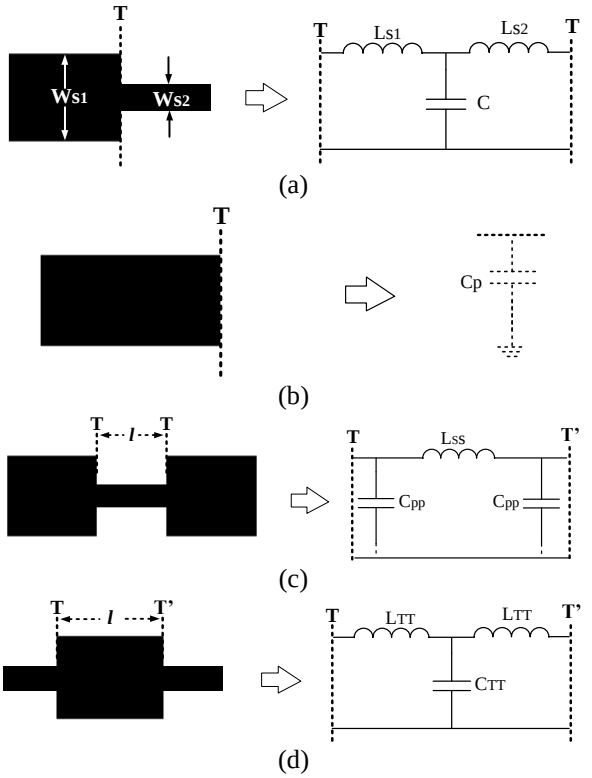

Fig. 2. Microstrip discontinuities: (a) step, (b) open-end, (c) high-impedance short-line, and (d) low-impedance short-line elements and their equivalent circuits [2].

The ABCD-parameters for a two-port network are [1]:

$$\begin{bmatrix} V_1 \\ I_1 \end{bmatrix} = \begin{bmatrix} A & B \\ C & D \end{bmatrix} \begin{bmatrix} V_2 \\ I_2 \end{bmatrix}. \quad (1)$$

According to (1), the ABCD-parameters of L-C equivalent circuit for primitive semi-circle resonator are obtained as follows:

$$A = C_1L_1S^2 + \frac{C_2L_1S^2}{C_2L_3S^2+1} + 1, \quad (2)$$

$$B = L_1S + C_1L_1L_2S^3 + \frac{C_2L_1L_2S^3}{C_2L_3S^2+1} + L_2S\ ), \quad (3)$$

$$C = C_1S + \frac{C_2S}{C_2L_3S^2+1}, \quad (4)$$

$$D = C_1L_2S^2 + \frac{C_2L_2S^2}{C_2L_3S^2+1} + 1. \quad (5)$$

The S-parameter (S_{21}) in terms of ABCD-parameters is [1]:

$$S_{21} = \frac{2}{A+B/Z_0+CZ_0+D}. \quad (6)$$

From (6), S_{21} of L-C equivalent circuit is:

$$S_{21} = \big(2Z_0(C_2L_3S^2+1)\big)/(S^5(C_1L_1C_2L_2L_3) + S^4(C_1L_1C_2L_3Z_0 + C_1L_2C_2L_3Z_0) + S^3\big(C_1L_3C_2{Z_0}^2 + C_2L_1L_3 + C_1L_1L_2 + C_2L_3L_2\big) + S^2(C_1L_1Z_0 + C_1L_2Z_0 + C_2L_2Z_0 + C_2L_1Z_0 + 2C_2L_3Z_0) + S\big(C_1{Z_0}^2 + C_2{Z_0}^2 + L_1 + L_2\big) + 2Z_0 + 1). \quad (7)$$

The T_{Z1} is obtained using Equation (7):

$$F_{z1} = \frac{1}{2\pi\sqrt{C_2L_3}}. \quad (8)$$

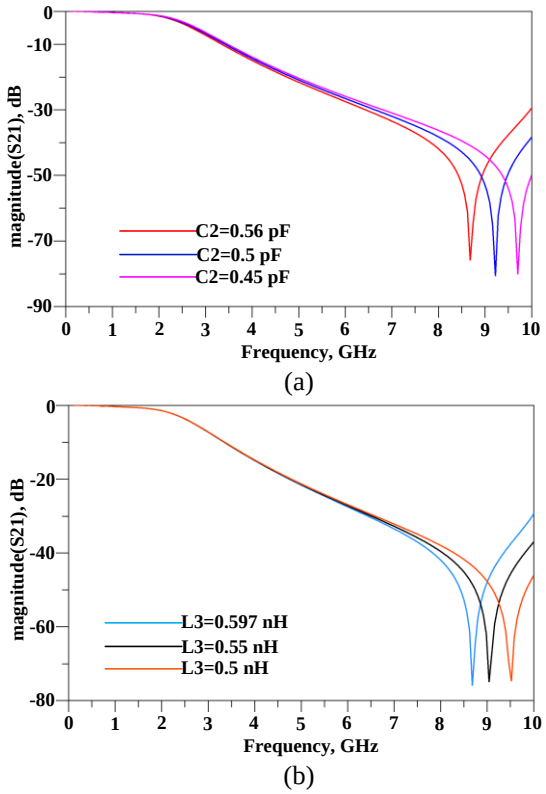

Fig. 3. (a) Variations of Fz1 as a function of C2, and (b) variations of Fz1 as a function of L3.

According to (8), the location of T_{Z1} is a function of C_2 and L_3. According to Fig. 3 (a) and Table 1, decreasing in value of C_2 (when L_3 is unchanged) moves T_{Z1} to the higher frequencies and vice versa. Also, decreasing in value of L_3 (when C_2 is unchanged) moves T_{Z1} to the higher frequencies and vice versa, as shown in Fig. 3 (b). So, the values of L-C equivalent circuit in Table 1 is selected, to achieve a transmission-zero at the desired frequency.

B. Symmetrical semi-circle resonator

To achieve a wide stop-band and better performance, symmetrical semi-circle resonator is designed. The substrate and conductor material are same as mentioned below. The layout of the symmetrical semi-circle resonator is depicted in Fig. 4 (a). According to Fig. 4 (b), this resonator with simple structure can generate a wide stop-band (from 3.9 to 22 GHz with -20 dB attenuation level). Although the transition-band is not very sharp. The proposed structure creates a transmission-zero (T_{Z2}) at 13.8 GHz with -47 dB attenuation, as seen in Fig. 4 (b).

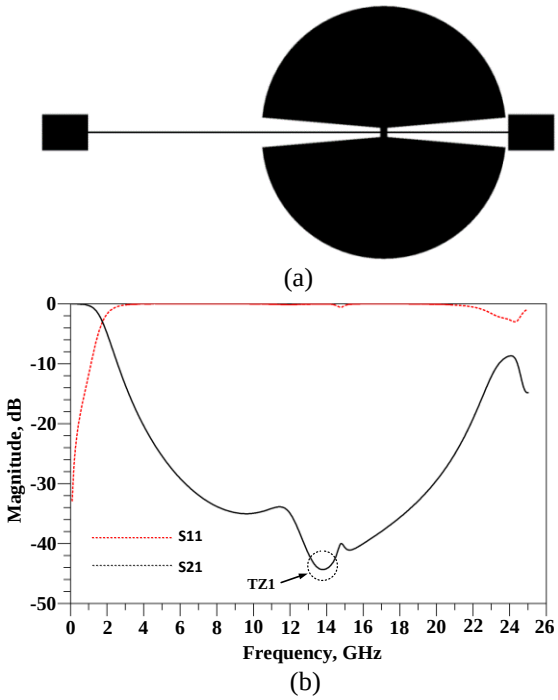

Fig. 4. (a) Layout and (b) EM simulation results of symmetrical semi-circle resonator.

C. Butterfly resonator

To achieve a sharp transition-band, a butterfly resonator is proposed. The layout and L-C equivalent circuit of butterfly resonator are demonstrated in Fig. 5 (a) and 5 (b), respectively. According to Fig. 5 (b), the corresponding inductances and capacitance of transmission line are L_4, L_5 and C_3, respectively. L_6 and L_7 are the inductances of high-impedance line and low impedance stub, respectively. C_4 is the sum of open stub and low-impedance stub capacitances. According to Fig.

5 (c), the EM simulations and L-C equivalent circuit simulation results are in good agreement. Also there is a transmission-zero (T_{Z3}) at 2.4 GHz with -52 dB attenuation level as seen in Fig. 5 (c). The L-C equivalent circuit values are optimized by ADS software and they are summarized in Table 2. The dimensions of this resonator are: A_7=10.45, A_8=3.07, A_9=5.5, A_{10}=0.4, A_{11}=3.92, A_{12}=0.15 (unit: millimeter) and ϕ_2=90°. The substrate and conductor material are same as mentioned below.

Table 2: The optimized values of L-C equivalent circuit

Parameter	L_4	L_5	L_6	L_7	C_3	C_4
Values	3.24	7.415	2.364	0.66	0.422	0.819

(Units: C=[pF]; L=[nH]).

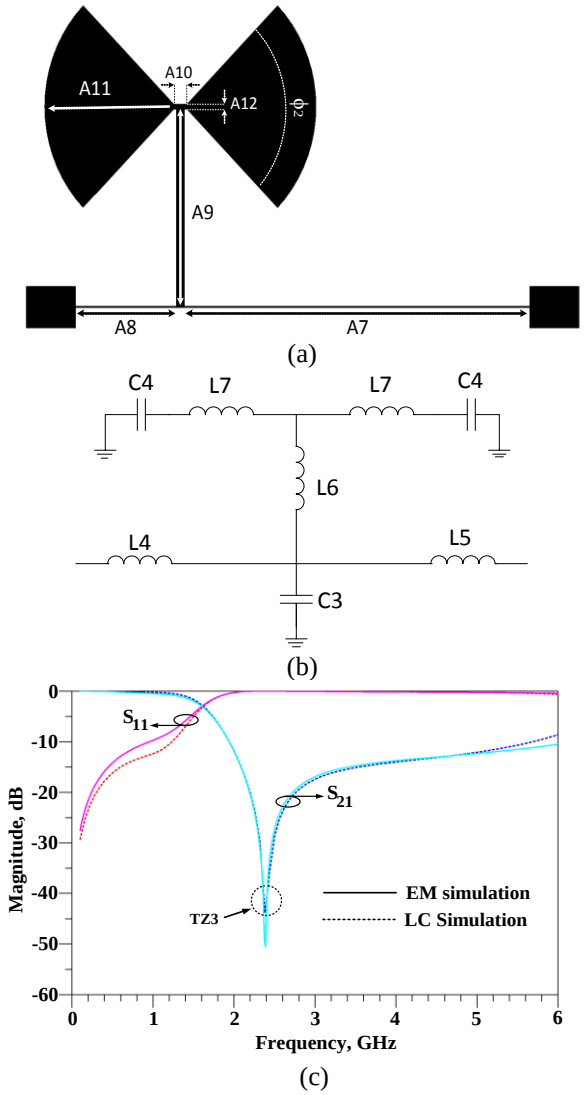

Fig. 5. (a) Layout, (b) L-C equivalent circuit, and (c) EM and L-C simulations of butterfly resonator.

As the simulation results shown in the Fig. 5 (c), the butterfly resonator has good performance. The insertion loss in pass band is zero (S_{12}= S_{21}= 0 dB). In the stop band this resonator creates a strong transmission-zero (T_{Z3}) near the desired cut-frequency of the proposed LPF, which results in a good performance compare to the primitive resonator. Unfortunately, the input and output return losses (S_{11}, S_{22}) of butterfly resonator in pass band are not so good and the transition band is not so sharp, therefore to improve the performance symmetrical semi-circle resonator and butterfly resonator are combined together, which will be discussed in Section II.D

The ABCD-parameters of L-C equivalent circuit for butterfly resonator are as follows:

$$A = C_3L_4S^2 + \frac{2C_4L_4S^2}{(2C_4L_6+C_4L_7)S^2+1} + 1, \quad (9)$$

$$B = L_4S + C_3L_4L_5S^3 + \frac{2C_4L_4L_5S^3}{(2C_4L_6+C_4L_7)S^2+1} + L_5S, \quad (10)$$

$$C = C_3S + \frac{2C_4S}{(2C_4L_6+C_4L_7)S^2+1}, \quad (11)$$

$$D = C_3L_5S^2 + \frac{2C_4L_5S^2}{(2C_4L_6+C_4L_7)S^2+1} + 1. \quad (12)$$

From (6), S_{21} of L-C equivalent circuit for butterfly resonator is:

$$S_{21} = \frac{\left(2Z_0\left((2C_4L_6+C_4L_7)S^2+1\right)\right)}{(S^5(2C_4L_6L_5C_3L_4+L_5C_3C_4L_4L_7)} + S^4(2Z_0C_4L_6C_3L_4 + Z_0C_3L_4C_4L_7 + 2Z_0L_5C_3C_4L_6 + Z_0L_5C_3C_4L_7) + S^3\left(2{Z_0}^2C_3C_4L_6 + {Z_0}^2C_3C_4L_7 + 2L_4C_4L_6 + L_4C_4L_7 + L_5C_3L_4 + 2L_5C_4L_6 + L_5C_4L_7\right) + S^2(C_3L_5Z_0 + 2C_4L_5Z_0 + 2Z_0C_4L_4 + 4Z_0C_4L_6 + 2Z_0C_4L_7 + Z_0C_3L_4) + S\left(C_3{Z_0}^2 + 2C_4{Z_0}^2 + L_4 + L_5\right) + 2Z_0 + 1). \quad (13)$$

The T_{Z3} is obtained using Equation (13):

$$F_{z3} = \frac{1}{2\pi\sqrt{(2C_4L_6+C_4L_7)}}. \quad (14)$$

According to (14), the location of T_{Z3} is a function of L_6 and C_4, which L_6 and C_4 are inductance and capacitance of A_9 and A_{11} in Fig. 5 (a), respectively. Decreasing in the value of A_9 (when A_{11} is unchanged) and decreasing in the value of A_{11} (when A_9 is unchanged), moves T_{Z3} to the higher frequencies, as depicted in Fig. 6 (a) and 5 (b), respectively. So to have sharp transition-band, T_{Z3} is tuned at 2.4 GHz and values of L-C equivalent circuit are obtained in Table 2.

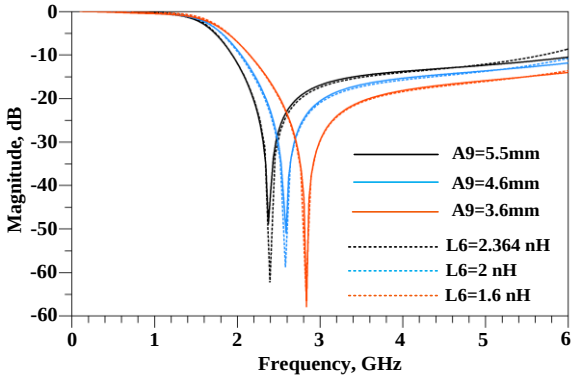

(a)

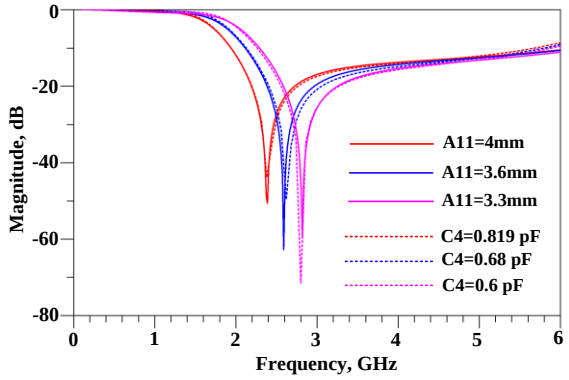

(b)

Fig. 6. (a) Variations of Fz_3 as a function of L_6 and A_9, and (b) variations of Fz_3 as a function of C_4 and A_{11}.

D. Primitive LPF

To approach a wide stop-band and sharp transition-band, symmetrical semi-circle resonator and butterfly resonator are combined, with same substrate and conductor strip line material as mentioned below, based on Fig. 7 (a). Although this structure, suffers from high ripple in pass-band and low return-loss in pass-band and a transmission pole that limits the suppression level and stopband bandwidth of primitive low pass filter, as seen in Fig. 7 (b). The distance between the resonators is A_{13}=6.26 mm.

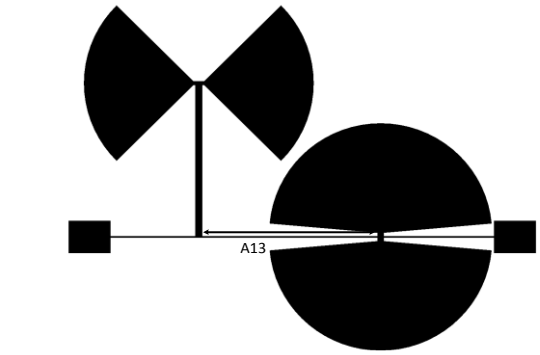

(a)

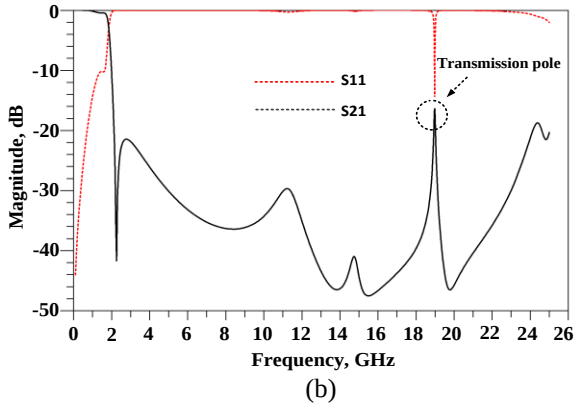

(b)

Fig. 7. (a) Layout and (b) EM simulations of primitive LPF.

E. Proposed LPF

According to Fig. 7 (b), there is a transmission-pole at 19 GHz, which limits the stop-band of primitive LPF. Therefore, two suppressing cells, with same substrate and conductor material as mentioned below, are added to primitive LPF to extend the stop-band and the transmission line is bended without increasing dimension as depicted in Fig. 8 (a). EM simulations illustrate wide stop-band, sharp transition-band. Moreover, the ripple in pass-band has been reduced (less than 0.05 dB) and a good return-loss in pass-band (20 dB) is achieved, as seen in Fig. 8 (b). Physical dimensions of the proposed LPF are: L_1=4.33, L_2=3.96, L_3=1.8, L_4=1, L_5=1.5, L_6=1.17, L_7=3.07, L_8=0.96, L_9=1.22, L_{10}=0.97, L_{11}=5.5, L_{12}=0.8, D_1=0.4, D_2=0.15, D_3=0.23, D_4=0.05, D_5=0.3, D_6=0.1, R_1=0.5, R_2=3.92 and R_3=4.12 (all in millimeters). Also θ_1=90˚, θ_2=170˚.

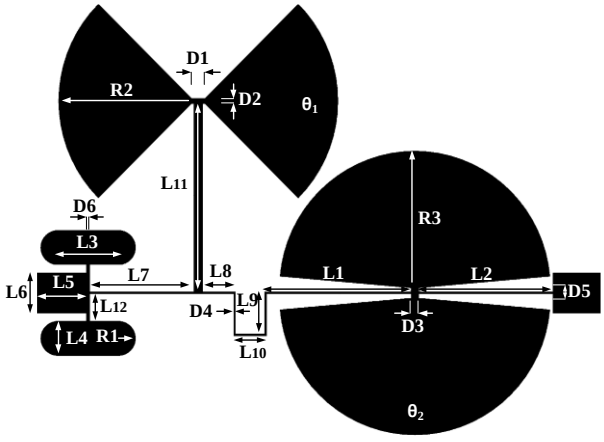

(a)

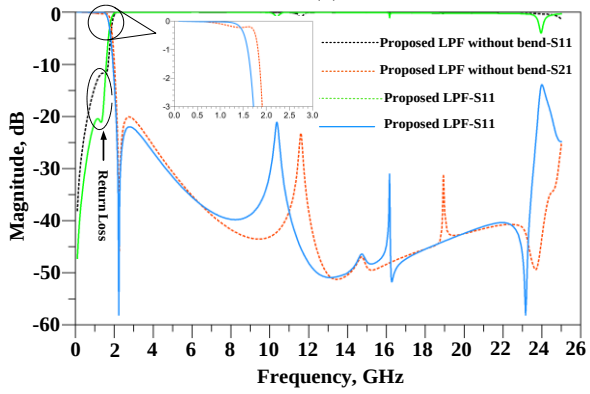

(b)

Fig. 8. (a) Layout and (b) EM simulations of proposed LPF.

III. MEASURED AND SIMULATED RESULTS

The proposed low-pass filter has been designed and fabricated on the RT-Duorid 5880 substrate with relative permittivity of 2.2, thickness of 0.381 mm and loss-tangent of 0.0009 Also, copper with thickness of 10μm

is utilized as conductor strip lines. The photograph of fabricated low-pass filter is illustrated in Fig. 9 (a). There is a good agreement between measurement and simulation results, as demonstrated in Fig. 9 (b). The S-parameters are measured using the network analyzer N5230A and. The results demonstrate that, proposed LPF presents very good size reduction compared with previous works.The final circuit dimensions of the proposed low-pass filter are only 13.72 × 12.6 mm^2 ($0.11\lambda_g \times 0.1\lambda_g$). The proposed LPF indicates high suppression in a wide stop-band from 2.1 to 23.73 GHz with more than -20 dB attenuation level (measurement results), which suppresses the 2nd-14th harmonics. The performance comparison among published filters and proposed one have been illustrated in Table 3.

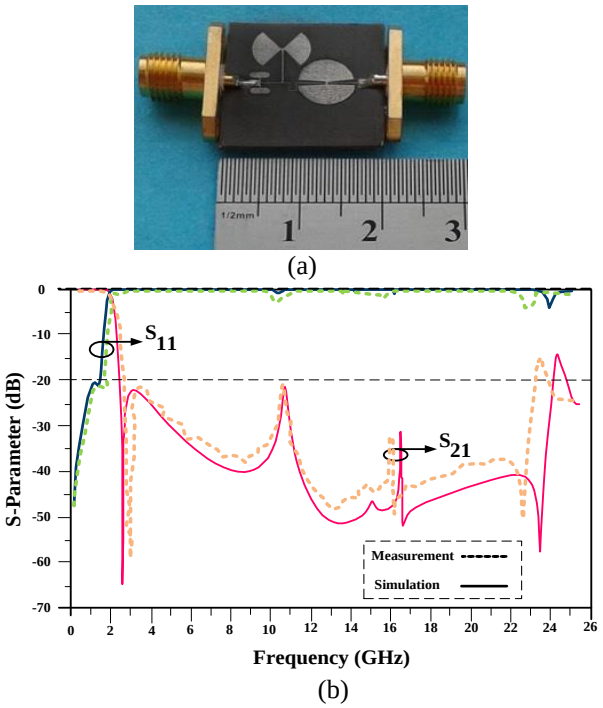

Fig. 9. (a) Photograph of proposed LPF, and (b) EM simulations and measured results

Table 3: Performance comparison among previous filters and proposed one

Refs.	ξ	RSB	SF	NCS	AF	FOM
[3]	95.5	1.359	2	0.540×0.480	2	500.7
[6]	52.8	1.529	2	0.081×0.113	1	17640
[7]	43.9	1.636	1	0.101×0.150	1	4723
[8]	95	1.4	2	0.022	1	12090
[13]	-	1.58	1.5	0.090×0.110	1	-
[14]	78	1.7	2	0.160×0.100	2	8287.5
[16]	129	1.62	2	0.730×0.130	1	4430.8
This work	112	1.674	2	0.110×0.100	1	34088

In Table 3, the sharpness of transition-band (ξ) is:

$$\xi = \frac{\alpha_{max} - \alpha_{min}}{f_s - f_c} \quad (dB/GHz), \tag{15}$$

and α_{max} is -60 dB suppression level; α_{min} is -3 dB suppression level; f_C is the frequency corresponds with -60 dB suppression level and f_c is the corresponding frequency with -3 dB suppression level. The relative stop-band band-width (RSB) is given by:

$$RSB = \frac{stopband\ bandwidth}{stopband\ center\ frequency}. \tag{16}$$

The suppressing factor (SF) is:

$$SF = \frac{suppression\ level}{10}. \tag{17}$$

The normalized circuit size (NCS) is:

$$NCS = \frac{physical\ size\ (length \times width)}{\lambda_g^2}. \tag{18}$$

The λ_g is the length of guided wavelength at -3 dB cut off frequency and for calculation of architecture facture, this parameter has below values: for circuits with 1 dimension is defined 1 and for circuits with three dimension the AF is defined 2.

Finally, the figure of merit (FOM) is defined as:

$$FOM = \frac{RSB \times \xi \times SF}{AF \times NCS}. \tag{19}$$

IV. CONCLUSION

A miniaturized low-pass filter with high FOM and ultra-wide stop-band is proposed. The proposed filter demonstrates very good performance such as low insertion-loss in pass-band, wide stop-band, sharp transition-band and small dimension. The final circuit dimension is only $0.11\lambda g \times 0.1\lambda g$. The cut off frequency of the proposed LPF is 1.75 GHz. The proposed structure suppresses 2nd to 14th harmonics with more than 20 dB attention level. With the above desirable features, the proposed filter is suitable for L-band applications.

ACKNOWLEDGMENT

The authors would like to thank the Kermanshah Branch, Islamic Azad University for the financial support of this research project.

REFERENCES

[1] D. M. Pozar, *Microwave Engineering*. John Wiley & Sons, New York, 2005.

[2] J. S. Hong and M. J. Lancaster, *Microstrip Filters for RF/Microwave Applications*. John Wiley & Sons, New York, 2001.

[3] Y. Zhang, L. Jin, and L. Li, "Design of LPF using Hi-Lo interdigital DGS slot," *IEICE Electronics Express*, vol. 13, no. 9, pp. 1-6, 2016.

[4] L. Li, Z. F. Li, and J. F. Mao, "Compact lowpass filters with sharp and expanded stopband using stepped impedance hairpin units," *IEEE Microwave and Wireless Components Letters*, vol. 20, no. 6, pp. 310-312, 2010.

[5] J. P. Wang, L. Ge, Y. X. Guo, and W. Wu,

"Miniaturised microstrip lowpass filter with broad stopband and sharp roll-off," *Electronics Letters*, vol. 46, no. 8, pp. 573-575, 2010.

[6] L. Shuai, J. Xu, and Z. Xu, "Compact lowpass filter with wide stopband using stepped impedance hairpin units," *Electronics Letters*, vol. 51, no. 1, pp. 67-69, 2014.

[7] F. Wei, L. Chen, and X. W. Shi, "Compact lowpass filter based on coupled-line hairpin unit," *Electronics Letters*, vol. 48, no. 7, pp. 379-381, 2012.

[8] V. Velidi and S. Sanyal, "Sharp roll-off lowpass filter with wide stopband using stub-loaded coupled-line hairpin unit," *IEEE Microwave and Wireless Components Letters*, vol. 21, no. 6, pp. 301-303, 2011.

[9] F. Wei, L. Chen, X. W. Shi, Q. L. Huang, and X. H. Wang, "Compact lowpass filter with wide stop-band using coupled-line hairpin unit," *Electronics Letters*, vol. 46, no. 1, pp. 88-90, 2010.

[10] X. B. Wei, P. Wang, M. Q. Liu, and Y. Shi, "Compact wide-stopband lowpass filter using stepped impedance hairpin resonator with radial stubs," *Electronics Letters*, vol. 47, no. 15, pp. 862-863, 2011.

[11] M. Rezaei Khezelia, M. Hayati, and A. Lotfi, "Compact wide stopband lowpass filter using spiral loaded tapered compact microstrip resonator cell," *International Journal of Electronics*, vol. 101, no. 3, pp. 375-382, 2012.

[12] C. J. Chen, "Design of artificial transmission line and low-pass filter based on aperiodic stubs on a microstrip line," *IEEE Transaction on Components, Packing and Manufacturing Technology*, vol. 4, no. 5, pp. 922-928, 2014.

[13] Q. Li, Y. Zhang, and Y. Fan, "Compact ultra-wide stopband low pass filter using multimode resonators," *Electronics Letters*, vol. 51, no. 14, pp. 1084-1085, 2015.

[14] F. C. Chen, H. T. Hu, J. M. Qiu, and Q. X. Chu, "High-selectivity low-pass filters with ultrawide stopband based on defected ground structures," *IEEE Transaction on Components, Packing and Manufacturing Technology*, vol. 5, no. 9, pp. 1313-1319, 2015.

[15] A. K. Verma, N. P. Chaudhari, and A. Kumar, "High performance microstrip transverse resonance lowpass filter," *Microwave and Optical Technology Letters*, vol. 55, no. 5, pp. 1149-1152, 2013.

[16] P. Zhang, M. Li, and J. Wang, "Miniaturized lowpass filter with ultra-wide stopband using dual-plan defected structures," *IEICE Electronics Express*, vol. 12, no. 2, pp. 1-7, 2014.

Saeed Roshani received the B.Sc. degree in Electrical Engineering from Razi University, Kermanshah, Iran in 2008, M.Sc. degree in Electrical Engineering from Shahed University, Tehran, Iran in 2011 and Ph.D. in Electrical Engineering from Razi University in 2015. He performed opportunity research program in Amirkabir University of Technology (Tehran Polytechnics) Iran, in 2014-2015. He graduated as the Best Student of his country among all students of Iran in 2015 and awarded by the First Vice President and Science, Research & Technology Minister. He is currently an Assistant Professor in the Department of Electrical Engineering at Islamic Azad University, Kermanshah, Iran. He has published more than 40 papers in ISI Journals and Conferences and two books. His research interest includes the microwave and millimeter wave devices and circuits, low-power and low-size integrated circuit design.

Alireza Golestanifar was born in Kermanshah, Iran in 1993. He received his B.Sc. degree in Electronics Engineering in 2015 from Islamic Azad University, Kermanshah, Iran and he is now pursuing his M.Sc. degree from Islamic Azad University, Kermanshah, Iran. His current research includes microwave passive circuits and RF integrated circuit design.

Amirhossein Ghaderi was born in Kermanshah, Iran in 1992. He received his B.Sc. degree in Electronics Engineering in 2015 from Islamic Azad University, Kermanshah, Iran (Honor) and he is currently working towards the M.Sc. degree in Electronics Engineering from Islamic Azad University, Kermanshah, Iran. He was selected as the Best Student in the Electronics Engineering Department

and awarded by the University President of Islamic Azad University, Kermanshah, Iran in 2014. His current research includes microwave passive circuits and RF integrated circuit design.

Sobhan Roshani received the B.Sc. degree in Electrical Engineering from Razi University, Kermanshah, Iran in 2010, M.Sc. degree in Electrical Engineering from Iran University of Science & Technology-IUST, Tehran, Iran in 2012 and Ph.D. in Electrical Engineering from Razi University in 2016. His research interest includes switching power amplifiers, microwave circuits, image processing, optimization and neural networks. He is currently working with Department of Electrical Engineering at Islamic Azad University, Kermanshah, Iran.

Shielding Effectiveness Estimation of a Metallic Enclosure with an Off-center Aperture for Obliquely Incident and Arbitrary Polarized Plane Wave

Dan Shi, Na Lv, and Yougang Gao

Department of Electronic Engineering
Beijing University of Posts and Telecommunications, Beijing, 100000, China
shidan@buptemc.com

Abstract ─ A circuit model for the shielding effectiveness (SE) estimation of a metallic enclosure is proposed, whose off-center aperture is irradiated by the obliquely incident and arbitrary polarized plane wave. This new model has advantages in the following aspects. First, it can deal with the arbitrary angular and polarized incident wave other than the normal incident wave. The incident wave angle and polarization direction are considered in the proposed analytical formulas. Second, higher-order modes such as TEmn and TMmn are included to enable the model to be applicable in higher frequencies. Third, the impedance of the enclosure wall is considered rather than the perfect conductor assumption used in the published literatures, which removes the deficiency that the aperture impedance is zero when the length of the aperture is equal to an integral number of the wavelengths. The influences on the SE from different parameters such as the incident wave angle, the polarization direction as well as the enclosure wall thickness are investigated. Finally, the accuracy of the proposed model is validated by measurements, simulations and comparisons with other literatures. The proposed method is particularly useful for the shielding enclosure design in the electronic manufacturing industry.

Index Terms ─ Circuit model, higher-order modes, obliquely incident, rectangular enclosure, shielding effectiveness.

I. INTRODUCTION

The shielding enclosure has been widely used in the electronic system to reduce the emissions or improve the immunity. The performance of a shielding enclosure is assessed by its shielding effectiveness (SE), defined as the ratio of field strengths in the presence and absence of the enclosure. However, the SE is often deteriorated by the apertures or slots for the input and output connections, heat dissipation, control and ventilation. Thus, in the published literatures, numerous approaches have been presented for calculating the SE of the shielding enclosures with apertures and slots, mainly including numerical methods and analytical formulations. The numerical methods such as the transmission-line modeling method [1], the finite-difference time-domain method [2], the method of moments [3], [4], the finite element method [5], and the hybrid methods [6] can model and calculate the complex structures, but it is difficult for designers to use them to investigate the effect of various parameters. In addition, they are computationally intensive when the thickness of the enclosure wall is much smaller than the enclosure dimension size. Meanwhile, most analytical formulations are based on the equivalent circuit method proposed by Robinson [7], where the aperture and the enclosure are assumed to be the length of a coplanar strip transmission line, and a rectangular waveguide ended with a short circuit. The model is limited to the center aperture and the TE10 mode. The method was extended in [8] to include the effects of loading the enclosure with some printed circuit board structures. The enclosure with apertures on multiple sides considering the oblique incidence and polarization was studied in [9]. [10] applied the concept of quasi-stationary admittance of diaphragms inside a rectangular waveguide and their equivalent circuits to investigate the SE of an enclosure with an aperture. The SE of the rectangular enclosure with an off-center aperture was analyzed in [11]. However, some important design parameters, such as the incident wave angle and polarization direction, have not been thoroughly investigated in the published literatures.

In this paper, a more general approach is proposed to evaluate the SE of a rectangular enclosure with an off-center aperture. The incident wave angle and the polarization direction are included in the analytical formulation. The proposed method can handle an arbitrary locational aperture in the higher frequencies. Moreover, the thickness of the enclosure wall is considered, which removes the limitation that the SE is erroneously predicted to be infinite when the length of the aperture corresponds to an integer multiple of wavelength for the traditional circuit models.

Submitted On: August 17, 2016
Accepted On: January 28, 2017

II. PROPOSED MODEL AND FORMULATION

The geometry of the enclosure with an aperture is shown in Fig. 1. The thickness of the enclosure wall is *t*. A plane wave as an excitation source has its incident angle θ and polarization angle φ.

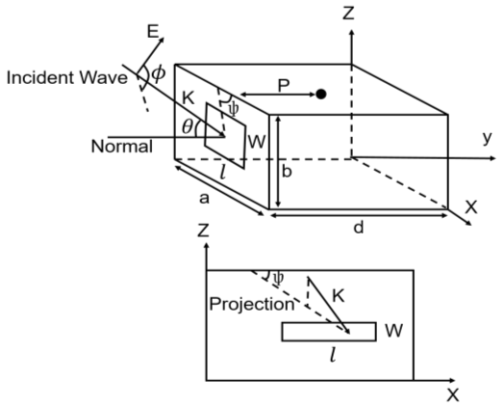

Fig. 1. The obliquely incident wave and the enclosure with an aperture.

Figure 2 shows the obliquely incident wave in the front face. The electric field ***E*** is decomposed into the x-component, the y-component and the z-component fields by the vector analysis. The normal vector of the front face of the enclosure is **n**, same as the direction of the y-axis. The propagation vector of the incident wave is named as **k** vector. The incident angle θ is defined as the angle between the propagation vector **k** and the normal vector **n**, and these two vectors determine the incident plane. The angle between the ***E*** field and the incident plane is defined as the polarization angle φ. The angle between the projection of the propagation vector **k** in the X-Z plane and the x-axis is defined as ψ. The decompositions of the ***E*** field are as follows:

x-component: $-E\cos\varphi\cos\theta\cos\psi + E\sin\varphi\sin\psi$,

y-component: $E\cos\varphi\sin\theta$,

z-component: $-E\cos\varphi\cos\theta\sin\psi - E\sin\varphi\cos\psi$.

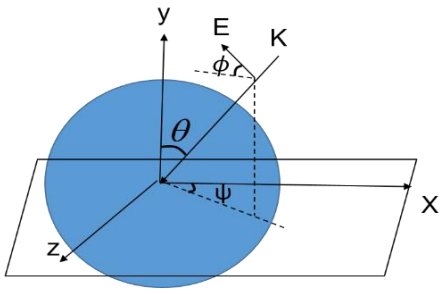

Fig. 2. The vector analysis of an obliquely incident wave.

For the x-component and the z-component of the electric field ***E***, the wave propagates along the y-axis into the enclosure. However, for the y-component, the wave propagates along the z-axis and reflects back and forth, which has small contributions to the field in the enclosure and is ignored in the calculation.

For the z-component, the equivalent circuit model is shown as Fig. 3.

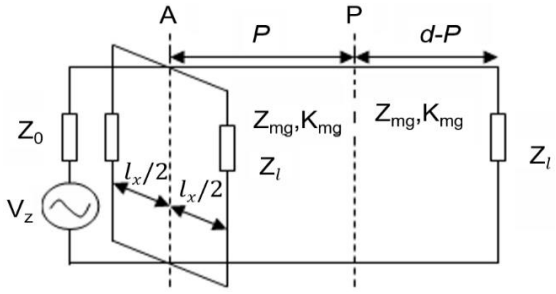

Fig. 3. The equivalent circuit of an enclosure with an aperture.

The aperture is represented as a coplanar strip transmission line with the length of the aperture in the x-direction. Owing to the loss of the enclosure wall, the transmission line is loaded with the impedance Z_l at each end. Based on Gupta's theory [12], the characteristic impedance of the transmission line is:

$$Z_{os1} = 120\pi^2 \left[\ln\left(2\frac{1+\sqrt[4]{1-\left(w_{e1}/b\right)^2}}{1-\sqrt[4]{1-\left(w_{e1}/b\right)^2}} \right) \right]^{-1}. \quad (1)$$

The effective width w_{e1} is:

$$w_{e1} = w - \frac{5t}{4\pi}\left(1+\ln\frac{4\pi w}{t}\right), \quad (2)$$

where *t* is the thickness of the enclosure wall and *w* is the width of the aperture in the z-direction.

A coupling co-efficient C_m, obtained by enforcing the field continuity at the aperture such that the total modal fields at the aperture are consistent with the aperture field, is introduced to account for the coupling between the aperture and the enclosure:

$$C_m = \int_{x_0}^{x_0+l}\int_{z_0}^{z_0+w} \cos\left(\frac{n\pi z}{b}\right)\cos\left(\frac{n\left(z-z_0\right)\pi}{w}\right)\sin\left(\frac{\pi m x}{a}\right)\sin\left(\frac{m\pi\left(x-x_0\right)}{l}\right)dxdz \Big/ XZ, \quad (3)$$

where x_0 and z_0 are the coordinates of the first edge of the aperture, *X* and *Z* are the coordinates of the aperture center. The load impedance Z_l at the ends of the transmission line is transformed through a distance *l*/2 to the center to calculate the aperture impedance Z_{ap1}:

$$Z_{ap1} = \frac{1}{2}C_m Z_{os1}\frac{Z_l + jZ_{os1}\tan\left(k_0 l/2\right)}{Z_{os1} + jZ_l\tan\left(k_0 l/2\right)}, \quad (4)$$

where $Z_l = (1+j)\sqrt{\pi f \mu_1/\sigma}$, μ_1 and σ are the permeability and conductivity of the enclosure.

By Thevenin's theorem, the equivalent source voltage V_{1z} and source impedance Z_{1z} are determined by:

$$V_{1z} = V_z Z_{ap1} / (Z_0 + Z_{ap1}), \quad (5)$$

$$Z_{1z} = Z_0 Z_{ap1} / \left(Z_0 + Z_{ap1}\right), \quad (6)$$

where source voltage V_z is $-V_0\left(\cos\phi\cos\theta\sin\psi + \sin\phi\cos\psi\right)$.

The equivalent voltage V_{2z} and the source impedance Z_{2z} are obtained by transforming V_{1z} and Z_{1z} to the test point P:

$$V_{2z} = V_{1z} / (\cos(k_{mg} p) + j(Z_{1z} / Z_{mg})\sin(k_{mg} p)), \quad (7)$$

$$Z_{2z} = Z_{mg} \frac{Z_{1z} + jZ_{mg}\tan(k_{mg} p)}{Z_{mg} + jZ_{1z}\tan(k_{mg} p)}. \quad (8)$$

For the TE_{mn} propagation mode, the waveguide modal impedance and the propagation constant are:

$$Z_{mg} = Z \Big/ \sqrt{1-\left(m\lambda/2a\right)^2 - \left(n\lambda/2b\right)^2}, \quad (9)$$

$$k_{mg} = k\sqrt{1-\left(m\lambda/2a\right)^2 - \left(n\lambda/2b\right)^2}. \quad (10)$$

For the TM_{mn} propagation mode, the waveguide modal impedance and the propagation constant are:

$$Z_{mg} = Z\sqrt{1-\left(m\lambda/2a\right)^2 - \left(n\lambda/2b\right)^2}, \quad (11)$$

$$k_{mg} = k\sqrt{1-\left(m\lambda/2a\right)^2 - \left(n\lambda/2b\right)^2}, \quad (12)$$

where $k = 2\pi/\lambda, Z = \sqrt{\mu/\varepsilon}$, μ and ε are the permeability and the dielectric permittivity of the material in the enclosure, and m and n are the modes of TE and TM wave.

Transform the load impedance Z_l at the end of the waveguide to the test point P, and the load impedance Z_3 is represented as:

$$Z_3 = Z_{mg} \frac{Z_l + jZ_{mg}\tan k_{mg}(d-p)}{Z_{mg} + jZ_l \tan k_{mg}(d-p)}. \quad (13)$$

Accordingly, the voltage at the test point is equal to $V_{pm1} = V_{2z}Z_3 \big/ \left(Z_{2z} + Z_3\right)$. For the multi-modes in the enclosure, the total voltage at the test point is given by:

$$V_{tpml} = \sum V_{pm1}. \quad (14)$$

For the x-component of the ***E*** field, the equivalent circuit model is similar to Fig. 3, simply replacing the source voltage V_z and coplanar transmission line l with V_x and w respectively. The source voltage V_x is equal to $V_0\left(\sin\phi\sin\psi - \cos\phi\cos\theta\cos\psi\right)$.

The characteristic impedance of the coplanar transmission line is:

$$Z_{os2} = 120\pi^2\left[\ln\left(2\left(1+\sqrt[4]{1-\left(w_{e2}/a\right)^2}\right)/\left(1-\sqrt[4]{1-\left(w_{e2}/a\right)^2}\right)\right)\right]. \quad (15)$$

The effective width w_{e2} is:

$$w_{e2} = l - \frac{5t}{4\pi}\left(1+\ln\frac{4\pi l}{t}\right). \quad (16)$$

The aperture impedance Z_{ap2} can be calculated by transforming the load impedance Z_l at the ends of the aperture through a distance $w/2$ to the center:

$$Z_{ap2} = \frac{1}{2}C_m Z_{os2}\frac{Z_l + jZ_{os2}\tan\left(k_0 w/2\right)}{Z_{os2} + jZ_l\tan\left(k_0 w/2\right)}. \quad (17)$$

Similarly, the voltage V_{pm2} at the test point P from the effect of the x-component of the ***E*** field can be obtained by replacing the source voltage V_z and the aperture impedance Z_{ap1} with V_x and Z_{ap2} from (5)-(14). The total voltage at the test point for the multi-modes is:

$$V_{tpm2} = \sum V_{pm2}. \quad (18)$$

Finally, the total voltages at the observing point P is given by the combination of the contributions from the x-component and z-component:

$$V_{ptotal} = \sqrt{V_{tpm1}^2 + V_{tpm2}^2}. \quad (19)$$

In the absence of the enclosure, the load impedance at P is simply Z_0 and the voltage V_p is equal to $V_0/2$. Therefore, the electric shielding effectiveness is written as:

$$S_E = 20\log_{10}\left|V_p / V_{ptotal}\right| = 20\log_{10}\left|V_0 / 2V_{ptotal}\right|. \quad (20)$$

III. NUMERICAL RESLULTS AND MEASUREMENT

The enclosure for testing is with the dimensions of 30 cm × 40 cm × 20 cm, and an aperture with the dimensions of 5 cm × 1cm is located at the off-center position in the front face. The enclosure is filled with air. The coordinates of the aperture center are X = 14.5 cm and Z = 10 cm. As the operating frequency of the electronic equipment gets higher and higher, many higher modes propagate in the enclosure other than only the dominant mode. The cut-off frequency of each mode is listed in the Table 1 according to (21). Thus, the modes TE_{10}, TE_{01}, TE_{20}, TE_{02}, TE_{11}, TE_{12}, TE_{21}, TE_{22}, TM_{11}, TM_{21}, and TM_{12} should be considered if the operating frequency is between the frequency band 1 GHz ~ 1.26 GHz.

$$f_c = \sqrt{\left(m/a\right)^2 + \left(n/b\right)^2}/2\sqrt{\mu\varepsilon}, , \quad (21)$$

where m and n are the modes of TE and TM wave.

Table 1: Cut-off frequency (MHz) for modes in the enclosure

n \ m	0	1	2
0	-	500	1000
1	375	625	1070
2	750	900	1250

According to the cut-off frequencies of different modes and the incident wave frequency, the modes considered in the analytical formulas are determined. Thus, the SE of the enclosure with an aperture can be

calculated with the proposed formulas. To validate the results, some measurements were carried out in a fully anechoic chamber (FRANKONIA). A network analyzer (E8363B, Agilent) connected via an amplifier to a log-periodic antenna (HL 562, R&S) was used to generate the source. The SE measurements were made by a small dipole antenna in the enclosure connected to the port 2 of the network analyzer. The SE was determined by the difference between the S21 for the shielded and unshielded cases.

Three cases of the normal incidence and the oblique incidence are investigated. First, the normal incident case for the vertical polarization is analyzed, where $\theta = 0$, $\phi = 90^0$ and $\psi = 0$.

Figure 4 represents the SE of the test point (14.5 cm × 20 cm × 10 cm). In the graph, the solid line shows the calculated results using the proposed model and the dotted line shows the results from the measurement.

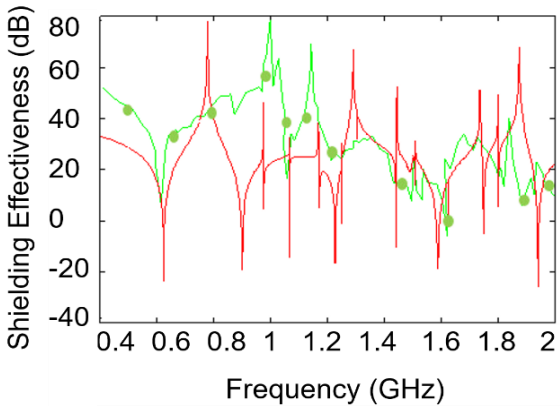

Fig. 4. The electric SE for the normal incident case. Solid line: our model. Dotted line: measurement.

Figure 4 shows that the SE deteriorates significately at those resonant frequencies. The proposed method can predict the multiple resonant points accurately. The resonant frequencies of different modes in the fabricated enclosure are given by the theoretical formula:

$$f = \frac{1}{2\sqrt{\mu\varepsilon}}\sqrt{\left(\frac{m}{a}\right)^2 + \left(\frac{n}{b}\right)^2 + \left(\frac{l}{d}\right)^2}. \qquad (22)$$

The SE obtained by the proposed methods decreases dramatically at 0.625 GHz, 0.9 GHz, 1.07 GHz, 1.25 GHz, 1.458 GHz, 1.58 GHz, 1.8 GHz, and 1.95 GHz, which are same as the resonant frequencies of modes TM_{110}, TE_{101}/TM_{120}, TM_{210}, TM_{220}, TE_{221}/TM_{221}, TE_{102}, TE_{202}, TE_{222}/TM_{222}, respectively. From Fig. 4 it is easy to find that the calculated results of the proposed model and the measured results are consistent in trend, especilaly at high frequencies. Therefore, higher-order modes should be included in the analytical formulas to get 0the reasonable results in high frequencies.

Another case for the obliquely incident wave with θ = 60°, φ = 30°, ψ = 30° is investigated. The SE of the enclosure from the proposed method and the measurement is displayed in Fig. 5.

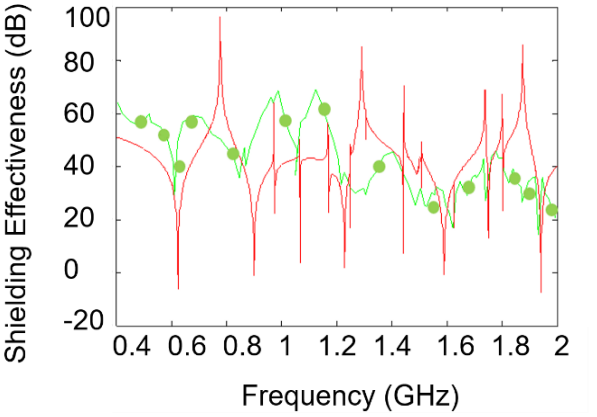

Fig. 5. The electric SE for the obliquely incident case. Solid line: our model. Dotted line: measurement.

The SE results for the obliquely incident wave with θ = 45°, φ = 60°, ψ = 45° are displayed in Fig. 6, and the comparisons with the CST simulations are also included. It can be found that many resonances happened at high frequencies, so multimode analytical method should be applied instead of TE_{10} mode analysis.

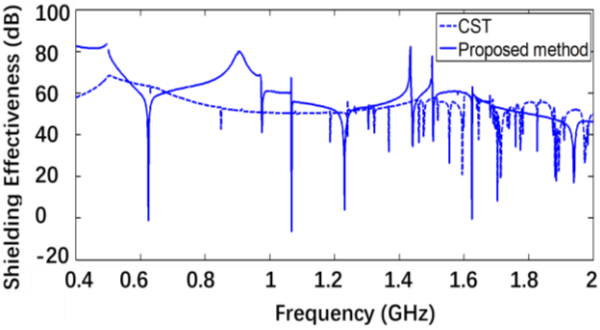

Fig. 6. The electric SE for obliquely incident case. Solid line: our model. Dotted line: CST simulation.

Some comparisons between the proposed method and other published literatures are also made. Table 2 shows the comparisons among the proposed method, the results from [11], and the results from the HFSS simulation. We can see that the results obtained with the proposed method are more consistent with the simulation results with HFSS than [11]. The excitation frequency is 700 MHz.

Table 2: Comparisons with other methods

Incident Angle	SE from the Proposed Method (dB)	SE from HFSS (dB)	SE from [11] (dB)
0°	20.54	14.03	-12.85
10°	20.67	14.78	-12.72
20°	21.08	15.88	-12.28
30°	21.79	17.3	-11.22
40°	22.85	23.74	-9.86
50°	24.38	26.7	-7.58
60°	26.56	26.94	-4.37
70°	29.85	28.34	-0.41
80°	35.73	28.71	6.63
90°	80.33	68.08	22.55

IV. DISCUSSION

Some parameters affecting the SE are studied in this part. The dimensions of the enclosure and the aperture are same as those in the part III.

A. SE varies with incident angle

The incident wave frequency is 1.1 GHz, and the polarization angle φ is 30°. The propagation vector of the incident wave is located at the X - Y plane, and the incident angle θ varies from 0 to 90°, leading to $\psi = 0$. Figure 7 demonstrates that the SE is the worst for the normal incident wave, and the SE increases with the incident angle until it reaches the maximum when the incident wave propagates along the long side of the aperture.

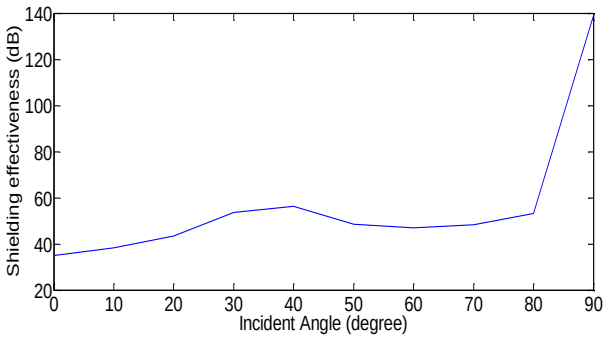

Fig. 7. The electric SE vs. the incident angle.

B. SE varies with the polarization angle

The incident angle θ in the X - Y plane is 30° and ψ is 45°. The polarization angle φ varies from 0 to 90°. Figure 8 shows that the SE is the worst when the polarization angle is 90°, in which case the ***E***-field is perpendicular to the long side of the aperture. On the other hand, the SE reaches the maximum when the polarization angle φ is equal to 45° since the equivalent source is determined by the $\sin\varphi$ and $\cos\varphi$ simultaneously.

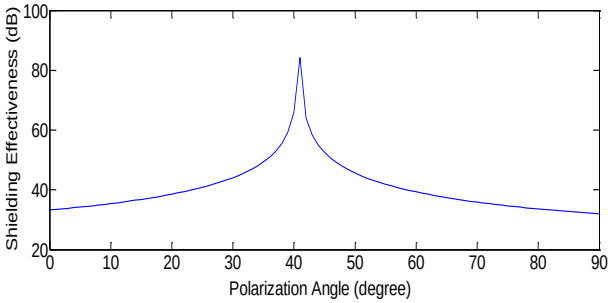

Fig. 8. The electric SE vs. the polarization angle.

C. SE varies with the enclosure wall thickness

The enclosure wall thickness, whose influence is explored, varies from 1 mm to 5 mm. The incident wave parameters are as: $\theta = 60°$, $\varphi = 30°$, $\psi = 30°$.

From Fig. 9, we can see that the SE increases with the enclosure wall thickness.

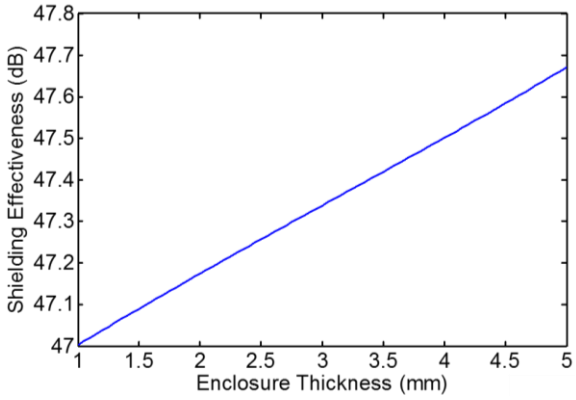

Fig. 9. The electric SE vs. the enclosure wall thickness.

V. CONCLUSION

The proposed model can calculate the SE of the rectangular enclosure with the off-center aperture fast and accurately. The oblique incidence and polarization are cogitated, and higher-order modes are included to enable the model to be applicable in higher frequencies. Therefore, the proposed analytical formulation is very useful for the practical design of the shielded enclosures in the electronic manufacturing industry.

ACKNOWLEDGMENT

This work has been supported by National Natural Science Foundation of China, No. 61201024.

REFERENCES

[1] B. L. Nie, P. A. Du, Y. T. Yu, and Z. Shi, "Study of the shielding properties of enclosures with apertures at higher frequencies using the transmission line modeling method," *IEEE Trans. Electromagn. Compat.*, vol. 53, no. 1, pp. 73-81,

Feb. 2011.

[2] C. Q. Jiao, L. Li, X. Cui, and H. Q. Li, "Subcell FDTD analysis of shielding effectiveness of a thin-walled enclosure with an aperture," *IEEE Transactions on Magnetics*, vol. 42, no. 4, 2006.

[3] R. Araneo and G. Lovat, "Fast MoM analysis of the shielding effectiveness of rectangular enclosures with apertures, metal plates, and conducting objects," *IEEE Trans. Electromagn. Compat.*, vol. 51, no. 2, pp. 274-283, May 2009.

[4] R. Araneo and G. Lovat, "Analysis of the shielding effectiveness of metallic enclosure excited by internal source through an efficient method of moment approach," *ACES Journal*, vol. 25, no. 7, pp. 600-611, July 2010.

[5] W. Abdelli, X. Mininger, L. Pichon, and H. Trabelsi, "Impact of composite materials on the shielding effectiveness of enclosure," *ACES Journal*, vol. 27, no. 4, pp. 369-375, Apr. 2012.

[6] C. Feng and Z. Shen, "A hybrid FD–MoM technique for predicting shielding effectiveness of metallic enclosures with apertures," *IEEE Trans. Electromagn. Compat.*, vol. 47, no. 3, pp. 456-462, Aug. 2005.

[7] M. P. Robinson, T. M. Benson, C. Christopoulos, J. F. Dawson, M. D. Ganley, A. C. Marvin, S. J. Porter, and D. W. P. Thomas, "Analytical formulation for the shielding effectiveness of enclosures with apertures," *IEEE Trans. Electromagn. Compat.*, vol. 40, no. 3, pp. 240-247, Aug. 1998.

[8] D. W. P. Thomas, A. C. Denton, T. Konefal, T. Benson, C. Christopoulos, J. F. Dawson, A. Marvin, S. J. Porter, and P. Sewell, "Model of the electromagnetic fields inside a cuboidal enclosure populated with conducting planes or printed circuit boards," *IEEE Trans. Electromagn. Compat.*, vol. 43, no. 2, pp. 161-169, May 2001.

[9] J. J. Shim, D. G. Kam, J. H. Kwon, and J. H. Kim, "Circuital modeling and measurement of shielding effectiveness against oblique incident plane wave on apertures in multiple sides of rectangular enclosure," *IEEE Trans. Electromagn. Compat.*, vol. 52, no. 3, pp. 566-577, Aug. 2010.

[10] B. l. N. and P. A. D., "An efficient and reliable circuit model for the shielding effectiveness prediction of an enclosure with an aperture," *IEEE Trans. Electromagn. Compat.*, vol. 57, no. 3, pp. 357-364, June 2015.

[11] C. C. Wang, C. Q. Zhu, X. Zhou, and Z. F. Gu, "Calculation and analysis of shielding effectiveness of the rectangular enclosure with aperture," *ACES Journal*, vol. 28, no. 6, pp. 535-544, June 2013.

[12] K. C. Gupta, R. Garg, and I. J. Bahi, *Microstip Lines and Slotlines*. Artech House, Norwood, MA, 1979.

Dan Shi received Ph.D. degree in Electronic Engineering from Beijing University of Posts & Telecommunications, Beijing, China in 2008. She has been working in Beijing University of Posts & Telecommunications. Her interests include electromagnetic compatibility, electromagnetic environment and electromagnetic computation. She has published more than 100 papers. She is the Chair of IEEE EMC Beijing chapter, Vice Chair of URSI E Commission in China, General Secretary of EMC Section of China Institute of Electronics.

Na Lv received her Bachelor degree in Communication Engineering from Beijing University of Posts and Telecommunications in Beijing, China in 2015. Now she is studying for Master degree in Beijing Univer-sity of Posts and Telecommunica-tions in Beijing, China. Her research interests include electromagnetic compatibility and electromagnetic environment.

Yougang Gao received his B.S. degree in Electrical Engineering from National Wuhan University, China in 1950. He was a Visiting Scholar in Moscow Technical University of Communication and Information in Russia from 1957 to 1959. He is now a Professor in Beijing University of Posts and Telecommunications, China. He has published several books: "Introduction of EMC, Inductive Coupling and Resistive Coupling", as well as "Shielding and Grounding". He became an EMP Fellow of US Summa Foundation since 2010.

Detection of the Faulty Sensors on Basis of the Pattern Using Symmetrical Structure of Linear Array Antenna

Shafqat Ullah Khan, M. K. A. Rahim, N. A. Murad, F. Zubir, O. Ayop, M. F. M. Yusoff, M. R. Hamid, and R. Dewan

Advanced RF & Microwave Research Group
Department of Communication Engineering, Faculty of Electrical Engineering
Universiti Teknologi Malaysia, 81310 Skudai, Johor, Malaysia
shafqatphy@yahoo.com, mdkamal@utm.my, noorasniza@utm.my, faridzubir@utm.my, osman@fke.utm.my, fairus@fke.utm.my, rijal@fke.utm.my, raimidewan@gmail.com

Abstract ─ In this paper, a simple method is proposed to diagnose the position of the damaged sensors. The position of the damaged sensors is diagnosed on the basis of the null depth level and the number of nulls for the degraded radiation pattern. The method is initiated with tabulation of the array radiation pattern with a single damaged sensor. The corresponding pattern is set as the reference to the radiation pattern of the failed sensors. The tabulated damaged array sensors are compared to a configuration of the assumed damaged sensor. The radiation pattern with deeper null depth level will be the location of the damaged sensor. Moreover, the symmetrical sensor damaged (SSD) technique diagnose the position of damaged sensor, in which on the basis of nulls one can detect the location of damaged sensors. The proposed method diagnoses the location of damaged sensors on the basis of pattern without complex computation as compared to available methods.

Index Terms ─ Array antenna, fault detection, null depth level, nulls.

I. INTRODUCTION

Detection of the damaged sensors in a phased array antenna is an important research topic for radar, satellite and microwave [1-5] applications. The array antenna with a large number of radiating sensors has the possibility of getting the failures for at least single unit of sensors. The sensor failures, damages the peak sidelobes level (PSL) and nulls [6-8]. To ensure the performances of array antenna are conformed to the desired requirements, failure sensors have to be detected regularly [9] and correction must be attempted [10-11]. Detection of the damaged sensors in an array antenna is unarguably the main task to be addressed in array testing [12-18]. Correct diagnosis of the damaged sensors for a large array antenna is a big challenge in both theoretical and algorithm point of view. Several available techniques in the literature to diagnose the position of the damaged sensors from the measurement of healthy and the degraded radiation power patterns [19-25]. Several techniques had been proposed such as the genetic algorithm [26], back propagation algorithm [27], matrix method [28], exhaustive searches [29], MUSIC [30], compressed sensing as well as Bayesian compressive sensing (BCS) [31-32]. Recently, Zhu et al. [33] proposed a method which does not requires a priori knowledge of the malfunctioning sensors and permits some sensors with complete failure. Fuchs et al. [34] has developed a fast diagnosis of the array antennas from a small number of far-field measurements which requires a priori knowledge of the reference array power pattern. This method uses the sparse recovery algorithms to diagnose the damaged sensor positions from a small number of measurements. However, the aforementioned diagnosis of damaged sensors requires a complex computation for each of the configuration of the array factor.

The symmetrical linear array is of great importance and has many advantages. In [35-36], the symmetrical element failure (SEF) gives better null depth level (NDL), while in [38] it requires half of the damaged pattern for the damaged sensor detection as compared to [37]. In [39], a linear symmetrical array antenna is used for failure correction, where the failed sensor signal is reconstructed from the symmetrical counterpart sensor by considering its conjugate. In this paper, a simple approach for the diagnosis of array antenna on the basis of the null depth level and nulls of the degraded far-field radiation power pattern is described using a linear symmetrical array. The method tabulates the radiation pattern of the array with single damaged sensor. Then, the corresponding radiation pattern the configuration of failed sensors under test is checked with the configuration of the damaged sensor. The radiation pattern with a deeper null depth level will be the location

Submitted On: October 25, 2016
Accepted On: February 28, 2017

of damaged sensor. The symmetrical sensor damaged (SSD) technique is used for the diagnosis of the damaged sensor, in which on the basis of the nulls one can detect the location of damaged sensors. This article is organized as follows. The problem formulation is described in Section 2, while Section 3 describes the proposed methodology of detecting the damaged sensors. Subsequently, Section 4 presents the simulation results of the proposed method. Finally, the conclusion is made in Section 5.

II. PROMLEM STATEMENT

Consider a linear reference array of $2K+1$ number of sensors with far-field radiation pattern is given by [40-41],

$$AF(\theta_i) = \sum_{n=-K}^{K} w_n \exp\left(jn\left(kd\cos\theta_i\right)\right), \tag{1}$$

where w_n is the weight vector of the reference array, k is the wave number $2\pi/\lambda$ and d is the distance between the antenna sensors. The degraded far-field power pattern of an array can be found using Equation (1) by making the weight excitation of that sensor equals to zero. The power pattern radiated by the degraded array can be identified by eliminating the weight excitation corresponding to the damaged sensors from the Equation (1). Furthermore, the degraded far field radiation pattern for the mth sensor damaged is given by the following expression:

$$AF_m(\theta_i) = \sum_{\substack{n=-K \\ n\neq m}}^{K} w_n \exp\left(jn\left(kd\cos\theta_i\right)\right). \tag{2}$$

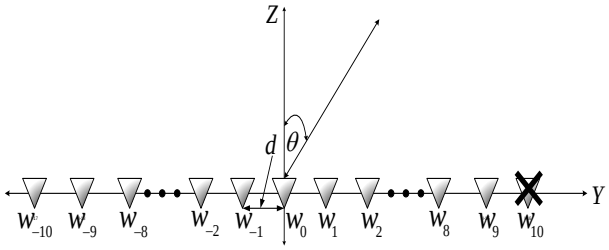

Fig. 1. Linear symmetrical array of $2K+1$ number of sensors with w_{10} sensor damaged.

Assume that the sensor, w_{10} in the array is damaged as shown in Fig. 1. The main objective is to detect the locations of the damaged sensors. Numerous techniques are found in the literature that diagnoses the locations of the damaged sensors. However, none of them is able to diagnose the damaged sensor locations on the basis of the radiation power pattern. The power pattern for the w_{10} sensors damaged is shown in Fig. 2 by the red solid line.

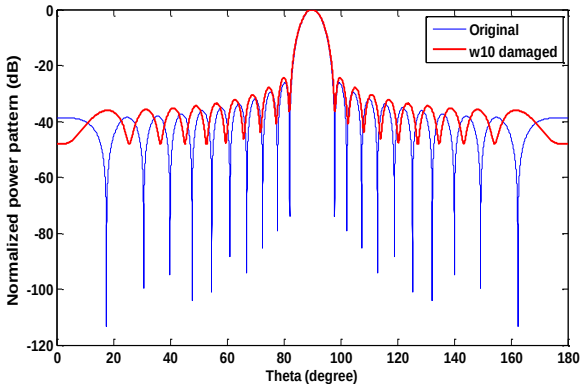

Fig. 2. Linear symmetrical Taylor pattern radiated by 21 sensors with w_{10} sensor damaged.

III. PROPOSED METHODOLOGY

The proposed methodology to diagnose the locations of the damaged sensors is based on the deeper null depth level and the number of nulls. As assumed for the damaged of w_{10} sensor, the null depth level is lost as depicted in Fig. 2. The pattern of w_{10} damaged sensors is then compared with the available damaged patterns. After comparing with the available damaged patterns, the symmetrical counterpart of w_{10} as shown in Fig. 3 will give a deeper null depth level, i.e., symmetrical sensor damaged (SSD) of w_{10} will give deeper nulls as shown in Fig. 4. Moreover, SSD technique predicts the location of the damaged sensors on the basis of the nulls. As the damaged sensors get nearer to the center of the array, the number of nulls reduces. If D represents the set of damaged sensors, i.e., all the possible patterns for a single damaged sensor. The degraded far-field power pattern of a set of D damaged sensors can be obtained by excluding the weight of the damaged sensor from the Equation (1) as shown in Equations (3) and (4):

$$AF_D(\theta_i) = AF(\theta_i) - \sum_{n\in D} AF(\theta_i), \tag{3}$$

$$AF_F(\theta_i) = \sum_{\substack{n=-M \\ n\notin D}}^{M} AF(\theta_i). \tag{4}$$

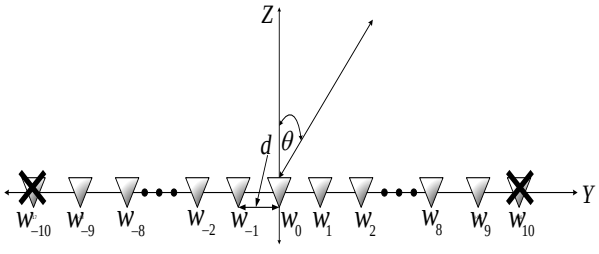

Fig. 3. Linear symmetrical array of $2K+1$ number of sensors with w_{10} SSD.

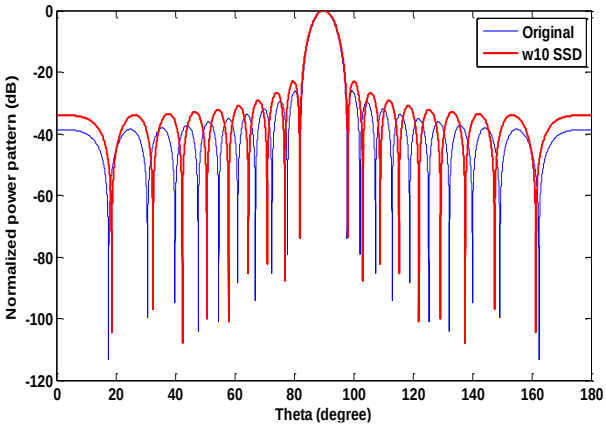

Fig. 4. Linear symmetrical array of 21 number of sensors with w_{10} SSD.

Assume that the number of patterns, radiated by the array with a known single damaged sensors. $\{AF_D(\theta_i)\}_{n=-K}^{K}$ is the $2K+1$ number of available damaged sensor patterns and $AF_m(\theta_i)$ is the pattern of the mth damaged sensor assumed to be failed. The method of detecting the damaged sensors in array antenna starts with the measurement of the damaged sensors pattern in θ_m direction. Then, the cost function C compares the damaged patterns with a given configuration of the failed sensor as shown in Equation (5). The cost function which gives the deeper null depth level will be the location of the damaged sensors, i.e., the symmetrical counterpart sensor will give a deeper null depth level:

$$C = \sum_{m=1}^{M} \left| AF_m(\theta_i) - AF_D(\theta_i) \right|^2 . \quad (5)$$

Firstly, the w_{10} SSD gives a deeper null depth level which allows the sensors position to be easily detected. Secondly, the number of nulls for w_{10} SSD is 18 which is reduced by 2.

IV. SIMULATION RESULTS

In this section, consider a linear symmetrical array composed of 21 number of sensors which are placed symmetrically from the origin along the x-axis. Analytical procedure [42] is used for the healthy set-up to radiate in the direction of $\theta = 90^{\circ}$ with sidelobe level of -30 dB. The radiation power pattern, shown in Fig. 5, has been created by taking a linear Taylor distribution with SLL=-30 and $n = 6$. So, there will be 20 number of nulls and one main beam for this healthy set up as shown in Fig. 5 by the blue solid lines. The number of nulls reduces as the sensors in the array become damaged near the centre of the array. At the first instant, it is assumed that the sensor w_9 become damaged in the array. The pattern of damaged sensor w_9 damaged is shown in Fig. 5 by the red solid line. To detect the pattern of the damaged sensor w_9 all the available damaged patterns, i.e., $\{AF_D(\theta_i)\}_{n=-K}^{K}$ are compared. The cost function in Eq. (5) is then compared for a given configuration of all the available damaged patterns and the sensor is assumed to be damaged. i.e., w_9. After comparison, the SSD of w_9 gave a deeper null depth level. The technique proposed in this article which uses Eq. (1) to tabulate both of the healthy power pattern as well as the one damaged pattern calculated at all the directions of the given samples. The computation of cost function in Eq. (5) for a particular configuration of the damaged sensors is very fast, because it requires using the available damaged patterns in Eq. (4) and the pattern of the assumed failed sensor only. This simple methodology will improve the computational cost as compared to the available techniques. Moreover the SSD technique is able to diagnose the location of damaged sensors without the needs of complex calculation. On the basis of the number of nulls of the degraded patterns, the position of the damaged sensors can be easily detected. For w_9 SSD, the pattern achieves deeper null depth level. Therefore, our decision is to diagnose the positions of the damaged sensors on the basis of null depth level and nulls. In this case, the number of nulls for w_9 SSD is 16. The number of nulls is reduced by 4 if w_9 SSD is occurrig as shown in Fig. 6. In the simulation results, a total of M=16 number of samples with no measurement error is considered.

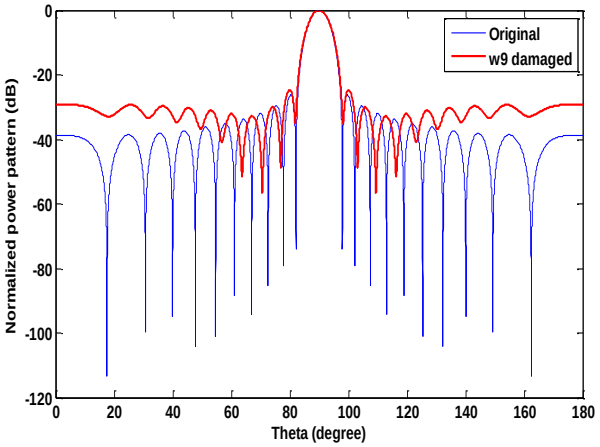

Fig. 5. Linear symmetrical Taylor pattern radiated by 21 sensors with w_9 damaged sensor damaged.

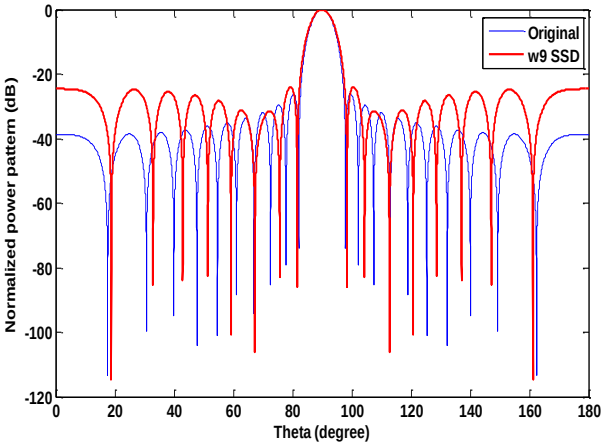

Fig. 6. Linear symmetrical array of 21 number of sensors with w_9 SSD.

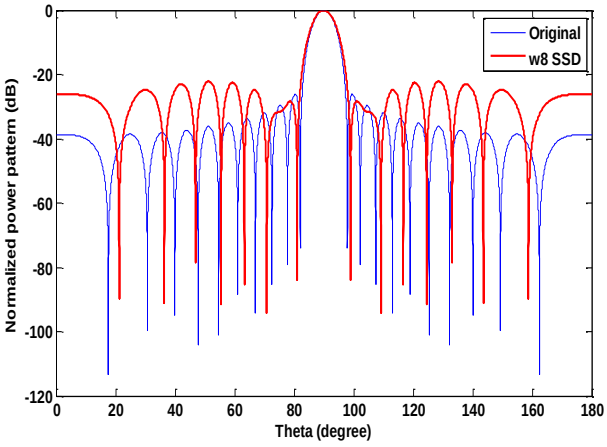

Fig. 7. Linear symmetrical array of 21 number of sensors with w_8 SSD.

The same procedure is repeated to diagnose the location of the damaged sensor w_8. The w_8 sensor pattern is compared with a given configuration of the available damaged pattern and then the cost function in Eq. (5) gives a deeper null depth level with w_8 SSD as shown in Fig. 7. At the same time, the number of the nulls for w_8 SSD is reduced by 6 and it is shown in Fig.7. Now, if the w_7 sensor is damaged in an array of 21 number of sensors, pattern of damaged sensor w_7 is compared with the given configuration of the available damaged pattern in cost function Eq. (5). Again, the w_7 SSD gives a deeper null depth level as depicted in Fig. 8

Moreover, the number of nulls for SSD is 12 which is reduced by 8. Therefore, the position of the damaged sensors can be easily detected from the degraded patterns on the basis of null depth level and number of nulls. From Table 1, it is obvious that if the damaged sensors gets nearer to the center of the array, the nulls are reduced by 2. For w_6 SSD, the number of nulls is 10. For w_5 SSD, the number of nulls is 8. For other following cases, the number of null has decreased by 2 as seen in Table 1. This symmetrical changes of number of nulls in the array radiation pattern is of great interest for the researcher.As one can see from Fig. 2, due to a single failure sensor one can not decide which sensor is damaged. On the basis of the SSD technique, the sidelobes level also conforms the diagnosis of the damaged sensors. From Fig. 4 and Fig. 6 it is clear that for w_9 SSD, the sidelobes level is higher than w_{10} SSD. Similarly, the sidelobes level for w_7 SSD is higher than w_8 SSD. From the simulation results it is clear that as the damage SSD nearer to the center of the array, the sidelobes level is increases while the number of nulls is reduces.

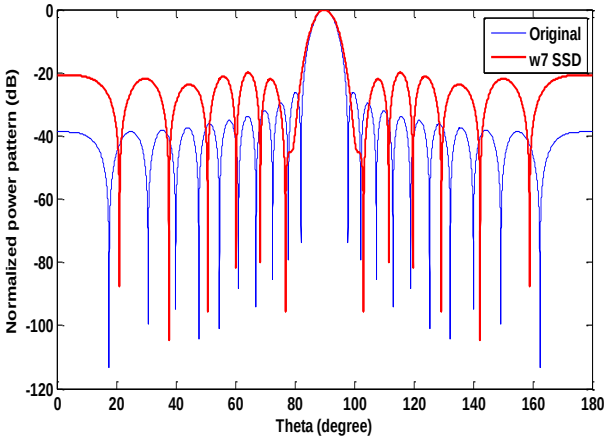

Fig. 8. Linear symmetrical array of 21 number of sensors with w_7 SSD.

Table 1: Detection of damaged sensor on the basis of number of nulls

Symmetrical Sensor Samaged (SSD)	Number of Nulls
w_{10}	18
w_9	16
w_8	14
w_7	12
w_6	10
w_5	8
w_4	6

In this case the performance of the proposed method is compared with the conventional method [37-38]. In [37], the main goal is to diagnose the location of faulty sensors using bacteria foraging optimization (BFO) technique. Let us consider a linear array of 21 number of sensors. The damaged patterns were generated by

making their weights equals to zero. We considered that the 3rd, and 19th sensors are damaged in an array of 21 number of sensors. For the detection of 3rd and 19th failure we require $\sum_{f=1}^{2} \frac{N!}{[f!(N-f)!]} = 210$ number of different patterns by the conventional method [37], while the method [38] requires 105 number of patterns for the same scenario of the damaged sensors. But our proposed method requires no computation, just on the basis of radiation patterns and number of nulls one can decide the location of the damaged sensors. The damaged array pattern obtained by the conventional method [37] as depicted in Fig. 9 while the performance is shown in Fig. 10. The same faulty scenario is diagnosed by [38] with half the number of samples poaints as shown in Fig. 11 and Fig. 12.

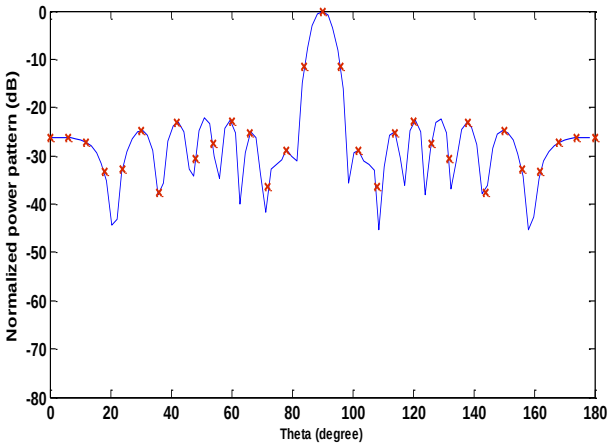

Fig. 9. Damaged array pattern with fault at 3rd and 19th sensors with 31 samples.

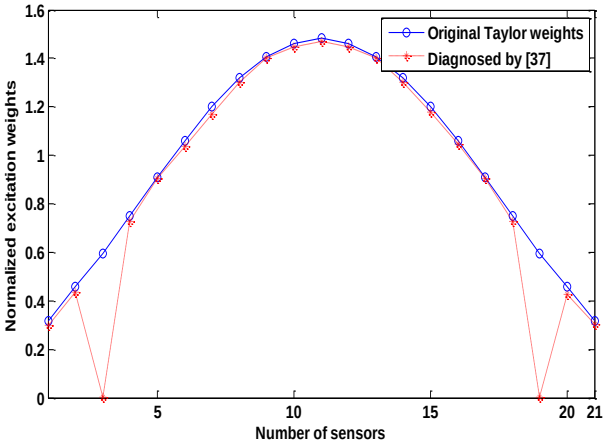

Fig. 10. Performance of the conventional method [37] with 31 samples.

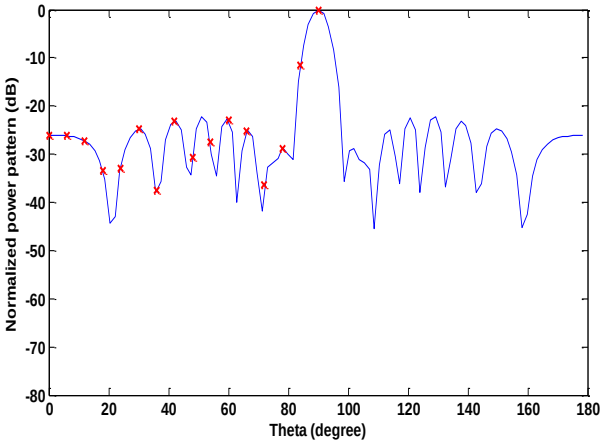

Fig. 11. Performance of the conventional method [38] with 16 samples.

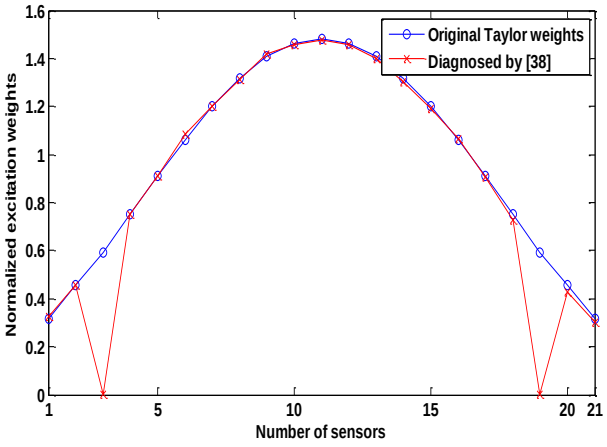

Fig. 12. Performance of the conventional method [38] with 16 samples.

V. CONCLUSION

In this paper, a simple approach of the damaged sensor detection in an antenna array on the basis of the deeper null depth level and nulls have been proposed. By using this approach one can easily detect the location of damaged sensors on the basis of degraded far-field radiation pattern. From the simulation results, it is observed that if the damaged sensors nearer the center of the array, the number of the nulls are decreases by 2. From this observation, it is a valid problem for the researcher and hence the number of nulls reduces as the damaged sensors get closer to the center of array. This approach is directly applicable to the L-type and circular arrays.

ACKNOWLEDGMENT

The authors thank the Ministry of Higher Education

(MOHE) for supporting the research work; Research Management Centre (RMC), School of Postgraduate Studies (SPS), Communication Engineering Department, Faculty of Electrical Engineering (FKE), Universiti Teknologi Malaysia (UTM) Johor Bahru under Grant Number 12H09 and 03E20.

REFERENCES

[1] S. Caorsi, M. Donelli, F. De Natale, D. Franceschini, and A. Massa, "A versatile enhanced genetic algorithm for planar array design," *Journal of Electromagnetic Waves and Applications*, vol. 18, no. 11, pp. 116-119, 2004.

[2] S. M. Makouie and A. Ghorbani, "Comparison between genetic and particle swarm optimization algorithms in optimizing ships' degaussing coil currents," *Applied Computational Electromagnetics Society Journal*, vol. 31, no. 5, 2016.

[3] S. Roy, et al., "Comparison of evolutionary algorithms for optimal design of broadband multilayer microwave absorber for normal and oblique incidence," *Applied Computational Electromagnetics Society Journal*, vol. 31, no. 1, 2016.

[4] R. Azaro, M. Donelli, G. Boato, E. Zeni, and A. Massa, "Design of prefractal mono polar antenna for 3.4-3.6 GHz Wi-Max band portable devices," *Electronic Letters*, vol. 5, no. 4, pp. 116-119, 2006.

[5] M. L. M. Lakshmi, et al., "Amplitude only linear array synthesis with desired nulls using evolutionary computing technique," *Applied Computational Electromagnetics Society Journal*, vol. 31, no. 11, 2016.

[6] S. U. Khan, I. M. Qureshi, F. Zaman, A. Naveed, B. Shoaib, and A. Basit, "Correction of faulty sensors in phased array radars using symmetrical sensor failure technique and cultural algorithm with differential evolution," *The Scientific World Journal (TSWJ)*, vol. 2014, Article ID 852539, 10 pages, 2014. doi:10.1155/2014/852539.

[7] S. U. Khan, I. M. Qureshi, and B. Shoaib, "Meta-heuristic cuckoo search algorithm for the correction of failed array antenna," *Mehran University Research Journal*, vol. 34, no. 4, Oct. 2015.

[8] S. U. Khan, I. M. Qureshi, B. Shoaib, and A. Naveed, "Correction of faulty arrays using nature inspired hybrid heuristic computation technique," *Submitted to Sindh University Research Journal*.

[9] S. U. Khan, I. M. Qureshi, H. Haider, F. Zaman, and B. Shoaib, "Diagnosis of faulty sensors in phased array radar using compressed sensing and hybrid IRLS-SSF algorithm," *Wireless Personal Communications*, vol. 89, no. 2, pp. 1-20, 2016.

[10] L. Poli, et al., "Failure correction in time-modulated linear arrays," *IET Radar, Sonar & Navigation*, vol. 8, no. 3, pp. 195-201, 2014.

[11] O. P. Acharya, A. Patnaik, and N. S. Sachendra, "Limits of compensation in a failed array antenna," *International Journal of RF and Microwave Computer-Aided Engineering*, vo. 24, no. 6, pp. 635-645, 2014.

[12] O. M. Bucci, M. D. Migliore, G. Panariello, and G. Sgambato, "Accurate diagnosis of conformal arrays from near-field data using the matrix method," *IEEE Trans. Antennas Propag*., vol. 53, no. 3, pp. 1114-1120, Mar. 2005.

[13] M. D. Migliore, "A compressed sensing approach for array diagnosis from a small set of near-field measurements," *IEEE Trans. Antennas Propag*., vol. 59, no. 6, pp. 2127-2133, June 2011.

[14] M. D. Migliore, "Array diagnosis from far-field data using the theory of random partial fourier matrices," *IEEE Trans. Antennas Wireless Propag. Lett.*, vol. 12, pp. 745-748, July 2013.

[15] B. Fuchs and M. D. Migliore, "Accurate array diagnosis from near-field measurements using reweighted minimization," *IEEE Antennas Propag. Symp*., Orlando, FL, USA, pp. 2255-2256, 2013.

[16] B. Fuchs, L. Le Coq, L. Ferro-Famil, and M. D. Migliore, "Comparison of methods for reflect array diagnostic from far field measurements," in *Proc. IEEE Int. Symp. Antennas Propag*., pp. 398-399, July 2015.

[17] J. J. Lee, E. M. Ferrer, D. P. Woollen, and K. M. Lee, "Near-field probe used as a diagnostic tool to locate defective elements in an array antenna," *IEEE Trans. Antennas Propag*., vol. 36, no. 3, pp. 884-889, June 1988.

[18] G. Oliveri, L. Manica, and A. Massa, "ADS-based guidelines for thinned planar arrays,'' *IEEE Trans. Antennas Propag*., vol. 58, no. 6, pp. 1935-1948, June 2010.

[19] A. Patnaik, B. Choudhury, P. Pradhan, R. K. Mishra, and C. Christodoulou, "An ANN application for fault finding in antenna arrays," *IEEE Trans. Antennas Propagat*., vol. 55, pp. 775-777, 2007.

[20] O. M. Bucci, A. Capozzoli, and G. D'Elia, "Diagnosis of array faults from far-field amplitude-only data," *IEEE Trans. Antennas Propag*., vol. 48, no. 5, pp. 647-652, 2000.

[21] G. Castaldi, V. Pierro, and I. Pinto, "Efficient faulty element diagnostic of large antenna arrays by discrete mean field neural nets," *Progress in Electromagnetics Research*, vol. 25, pp. 53-76, 2000.

[22] B. Choudhury, O. P. Acharya, and A. Patnaik, "Bacteria foraging optimization in antenna engineering: An application to array fault finding," *International Journal of RF and Microwave Computer-Aided Engineering*, vol. 23, pp. 141-148, Mar. 2013.

[23] S. U. Khan, I. M. Qureshi, A. Naveed, B. Shoaib, and A. Basit, "Detection of defective sensors in phased array using compressed sensing and hybrid genetic algorithm," *Journal of Sensors*, vol. 2016, Article ID 6139802, 8 pages, 2016. doi:10.1155/2016/6139802.

[24] S. U. Khan, I. M. Qureshi, F. Zaman, A. Basit, and W. Khan, "Application of firefly algorithm to fault finding in linear arrays antenna," *World Applied Sciences Journal (WASJ)*, vol. 26, no. 2, pp. 232-238, 2013. doi: 10.5829/idosi.wasj.2013.26.02.1387.

[25] S. U. Khan, I. M. Qureshi,F. Zaman, B. Shoaib, and K. Ashraf, "An application of hybrid nature inspired computational technique to detect faulty element in array antenna," *Proceedings of 2015 12th International Bhurban Conference on Applied Sciences and Technology, IEEE IBCAST 2015*, pp. 629-632, 2015.

[26] J. A. Rodríguez, F. Ares, H. Palacios, and J. Vassal'lo, "Finding defective elements in planar arrays using genetic algorithms," *Progr. Electromagn. Res., PIER*, vol. 29, pp. 25-37, 2000.

[27] J. Lee, E. M. Ferrer, D. P. Woollen, and K. M. Lee, "Near-field probe used as a diagnostic tool to locate defective elements in an array antenna," *IEEE Trans. Antennas Propag*., vol. 36, no. 3, pp. 884-889, June 1988.

[28] L. Gattoufi, D. Picard, Y. R. Samii, and J. C. Bolomey, "Matrix method for near-field diagnostic techniques of phased array antennas," in *Proc. IEEE Int. Symp. Phased Array Syst. Technol*., pp. 52-57, 1996.

[29] J. A. Rodríguez, F. Ares, H. Palacios, M. F. Delgado, R. Iglesias, and S. Barrow, "Rapid method for finding faulty elements in antenna arrays," *IEEE Trans. Antennas Propagat*., vol. 57, pp. 1679-1683, 2009.

[30] A. Buonanno and M. D'Urso, "On the diagnosis of arbitrary geometry fully active arrays," presented at the *Eur. Conf. Antennas Propag. (EuCAP)*, Barcelona, Apr. 12-16, 2010

[31] M. D. Migliore, B. Fuchs, L. Le Coq, and L. Ferro-Famil, "Compressed sensing approach for reflect array diagnostic from far field measurements," in *Proc. Eur. Microw. Conf*., pp. 289-292, Sep. 2015.

[32] G. Oliveri, P. Rocca, and A. Massa, "Reliable diagnosis of large linear arrays, a Bayesian compressive sensing approach," *IEEE Trans. Antennas Propag*., vol. 60, no. 10, pp. 4627-4636, Oct. 2012.

[33] C. Zhu, et al., "Impaired sensor diagnosis, beamforming, and DOA estimation with difference co-array processing," *IEEE Sensors Journal*, vol. 15, no. 7, pp. 3773-3780, 2015.

[34] B. Fuchs, L. Le Coq, and M. D. Migliore, "Fast antenna array diagnosis from a small number of far-field measurements," *IEEE Transactions on Antennas and Propagation*, vol. 64, no. 6, pp. 2227-2235, 2016.

[35] S. U. Khan, I. M. Qureshi, F. Zaman, and A. Naveed, "Null placement and sidelobe suppression in failed array using symmetrical element failure technique and hybrid heuristic computation," *Progress In Electromagnetics Research B*, vol. 52, pp. 165-184, 2013.

[36] S. U. Khan, I. M. Qureshi, B. Shoaib, and A. Basit, "Correction of faulty pattern using cuckoo search algorithm and symmetrical element failure technique along with distance adjustment between the antenna array," *Proceedings of 2015 12th International Bhurban Conference on Applied Sciences and Technology, IEEE IBCAST 2015*, pp. 633-636, 2015.

[37] B. Choudhury, O. P. Acharya, and A. Patnaik, "Bacteria foraging optimization in antenna engineering: An application to array fault finding," *International Journal of RF and Microwave Computer-Aided Engineering*, vo. 23, no. 2, pp. 141-148, 2013.

[38] S. U. Khan, I. M. Qureshi,F. Zaman, and W. Khan, "Detection of faulty sensor in array using symmetrical structure and cultural algorithm hybridized with differential evolution," *Frontiers of Information Technology & Electronic Engineering*. doi.10. 10.1631/FITEE.1500315.

[39] S. U. Khan, I. M. Qureshi, B. Shoaib, and A. Naveed, "Recovery of failed element signal with a digitally beamforming using linear symmetrical array antenna," *Journal of Information Science and Engineering (JISE)*, vol. 32, no. 3, pp. 611-624, 2016.

[40] I. Wolf, "Determination of the radiating system which will produce a specified directional characteristic," *Proc. IRE*, vol. 25, pp. 630-643, May 1937.

[41] O. Gassab and A. Azrar, "Novel mathematical formulation of the antenna array factor for side lobe level reduction," *Applied Computational Electromagnetics Society Journal*, vol. 31, no. 12, 2016.

[42] C. A. Balanis, *Antenna Theory: Analysis and Design*. Wiley, New Jersey, 2005.

Shafqat Ullah Khan received, M.S. and Ph.D. degree in Electronic Engineering from from International Islamic University Islamabad and ISRA University in 2008 and 2015 respectively. Currently he is a Post Doc Fellow at University Technology Malaysia.

M. K. A. Rahim was born in Alor Star Kedah Malaysia on the 3rd of November, 1964. He received the B.Eng. degree in Electrical and Electronic Engineering from University of Strathclyde, UK in 1987. He obtained his Master Engineering from University of New South Wales, Australia in 1992. He graduated his Ph.D. in 2003 from University of Birmingham, U.K., in the field of Wideband Active Antenna. From 1992 to 1999, he was a OLecturer at the Faculty of Electrical Engineering, UTM. From 2005 to 2007, he was a Senior Lecturer at the Department of Communication Engineering, UTM. He is now a Professor at Universiti Teknologi, Malaysia. His research interest includes the design of active and passive antennas, electromagnetic band gap (EBG), artificial magnetic conductors (AMC), left-handed metamaterials and computer aided design for antennas.

Noor Asniza Murad obtained her first degree in 2001 from Universiti Teknologi Malaysia (UTM). She received her M.Eng. in 2003 from the same university. She joined Emerging Device Technology Group, University of Birmingham, UK and obtained her Ph.D. in 2011. Her research interests include antenna design for RF and millimeterwave circuits design. Currently, Murad is a Senior Lecturer at Faculty of Electrical Engineering, UTM.

Farid Zubir received his first degree in Electrical Engineering from Universiti Teknologi Malaysia in 2008. He has completed his Master at the same university in 2010. He has officially completed his Ph.D. at the University of Birmingham in 2015 for research into Power Amplifiers in Microwave Transmitters. Currently, he is a Senior Lecturer at the Faculty of Electrical Engineering, UTM. His research interests are in the area of antenna design and reflectarray antenna.

Osman bin Ayop received B.Eng., M.Sc. and Ph.D. in Electrical Engineering from UTM Malaysia in 2007, 2010, 2016 respectively. His research interests are in the field of antennas, propagation, and also metamaterials. He is active in a research group which is Advanced RF and Antenna Research Group (ARFMRG). He is currently working as a Senior Lecturer in the Department of Communication Engineering, Universiti Teknologi Malaysia.

M. F. M. Yusoff is a Graduate Faculty Member of the Faculty of Electrical Engineering, UTM. He received his Bachelor in 2002 and Master in 2005 from UTM. He obtained his Ph.D. in 2012 from University of Rennes 1, France in the area of Signal Processing. His research interest areas is antenna design and millimeter waves.

M. R. Hamid received the Ph.D. degree at the University of Birmingham,United Kingdom. He has been with Universiti Teknologi Malaysia at the Faculty of Electrical Engineering, UTM since 1999. Currently his position is a Senior Lecturer. His major research interest is reconfigurable antenna design for multimode wireless applications.

Raimi Dewan received his Bachelor degree in Engineering (Electrical-Telecommunication) and Master degree in Electrical from Universiti Teknologi Malaysia in 2010 and 2013 respectively. He recently pursues his Ph.D. at the same university. His research interests include antenna design, metamaterial, applied electromagnetics, radio frequency (RF) and microwave devices.

Antipodal Linear Tapered Slot Antenna with Dielectric Loading Using Substrate Integrated Waveguide Technology for 60 GHz Communications

Nishesh Tiwari and T. Rama Rao

Department of Telecommunication Engineering
SRM University, Chennai, Tamilnadu-603203, India
nitizaz@gmail.com, ramaraot@outlook.com

Abstract ─ The 60 GHz band is capable of providing high speed communication. In this paper a substrate integrated waveguide (SIW) fed high gain antipodal linear tapered slot antenna (ALTSA) is presented. In order obtain high gain the dielectric loading is applied to the ALTSA in addition to the corrugation structure. Using SIW technology, a highly efficient, compact and low cost planar design is realized. An electromagnetic field simulation tool is used for design and simulation of the antenna. SIW power divider is used for designing 1x4 ALTSA array. To validate the proposed design, prototype is fabricated and measured. The simulated results agree well with the measured values which validates the proposed design. The measured return loss of 1x4 ALTSA array is better than 12 dB over the entire 60 GHz band (57 GHz - 64 GHz). The measured gain of 1x4 ALTSA array is 23.1 $\pm$ 0.5 dBi over the 60 GHz band.

Index Terms ─ ALTSA, dielectric loading, high gain, millimeter wave, SIW, 60 GHz.

I. INTRODUCTION

In recent years the demand of large bandwidth for high speed communication is growing at a faster pace. The 60 GHz band (57 GHz - 64 GHz) is capable of providing high speed wireless communication permitting transfer of high volumes of uncompressed data at the speed of multi-gigabit per second [1-2]. The losses associated with the microstrip circuit are quite high in the millimeter wave frequency band. Therefore, more efficient technology like the substrate integrated waveguide (SIW) is needed. SIW has the positive traits of the traditional rectangular waveguide such as low loss, high quality factor, complete shielding and capability of handling high power along with the advantage of low cost and planar circuit design [3-4]. Numerous research works involving SIW have been reported for many years [3-6]. The 60 GHz band suffers from attenuation due to atmospheric absorption. This requires the use of high gain antennas to overcome the losses. Tapered slot antennas (TSA) are popular for their wide bandwidth, good return loss and high gain. Antipodal linear tapered slot antenna (ALTSA) is a type of TSA which uses antipodal geometry in its design where the top and bottom metallized parts on a substrate are tapered in opposite direction. Researchers have designed antipodal Vivaldi antenna with wide bandwidth ranging from 4-50 GHz in [7]. The antenna gain varies from 3-12 dBi over the bandwidth. In [8], a high gain antipodal Fermi tapered slot antenna with gain of 18.75 dBi at 60 GHz has been proposed. In [9], Hao et al. introduced a novel technique for feeding ALTSA with SIW where the top and bottom tapered edges are overlapped to overcome the impedance mismatch between the ALTSA and SIW feed. TSA with corrugation structure have been used for reducing the width of the antenna while minimizing any significant degradation in radiation pattern [10-11]. This helps in making the antenna array of compact size. Further, corrugation is also known for increasing antenna gain, reducing side lobe level and reducing cross polarization, thus improving the overall performance of antenna. In [11], Djerafi et al. have developed rectangular corrugated ALTSA array with quasi triangular power divider. The gain of the 1x12 array is 19.25 dBi. In [12], Shrivastava et al. have presented corrugated ALTSA for 60 GHz band. In [13], Dae-Myoung et al. have developed ALTSA with half circular slots as corrugation structure. The gain at 7 GHz is 12.4 dBi. Dielectric loading also helps in enhancement of antenna gain. By placing the dielectric slab in front of the antenna its gain can be increased. The dielectric slab in this case acts as a guiding structure [14] and enhances the gain of the antenna [15]. In [16], dielectric loading is applied to a planar SIW horn antenna to narrow down the E-plane beamwidth and increase the gain. In [14] Ghassemi et al. have developed a high gain ALTSA array with SIW horn structure and rectangular dielectric loading for E and W band. The gain of 1x4 ALTSA array is 19$\pm$1 dBi.

In this paper, ALTSAs having rectangle with semi-circular top shaped dielectric loading structures are used to obtain a high gain antenna array in the 60 GHz band. The antenna array is designed and simulated in Ansys HFSS software. It is fabricated on Rogers RT/Duroid 5880 substrate which has dielectric constant of 2.2 and

Submitted On: December 29, 2016
Accepted On: March 18, 2017

thickness of 0.254 mm.

II. ANTENNA DESIGN

A. Design of SIW

SIW structure is shown in Fig. 1. In SIW there are two rows of metallic vias embedded in the dielectric substrate which act as waveguide by connecting the two parallel metal plates on the top and bottom. The two rows of vias act as the walls of the rectangular waveguide along with the top and bottom metal plates. Nevertheless, though SIW has electrical similarities to rectangular waveguide and provides advantages similar to the rectangular waveguide, it is also prone to leakage problem if the design rules are not followed properly. Some design rules and equations have been formulated by researchers in the past for proper design of SIW. The via diameter and the space between the vias should be selected as per Equations (1) and (2) respectively [17]:

$$D_{via} < \frac{\lambda_g}{5}, \quad (1)$$

$$S \leq 2D_{via}, \quad (2)$$

where λ_g is the guided wavelength, D_{via} is the diameter of the via and S is the space between the vias. The effective width of the waveguide is given by Equation (3) [18]:

$$W_{eff} = W_{siw} - 1.08\frac{{D_{via}}^2}{S} + 0.1\frac{{D_{via}}^2}{W_{siw}}, \quad (3)$$

where W_{eff} is the effective width, W_{siw} is the width of the SIW which is 2.69 mm, D_{via} is the diameter of the via which is 0.4 mm and S is the space between the vias which is 0.7 mm. The cut off frequency for the SIW in TE mode is given by Equation (4):

$$f_{c,mn} = \frac{c}{2\sqrt{\varepsilon_r}}\sqrt{\left(\frac{m}{a}\right)^2 + \left(\frac{n}{b}\right)^2}, \quad (4)$$

where f_c is the cutoff frequency, m and n are the mode numbers, ε_r is the dielectric constant, a is the width of the waveguide and b is the height. For a given waveguide the dominant mode is the mode having lowest cut-off frequency. In rectangular waveguide TE_{10} is the fundamental mode and same is also true for SIW. Figure 2 shows the E-field distribution in the SIW.

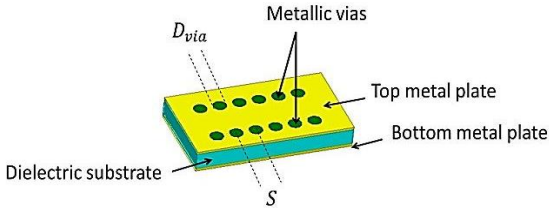

Fig. 1. SIW structure.

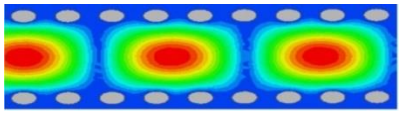

Fig. 2. E-field distribution in SIW.

B. Dielectric loaded ALTSA array

An ALTSA is a type of TSA. Yngvesson et al. have reported that the performance of TSA is sensitive to the thickness t and the dielectric constant ε_r in [19]. Hence, a factor $f_{substrate}$ for efficient performance of TSA has been defined as:

$$f_{substrate} = \frac{t(\sqrt{\varepsilon_r}-1)}{\lambda_0}. \quad (5)$$

For good performance of tapered slot antenna the substrate thickness should satisfy Equation (6). Here, with substrate thickness of 0.254 mm $f_{substrate}$ is 0.024, which satisfies Equation (6):

$$0.005 \leq f_{substrate} \leq 0.03. \quad (6)$$

The authors have presented a dielectric loaded ALTSA in [20]. Four such ALTSAs are placed adjacent to each other to form 1x4 ALTSA array. Figure 3 shows the 1x4 array configuration. The dimension of the antenna array is listed in Table 1. The inter-element spacing for the ALTSA array is 11.25 mm.

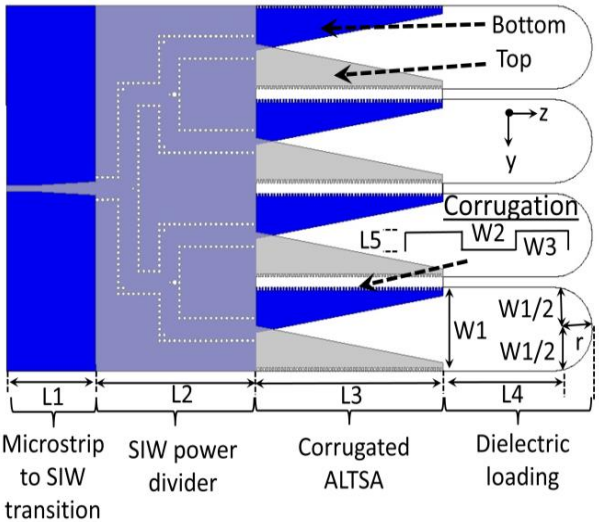

Fig. 3. ALTSA array configuration.

Table 1: Dimension of ALTSA array

Parameter	Value (Unit: mm)
L1	12
L2	21.38
L3	25
L4	15
L5	0.4
W1	10
W2	0.2
W3	0.2
r	5

SIW power divider is used for the design of 1x4 ALTSA array. The SIW power divider feeds each of the four ALTSA with power of same amplitude and phase. Figure 4 shows the design of SIW power divider with E-

field distribution. Proper placements of the inductive posts are essential for proper division of the power. In Fig. 4, Da = 0.3, Db = 0.3, Dc = 0.6, Dd = 0.4, La = 0.95, Lb = 0.15, Lc = 0.2, Ld = 0.32, Le = 0.25, Lf = 21.38, Wr = 19.81 and Ws = 8.56. Figure 5 shows the simulated S-parameters of the SIW power divider. From Fig. 5, it is observed that S11 is below -10 dB from 57 GHz to 64 GHz. Also, S21, S31, S41 and S51 have similar magnitudes over the 60 GHz band. The simulated phase at the output of the SIW power divider is shown in Fig. 6. From Fig. 6, it is seen that the phases of S21, S31, S41 and S51 are similar.

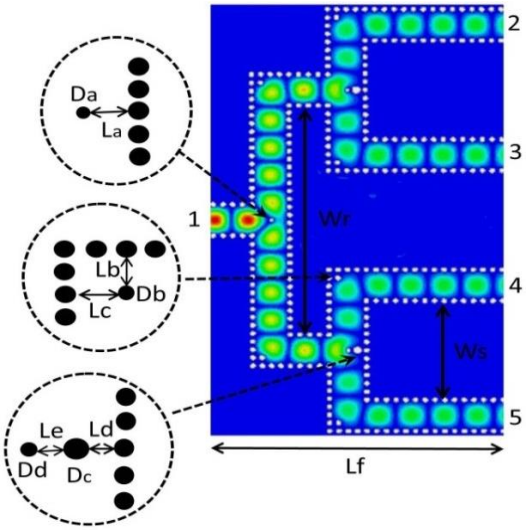

Fig. 4. SIW power divider schematic and E-field distribution

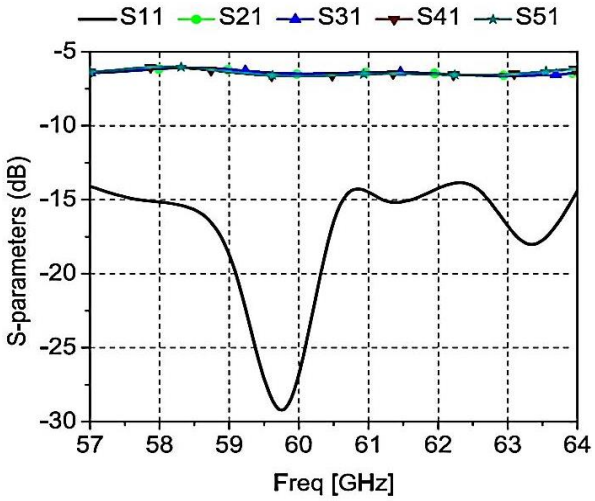

Fig. 5. Simulated S-parameters of SIW power divider.

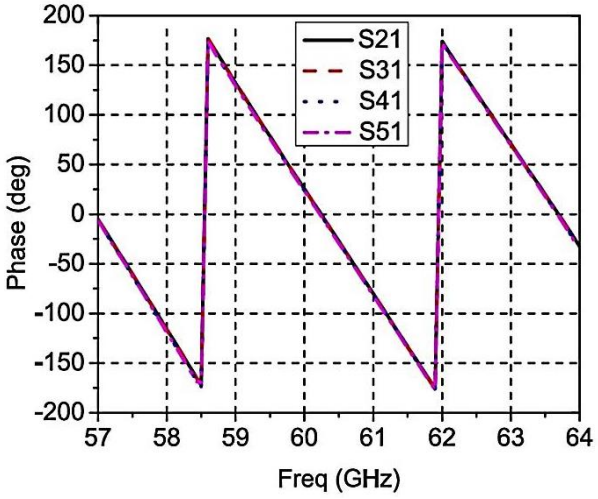

Fig. 6. Simulated phase at output of SIW power divider.

Figure 7 shows the simulated radiation patterns at 58, 60, 62 and 64 GHz. It is seen that the side lobe levels for both E-plane and H-plane are below -12 dB. Further, the cross polarization levels are also below -18 dB. Front to back ratio is a useful parameter used in describing the performance of directive antennas. In highly directive antennas, it is desirable to focus all radiated energy in the front direction and keep the energy radiated in unwanted direction (i.e., back side) to the minimum. In Fig. 8, the simulated front to back ratio of the antenna array shown. The front to back ratio is observed to be between 28-34 dB in the 60 GHz band.

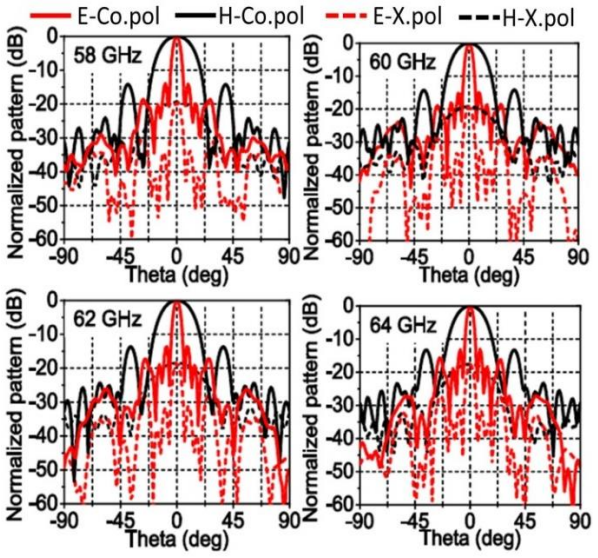

Fig. 7. Simulated radiation patterns.

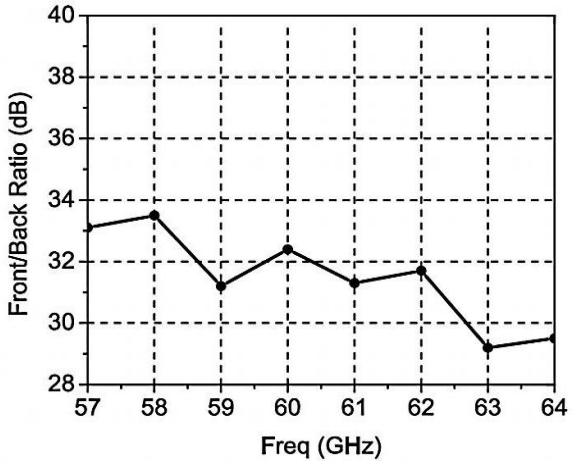

Fig. 8. Simulated front to back ratio.

III. MEASUREMENT

Figure 9 shows the fabricated antenna array. The dimension of the ALTSA array is 78.38 mm x 43.75 mm x 0.254 mm. Figure 10 shows the simulated and measured return loss and gain of the proposed 1x4 ALTSA array. The S11 parameters and gain of the antenna array are measured utilizing MVNA 8-350 with probe station. The measurement of radiation pattern is performed in far field anechoic chamber. From Fig. 10, it is observed that the simulated and measured return losses are better than 12 dB over the 60 GHz band. At 60 GHz the measured return loss is better than 24 dB. It is observed that there is good agreement between the measured and simulated results. Some slight differences between the simulated and measured results can be attributed to fabrication and calibration related tolerances. Further it is seen that the gain is almost flat over the 60 GHz band. Similarly, from Fig. 10 the simulated gain is observed to be 23 ± 0.4 dBi and the measured gain is seen to be 23.1 ± 0.5 dBi over the 60 GHz band.

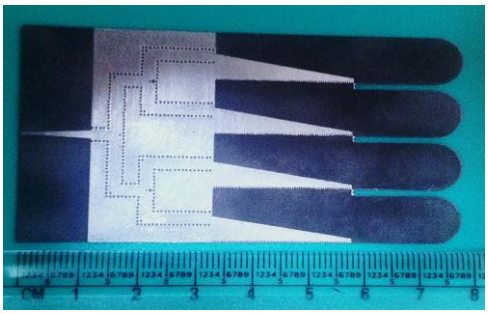

Fig. 9. Fabricated 1x4 ALTSA array.

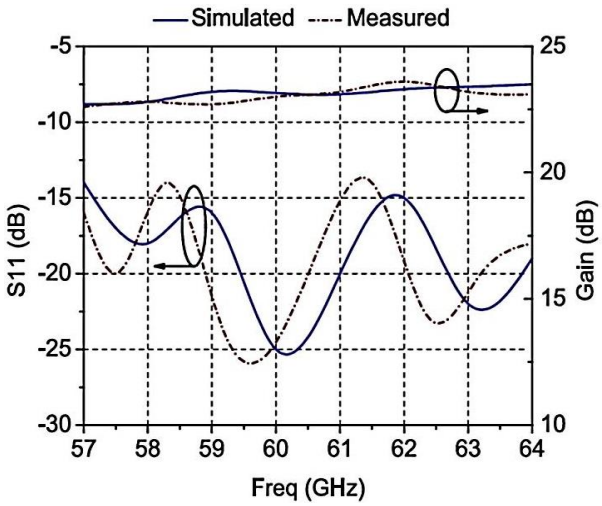

Fig. 10. Measured gain and return loss of ALTSA array.

Further, simulated and measured E-plane radiation pattern is shown in Fig. 11. The simulated E-plane beamwidth is seen to be 7° and the measured E-plane beamwidth is observed to be 8°. The measured and simulated side lobe levels in E-plane are at -15 dB. Similarly, from Fig. 12 the simulated H-plane beamwidth is observed to be 25° and the measured H-plane beamwidth is observed to be 27°. The simulated and measured side lobe levels in H-plane are at -14 dB. However, overall it is observed that there is a good agreement between the simulated and measured results.

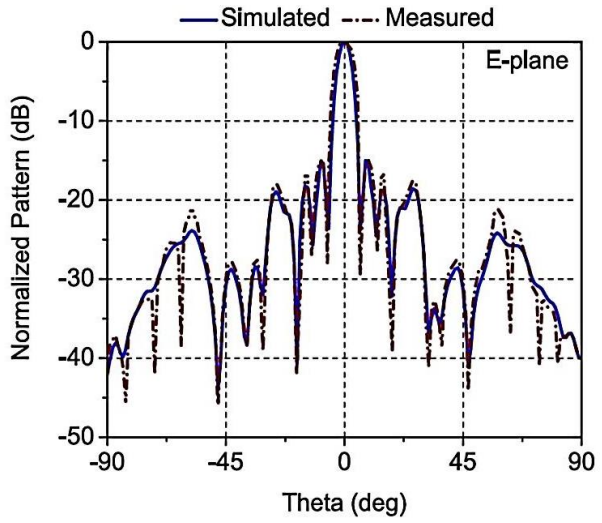

Fig. 11. Measured E-plane radiation pattern of ALTSA array at 60 GHz.

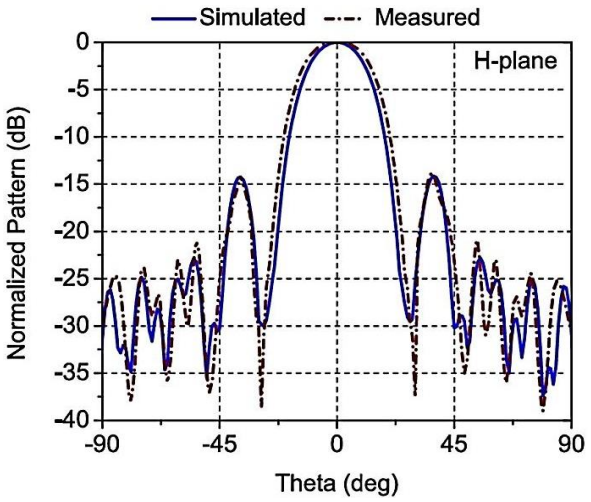

Fig. 12. Measured H-plane radiation pattern of ALTSA array at 60 GHz.

The comparison of other antenna arrays with this work is listed in Table 2. Numerous antenna arrays have been reported over the years for applications related to millimeter wave band. The general trend has been moving towards low cost, light weight and high gain antenna arrays. ALTSA with SIW feed can cater to those requirements. SIW fed ALTSA are known for high gain and wide bandwidth.

Table 2: Comparison with other antennas

Parameters	[21]	[14]	This Work
Antenna type	L-probe patch	ALTSA	ALTSA
Impedance bandwidth	29%	41%	11.6%
Operating frequency	60 GHz	80 GHz	60 GHz
No. of elements	16	4	4
Peak gain (dBi)	17.5	20	23.6

From the above table, it is observed that in [14] the peak gain of 20 dBi has been achieved with 4 ALTSA elements. Similarly, in [21] peak gain of 17.5 dBi has been reported but the number of elements used in the array is 16. In this work, peak gain of 23.6 dBi is achieved with four ALTSA elements. Though the impedance bandwidth of the antenna in this work is smaller than other antennas in the table, it should be noted that 11.6% covers 57-64 GHz and it is enough for multi-Gbps speed communication in 60 GHz band.

IV. CONCLUSION

In this paper, a high gain corrugated ALTSA array with dielectric loading for wireless communication application in the 60 GHz band is presented. The proposed design is validated with measurement of the fabricated prototype. Good agreement is seen between the simulated and measured results. The proposed antenna design has good return loss and high gain over the 60 GHz band. Overall, the proposed 1x4 ALTSA array has large bandwidth, high gain, compact size, light weight and is easy to fabricate using the low cost PCB technology. The single layer SIW design also suits mass fabrication. Hence, it is a suitable candidate for high speed communication in 60 GHz band.

ACKNOWLEDGMENT

Authors are very much obliged to ISRO, Government of India, for the assistance provided for the execution of this research work.

REFERENCES

[1] P. Smulders, "Exploiting the 60 GHz band for local wireless multimedia access: Prospects and future directions," *IEEE Communications Mag*azine, vol. 40, no. 1, pp. 140-147, 2002.

[2] A. Valdes-Garcia, S. Reynolds, A. Natarajan, D. Kam, D. Liu, J. W. Lai, Y- L. O. Huang, P.-Y. Chen, M. D. Tsai, J. H. C. Zhan, S. Nicolson, and B. Floyd, "Single element and phased array transceiver chipsets for 60 GHz Gb/s communicat-ions," *IEEE Communications Magazine*, vol. 49, no. 4, pp. 120-131, 2011.

[3] M. Bozzi, L. Perregrini, K. Wu, and P. Arcioni, "Current and future research trends in substrate integrated waveguide technology," *Radioengineer-ing*, vol. 18, no. 2, pp. 201-209, 2009.

[4] Y. J. Cheng, P. Chen, W. Hong, T. Djerafi, and K. Wu, "Substrate integrated waveguide beamforming networks and multibeam antenna arrays for low-cost satellite and mobile systems," *IEEE Antennas and Propagation Magazine*, vol. 53, no. 6, pp. 18-30, 2011.

[5] S. E. Hosseininejad, N. Komjani, H. Oraizim, and M. T. Noghani, "Optimum design of SIW longitudinal slot array antennas with specified radiation patterns," *ACES Journal*, vol. 27, no. 4, pp. 320-325, April 2012.

[6] R. Rezaiesarlak, M. Salehi, and E. Mehrshahi, "Hybrid of moment method and mode matching technique for full-wave analysis of SIW circuits," *ACES Journal*, vol. 26, no. 8, pp. 688-695, August 2011.

[7] J. Bai, S. Shi, and D. W. Prather, "Modified compact antipodal Vivaldi antenna for 4-50 GHz UWB application," *IEEE Transactions on Micro-wave Theory and Techniques*, vol. 59, no. 4, pp. 1051-1057, 2011.

[8] Z. Briqech, A. Sebak, and T. A. Denidni, "High gain 60 GHz antipodal Fermi tapered slot antenna

with sine corrugation," *Microwave and Optical Technology Letters*, vol. 57, no. 1, pp. 6-9, 2015.

[9] Z. C. Hao, W. Hong, J. Chen, X. Chen, and K. Wu, "A novel feeding technique for antipodal linearly tapered slot antenna array," *Proceedings of IEEE MTT-S Microwave Symposium Digest*, pp. 12-17, June 2005.

[10] S. Sugawara, Y. Maita, K. Adachi, and K. Mizuno, "Characteristics of a mm-wave tapered slot antenna with corrugated edges," *Proceedings of IEEE MTT-S Microwave Symposium Digest*, pp. 533-536, 1998.

[11] T. Djerafi and K. Wu, "Corrugated substrate integrated waveguide antipodal linearly tapered slot antenna array fed by quasi-triangular power divider," *Progress in Electromagnetic Research C*, vol. 26, pp. 139-151, 2012.

[12] P. Shrivastava and T. R. Rao, "Antipodal linear tapered slot antenna based radio link characterization in narrow hallway environment at 60 GHz," *J. Infrared Milli. Terahz Waves*, DOI 10.1007/s10762-016-0282-9.

[13] D. M. In, S. Pyo, H. S. Lee, M. J. Lee, and Y. S. Kim, "Antipodal linearly tapered slot antenna using unequal half-circular slotted sides for gain improvements," *Proceedings of Asia-Pacific Microwave Conference*, pp. 2036-2039, 2010.

[14] N. Ghassemi and K. Wu, "Planar high-gain dielectric-loaded antipodal linearly tapered slot antenna for E and W band gigabyte point to point wireless services," *IEEE Transactions on Antennas and Propagation*, vol. 61, no. 4, pp. 1747-1755, 2013.

[15] T. R. Rao, C. Sarath, N. Tiwari, and R. Jyoti, "Design of SIW fed antipodal linearly tapered slot antennas with curved and hat shaped dielectric loadings at 60 GHz for wireless communications," *IEEE 5th Asia-Pacific Conference on Antennas and Propagation (APCAP)*, pp. 309-310, 2016.

[16] H. Wang, D. G. Fang, B. Zhang, and W. Q. Che, "Dielectric loaded substrate integrated waveguide (SIW) H-plane horn antennas," *IEEE Transactions on Antennas and Propagation*, vol. 58, no. 3, pp. 640-647, 2010.

[17] K. Wu, D. Deslandes, and Y. Cassivi, "The substrate integrated circuits - A new concept for high-frequency electronics and optoelectronics," *Proceedings of Telecommunications in Modern Satellite, Cable and Broadcasting Service*, vol. 1, pp. III-X, October 2003.

[18] M. Bozzi, A. Georgiadis, and K. Wu, "Review of substrate-integrated waveguide circuits and antennas," *IET Microwaves Antennas and Propagation*, vol. 5, no. 8, pp. 909-920, 2011.

[19] K. S. Yngvesson, T. L. Korzeniowski, Y. S. Kim, E. L. Kollberg, and J. F. Johansson, "The tapered slot antenna - A new integrated element for millimeter wave applications," *IEEE Transactions on Microwave Theory and Techniques*, vol. 37, no. 2, pp. 365-374, 1989.

[20] N. Tiwari and T. R. Rao, "A substrate integrated waveguide based antipodal linear tapered slot antenna for 60 GHz wireless communications," *ACES Express Journal*, vol. 1, no. 8, pp. 220-223, 2016.

[21] L. Wang, Y. X. Guo, and W. X. Sheng, "Wideband high gain 60 GHz LTCC L-probe patch antenna array with a soft surface," *IEEE Transactions on Antennas and Propagation*, vol. 61, no. 4, pp. 1802-1809, 2013.

Nishesh Tiwari is currently pursuing Ph.D. from Department of Telecommunication Engineering at SRM University, India. He received his M.Tech Degree in Telecommunication Networks from SRM University in 2012. He is a Student Member of IEEE. His current research interests are Antennas and Propagation, Microwave Photonics and Wireless Sensor Networks.

T. Rama Rao is a Professor of Telecommunication Engineering at SRM University, India, and has a long-standing research experience on radiowave propagation studies for wireless communications. In the past, he has worked at Aalborg University, Denmark as a Research Professor in an EU funded project on cellular networks capacity enhancement, at Universidad Carlos III de Madrid, Spain, and at the University of Sydney, Australia, as a Visiting Professor. He is a Member of IEEE, WWRF, IET, ACM, and IETE.